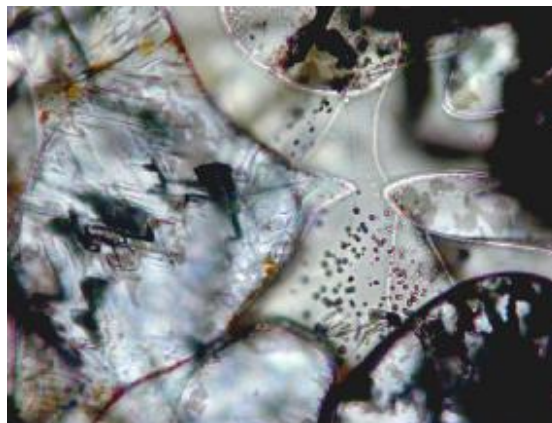


Fluid/melt – wall rock interaction in the upper mantle beneath the central Pannonian basin

Enikő Bali



Advisors:

Csaba Szabó

Lithosphere Fluid Research Lab
Department of Petrology and Geochemistry
Eötvös University, Budapest

David W. Peate

Department of Geoscience
University of Iowa

2004

Table of contents

| | |
|---|----|
| Figure catalogue | VI |
| Table catalogue | X |
| 1. Preface | 1 |
| 2. Introduction | 2 |
| 2.1 <i>The composition of the ultramafic rocks in Alpine peridotite massifs and mantle xenoliths</i> | 2 |
| 2.2 <i>The nature of metasomatism</i> | 3 |
| 3. The Cenozoic evolution of the Alpian-Carpathian-Pannonian region – Formation of the Pannonian basin | 7 |
| 3.1. <i>The recent setup of the basin</i> | 7 |
| 3.1.1. Lithospheric thickness in the Carpathian – Pannonian region | 8 |
| 3.1.2. Crustal thickness in the Carpathian – Pannonian region | 8 |
| 3.2. <i>The Cenozoic evolution of the Alpian-Carpathian-Pannonian region</i> | 10 |
| 3.2.1. Escape models | 10 |
| 3.2.2. Subduction and slab break-off model | 11 |
| 3.2.3. The Neogene evolution of the Pannonian basin in the background of the Carpathian subduction | 12 |
| 4. Sampling localities | 15 |
| 5. Petrography | 20 |
| 5.1. <i>Orthopyroxene-rich websterites</i> | 23 |
| 5.2. <i>Spinel peridotites with websterite-clinopyroxenite vein(s)</i> | 25 |
| 5.2.1. Spinel lherzolites with websterite veins | 25 |
| 5.2.1. Spinel lherzolites with clinopyroxenite vein | 28 |
| 5.3. <i>Spinel peridotites and clinopyroxenites with silicate melt pockets</i> | 29 |
| 5.3.1. Spinel peridotites with silicate melt pockets with carbonate | 29 |
| 5.3.2. Spinel peridotites with silicate melt pockets without carbonate | 32 |
| 6. Analytical techniques | 34 |

| | |
|---|-----------|
| 7. Mineral chemistry | 36 |
| 7.1. Major elements | 36 |
| 7.1.1. Olivines | 36 |
| 7.1.1.1. Orthopyroxene-rich websterites | 36 |
| 7.1.1.1.1. Mantle olivines | 36 |
| 7.1.1.1.2. Melt pocket olivines | 36 |
| 7.1.1.2. Spinel lherzolites with websterite and clinopyroxenite vein(s) | 36 |
| 7.1.1.3. Spinel peridotites and pyroxenites with silicate melt pockets and veins | 37 |
| 7.1.1.3.1. Mantle olivines | 37 |
| 7.1.1.3.2. Silicate melt pocket olivines | 37 |
| 7.1.1.3.2.1. Olivines in carbonate-bearing silicate melt pockets | 37 |
| 7.1.1.3.2.2. Olivines in carbonate-free silicate melt pockets | 37 |
| 7.1.2. Orthopyroxenes | 39 |
| 7.1.2.1. Orthopyroxene-rich websterites | 39 |
| 7.1.2.2. Spinel lherzolites with websterite and clinopyroxenite vein(s) | 39 |
| 7.1.2.3. Spinel peridotites and pyroxenites with silicate melt pockets and veins | 42 |
| 7.1.3. Clinopyroxenes | 42 |
| 7.1.3.1. Orthopyroxene-rich websterites | 43 |
| 7.1.3.1.1. Mantle clinopyroxenes | 43 |
| 7.1.3.1.2. Melt pocket clinopyroxenes | 44 |
| 7.1.3.2. Spinel lherzolites with websterite and clinopyroxenite vein(s) | 44 |
| 7.1.3.2.1. Websterite veined lherzolite with moderate Al-orthopyroxenes | 44 |
| 7.1.3.2.1. Websterite and clinopyroxenite veined lherzolite with Al-rich orthopyroxenes | 44 |
| 7.1.3.3. Spinel peridotites and pyroxenites with silicate melt pockets and veins | 47 |
| 7.1.3.3.1. Mantle clinopyroxenes | 47 |
| 7.1.3.3.2. Melt pocket clinopyroxenes | 47 |
| 7.1.3.3.2.1. Clinopyroxenes in carbonate-bearing melt pockets | 47 |
| 7.1.4. Spinel | 49 |
| 7.1.4.1. Orthopyroxene-rich websterites | 49 |

| | |
|--|----|
| 7.1.4.1.1. Mantle spinels | 49 |
| 7.1.4.1.2. Melt pocket spinels | 49 |
| 7.1.4.2. Spinel lherzolites with websterite and clinopyroxenite vein(s) | 49 |
| 7.2.3.2.1. Websterite veined lherzolite with moderate Al-orthopyroxenes | 49 |
| 7.2.3.2.1. Websterite and clinopyroxenite veined lherzolite with Al-rich orthopyroxenes .. | 50 |
| 7.1.4.4. Spinel peridotites and pyroxenites with silicate melt pockets and veins | 50 |
| 7.1.4.4.1. Mantle spinels | 50 |
| 7.1.4.4.2. Melt pocket spinels | 50 |
| 7.1.5. Amphiboles | 53 |
| 7.1.6. Glasses | 54 |
| 7.1.6.1. Orthopyroxene-rich websterites | 56 |
| 7.1.6.2. Spinel lherzolites with websterite and clinopyroxenite vein(s) | 56 |
| 7.1.6.3. Spinel peridotites and pyroxenites with silicate melt pockets and veins | 60 |
| 7.1.6.3.1. Glasses in carbonate-bearing silicate melt pockets and veins | 60 |
| 7.1.6.3.2. Glasses in carbonate-free silicate melt pockets and veins | 60 |
| 7.1.7. Carbonates | 62 |
| 7.2. <i>Trace elements</i> | 63 |
| 7.2.1. Clinopyroxenes | 63 |
| 7.2.1.1. Orthopyroxene-rich websterites | 66 |
| 7.2.1.2. Spinel lherzolites with websterite and clinopyroxenite vein(s) | 66 |
| 7.2.1.2.1. Websterite veined lherzolite with moderate Al-orthopyroxenes | 66 |
| 7.2.1.2.2. Websterite and clinopyroxenite veined lherzolite with Al-rich orthopyroxenes .. | 67 |
| 7.2.1.3. Silicate melt pocket – bearing xenoliths | 70 |
| 7.2.1.3.1 Mantle clinopyroxenes in silicate melt pocket – bearing xenoliths | 70 |
| 7.2.1.4.2. Melt pocket clinopyroxenes in silicate melt pocket – bearing samples | 72 |
| 7.2.2. Amphiboles | 72 |
| 7.2.3. Silicate melt accumulations | 73 |
| 7.2.3.1. Carbonate-bearing silicate melt accumulations | 74 |
| 7.2.3.2. Carbonate-free silicate melt accumulations | 74 |

| | |
|--|-----|
| 7.2.4. Carbonates | 76 |
| 7.3. <i>Sr - Pb isotopes</i> | 89 |
| 7.3.1. Sr-isotopes | 89 |
| 7.3.2. Pb-isotopes | 91 |
| 8. Bulk rock chemistry | 93 |
| 8.1. <i>Major elements</i> | 93 |
| 8.2. <i>Trace elements</i> | 95 |
| 8.2.1 Orthopyroxene-rich websterites | 96 |
| 8.2.2. Spinel lherzolites with websterite or clinopyroxenite vein(s) | 97 |
| 8.2.3. Spinel peridotites and pyroxenites with silicate melt pockets and veins | 98 |
| 9. Equilibrium conditions | 102 |
| 9.1. <i>Interaction between websterite - clinopyroxenite veins and peridotite wall rocks</i> | 102 |
| 9.2. <i>Equilibrium between melt pocket amphiboles and their wall rock peridotites</i> | 102 |
| 9.3. <i>Estimates of equilibrium temperature and oxygen fugacity</i> | 103 |
| 10. Formation of silicate melt pockets | 108 |
| 10.1. <i>The bulk composition of silicate melt pockets</i> | 108 |
| 10.2. <i>The estimation of composition and source of external melt(s)</i> | 113 |
| 10.3. <i>The source of the estimated external melt(s)</i> | 116 |
| 10.3.1. The effect of host basalt | 116 |
| 10.3.2. The effect of subduction related melt(s) | 117 |
| 10.4. <i>The significance of trace element distribution among the phases of the melt pockets</i> | 121 |
| 10.4.1. Trace element variation in silicate glass and bulk melt | 121 |
| 10.4.2 The presence of carbonate | 123 |
| 11. Evolution of websterite-clinopyroxenite veins | 125 |
| 11.1. <i>Formation of websterite-clinopyroxenite veins</i> | 125 |
| 11.2. <i>Development of clinopyroxene zoning</i> | 127 |
| 12. Formation of orthopyroxene-rich websterites | 130 |
| 13. Summarizing remarks | 136 |
| 14. Acknowledgements | 141 |

| | |
|--------------------------------|-----|
| 15. Összefoglalás | 142 |
| References | 145 |
| Appendix I | XII |

Figure catalogue

| | |
|--|----|
| Fig. 1: The mechanism of metasomatism due to melt – wall rock interaction | 4 |
| Fig. 2: Generalized cross section of a modern subduction zone | 5 |
| Fig. 3: Geological sketch map of the Carpathian – Pannonian region (CPR) | 7 |
| Fig. 4: Lithosphere thickness map of the Alpine – Carpathian – Pannonian region | 9 |
| Fig. 5: Plate tectonic models for the Tertiary evolution of the Carpathian – Pannonian system | 10 |
| Fig. 6: The Miocene to Pliocene evolution of the Pannonian basin system | 14 |
| Fig. 7: Geological sketch map of the Bakony – Balaton Highland Volcanic Field (BBHVF) | 15 |
| Fig. 8: Simplified stratigraphy column of Szentbékállá and Szigliget volcanoes | 18 |
| Fig. 9: The characteristic rock types of the BBHVF upper mantle xenolith suite, this study | 19 |
| Fig. 10: Modal compositions of the studied upper mantle xenoliths in Streckeisen's (1976) classification diagram | 20 |
| Fig. 11: Textural distribution of carbonate-free silicate melt pockets and veins in orthopyroxene-rich websterite Szb36 | 22 |
| Fig. 12: Textural appearance of composite xenolith Szb59 | 23 |
| Fig. 13: Petrographic features of websterite and clinopyroxenite veined spinel peridotites | 25 |
| Fig. 14: Distribution of silicate melt pockets and veins in lherzolite Szb21 | 30 |
| Fig. 15: Distribution of silicate melt pockets and texture of carbonate-bearing silicate melt pocket in olivine clinopyroxenite Szb50 | 30 |
| Fig. 16: Distribution of silicate melt pockets and veins in lherzolite Szb21 | 32 |
| Fig. 17: Distribution of silicate melt pockets and veins in lherzolite Szb04 and harzburgite Szb52 | 32 |
| Fig. 18: Mg# vs Al ₂ O ₃ and mg# vs Na ₂ O diagrams for BBHVF ultramafic xenoliths, this study | 39 |
| Fig. 19: Composition of clinopyroxenes in BBHVF ultramafic xenoliths in Enstatite-Wollastonite-Ferrosillite (En-Wo-Fs) diagram | 42 |
| Fig. 20: Na vs Al and Ca vs Al diagrams of clinopyroxenes in BBHVF ultramafic xenoliths | 47 |

| | |
|---|----|
| Fig. 21: Composition of spinels in BBHVF ultramafic xenoliths | 50 |
| Fig. 22: Classification of amphiboles in BBHVF ultramafic xenoliths | 53 |
| Fig. 23: Composition of silicate glasses in BBHVF ultramafic xenoliths in TAS diagram | 54 |
| Fig. 24: Compositional variation of silicate glasses in BBHVF ultramafic xenoliths in Harker diagrams | 58 |
| Fig. 25: Compositional variation of silicate glasses in different silicate melt accumulations of websterite veined lherzolite Szb63 in Harker diagrams | 60 |
| Fig. 26: Rare Earth Element (REE) distribution of clinopyroxenes in BBHVF ultramafic xenoliths in Sm/Yb vs La/Nd diagram | 62 |
| Fig. 27: Primitive mantle normalized multielement and chondrite normalized REE diagrams for clinopyroxenes and silicate melt accumulations for orthopyroxene-rich websterite Szb36 | 63 |
| Fig. 28: Primitive mantle normalized multielement and chondrite normalized REE diagrams for clinopyroxenes, silicate melt accumulations and carbonates for orthopyroxene-rich websterite/ harzburgite composite xenolith Szb59 | 64 |
| Fig. 29: Primitive mantle normalized multielement and chondrite normalized REE diagrams for clinopyroxenes of websterite veined lherzolite Szgk99/11 | 66 |
| Fig. 30: Primitive mantle normalized multielement and chondrite normalized REE diagrams for clinopyroxenes of websterite veined lherzolites Szb62 and Szb63 | 67 |
| Fig. 31: Primitive mantle normalized multielement and chondrite normalized REE diagrams for clinopyroxenes of clinopyroxenite veined lherzolite Szg01 | 68 |
| Fig. 32: Primitive mantle normalized multielement and chondrite normalized REE diagrams for clinopyroxenes, silicate melt accumulations and carbonates for lherzolite Szb21 and olivine clinopyroxenite Szb50 | 70 |
| Fig. 33: Primitive mantle normalized multielement and chondrite normalized REE diagrams for clinopyroxenes, amphiboles, silicate glass and carbonates for lherzolite Szb55 | 72 |
| Fig. 34: Primitive mantle normalized multielement and chondrite normalized REE diagrams for clinopyroxenes, amphiboles and silicate melt accumulations for lherzolite Szb04 and harzburgite Szb52 | 74 |
| Fig. 35: Sr-Pb isotopic composition of separated clinopyroxenes and silicate melt pockets of BBHVF ultramafic xenoliths | 89 |
| Fig. 36: Pb isotopic composition of separated clinopyroxenes and silicate melt pockets of BBHVF ultramafic xenoliths | 91 |

| | |
|---|-----|
| Fig. 37: Bulk rock major element variation diagrams for BBHVF ultramafic xenoliths | 93 |
| Fig. 38: Bulk rock trace element variation diagrams for BBHVF ultramafic xenoliths | 94 |
| Fig. 39: Primitive mantle normalized multielement and chondrite normalized REE diagrams for bulk compositions of orthopyroxene-rich websterites and their wall rocks . | 96 |
| Fig. 40: Primitive mantle normalized multielement and chondrite normalized REE diagrams for bulk compositions of websterite and clinopyroxenite veined lherzolites ... | 98 |
| Fig. 41: Primitive mantle normalized multielement and chondrite normalized REE diagrams for bulk compositions of silicate melt pocket – bearing ultramafic xenoliths | 99 |
| Fig. 42: Calculated trace element distribution coefficients between mantle amphibole and clinopyroxene of harzburgite Szb52 | 102 |
| Fig. 43: Calculated equilibrium temperature vs equilibrium oxygen fugacity diagram for BBHVF ultramafic xenoliths | 104 |
| Fig. 44: Calculated equilibrium temperature and equilibrium oxygen fugacity vs Pb isotopic composition diagrams for BBHVF ultramafic xenoliths | 106 |
| Fig. 45: Sr/Zr vs Ce/Pb and Nb/La vs Ti/Eu diagrams for silicate melt accumulations, clinopyroxenes and amphiboles of xenoliths Szb50, Szb52 and Szb55 | 109 |
| Fig. 46: Sr/Zr vs Ce/Pb and Nb/La vs Ti/Eu diagrams for silicate melt accumulations, clinopyroxenes and amphiboles of xenoliths Szb36, Szb21, Szb04 | 111 |
| Fig. 47: Primitive mantle normalized multielement diagram for the calculated external melts in silicate melt pockets of xenoliths Szb04, Szb21, Szb36 and Szb59 | 115 |
| Fig. 48: Primitive mantle normalized multielement diagram for the calculated external melts in silicate melt pockets compared to BBHVF alkaline basalts, Northern Pannonian Basin calc-alkaline andesites, subduction related silicate melts and fluids and subducted sediment | 117 |
| Fig. 49: Mixing curves for melt pocket – free ultramafic xenoliths and the possible external melts/fluids in Ce vs Ce/Pb diagrams for xenoliths Szb04, Szb21, Szb36 and Szb59. The melt pocket bearing bulk compositions and melt pocket compositions are also shown | 119 |
| Fig. 50: Primitive mantle normalized multielement diagram for measured and calculated bulk silicate melts of lherzolite Szb21 | 122 |
| Fig. 51: Comparison of major element composition of main compounds of websterite and clinopyroxenite veined lherzolites to the experimental results of Gaetani & Grove (1998) | 125 |
| Fig. 52: Equilibrium pressure and temperature diagrams calculated for cores and rims of clinopyroxenes in websterite and clinopyroxenite veined lherzolites | 128 |
| Fig. 53: REE-distribution of orthopyroxene-rich websterites and residual peridotites after 3 to 11 % partial melting of Szentbékállá protogranular ultramafic xenolith | 130 |

Fig. 54: Calculated trace element distribution of silicate melts in equilibrium with mantle clinopyroxenes of orthopyroxene-rich websterites 132

Fig. 55: Temperature and oxygen fugacity relationship between the average BBHVF mantle and the possible metasomatizing agents formed the rock types, this study 134

Table catalogue

| | |
|---|----|
| Table 1: Texture, modal composition and equilibrium conditions of the studied ultramafic xenoliths | 22 |
| Table 2: Modal composition of silicate melt pockets | 30 |
| Table 3: Major element composition of olivines in BBHVF ultramafic xenoliths, this study | 38 |
| Table 4: Major element composition of orthopyroxenes in BBHVF ultramafic xenoliths, this study | 41 |
| Table 5: Major element composition of clinopyroxenes in BBHVF ultramafic xenoliths, this study | 45 |
| Table 6: Major element composition of spinels in BBHVF ultramafic xenoliths, this study | 52 |
| Table 7: Major element composition of amphiboles in BBHVF ultramafic xenoliths, this study | 53 |
| Table 8: Major element composition of silicate glass in BBHVF ultramafic xenoliths, this study | 57 |
| Table 9: Trace element composition of mantle clinopyroxene, bulk silicate melt and silicate glass in orthopyroxene-rich websterite Szb36 | 77 |
| Table 10: Trace element composition of mantle clinopyroxene, bulk silicate melt, silicate glass and carbonate in harzburgite wall rock Szb59/1 | 78 |
| Table 11: Trace element composition of mantle clinopyroxene, bulk silicate melt in orthopyroxene-rich websterite vein Szb59/2 | 79 |
| Table 12: Trace element composition of mantle clinopyroxene in websterite veined lherzolite Szgk99/11 | 80 |
| Table 13: Trace element composition of mantle clinopyroxene in websterite veined lherzolite Szb62 | 81 |
| Table 14: Trace element composition of mantle clinopyroxene in websterite veined lherzolite Szb63 | 82 |
| Table 15: Trace element composition of mantle clinopyroxene in clinopyroxenite veined lherzolite Szg01 | 83 |
| Table 16: Trace element composition of mantle clinopyroxene, bulk silicate melt, silicate glass, melt pocket clinopyroxene and carbonate in lherzolite Szb21 | 84 |
| Table 17: Trace element composition of mantle clinopyroxene, bulk silicate melt, silicate glass, and carbonate in olivine clinopyroxenite Szb50 | 85 |
| Table 18: Trace element composition of mantle amphibole, silicate glass, and carbonate in harzburgite Szb55 | 86 |

| | |
|--|-----|
| Table 19: Trace element composition of mantle clinopyroxene, bulk silicate melt, silicate glass and melt pocket clinopyroxene in lherzolite Szb04 | 87 |
| Table 20: Trace element composition of mantle clinopyroxene, amphibole and bulk silicate melt in harzburgite Szb52 | 88 |
| Table 21: Sr-Pb isotopic composition of separated clinopyroxenes and silicate melt pockets of BBHVF ultramafic xenoliths | 89 |
| Table 22: Bulk rock composition of BBHVF ultramafic xenoliths, this study | 101 |
| Table 23: Bulk composition of silicate melt pockets in orthopyroxene - rich websterites Szb36 and Szb59/2 | 108 |
| Table 24: Calculated major element composition of external melts in silicate melt pockets | 114 |
| Table 25: Calculated trace element composition of external melts in silicate melt pockets | 115 |
| Table 26: Comparison of calculated equilibrium pressure and temperature for cores and rims of clinopyroxenes in websterite and clinopyroxenite veined lherzolites | 128 |

1. Preface

Upper mantle xenolith - bearing Neogene-Quaternary alkali basalts are found both in the central (Little Hungarian Plain, Bakony-Balaton Highland), and marginal parts (Styrian basin, Nógrád-Gömör and Eastern Transylvanian basin) of the Carpathian Pannonian region (CPR) (Fig. 1), providing a unique opportunity for studying the evolution of the lithosphere. The study of ultramafic xenoliths from these localities recognized the effects of numerous mantle processes such as different extents of partial melting, deformation and mantle metasomatism. Previous studies pointed out that following the extensive depletion of the mantle (~ 1 Ga, but at least much before than Tertiary, Embey-Isztin et al., 2001) remarkable incompatible trace element and variable Nd-Sr isotopic enrichment dominantly affected the deformed lithospheric mantle. This enrichment was interpreted by Downes et al. (1992) as being due to the host alkaline magmas and subduction-related calc-alkaline magmas or fluids traced in the central Pannonian basin. Most studies dealing with mantle xenoliths from the area focused on peridotites which were not affected by modal metasomatism, with very few dealing with pyroxene-rich and amphibole-bearing ones (e.g.: Embey-Isztin, 1976; Embey-Isztin et al., 1989; Downes et al., 1992; Dobosi et al., 2003; Török et al., 2003). Furthermore origin of amphibole-enrichment and clinopyroxenites were attributed to metasomatic processes generated by the host alkaline magmatism (Downes et al., 1992; Dobosi et al., 2003). Technical developments in the last decades allow us to study the fine grained assemblages such as rarely occurring melt pockets, veins and fluid and/or silicate melt inclusions that have been recognized in the last several years. Thus, attention has been focused on these clusters (e.g.: Szabó et al., 1995a, 1996; Embey-Isztin & Scharbert, 2000; Bali et al., 2002) either.

The main aims of this study are:

1. To give detailed textural, major and trace element and isotopic characterization of less studied rock types as orthopyroxene-rich websterites and websterite veins in spinel lherzolitic wall rock, as well as the rarely occurring silicate melt pockets;
2. To determine the conditions of melt/fluid–wall rock interactions and the formation of reaction products in the upper mantle;
3. To give a more comprehensive insight into the complex depletion – refertilization processes affected the lithospheric mantle beneath the central Pannonian basin.

2. Introduction

Detailed petrologic and geochemical studies of ultramafic rocks (as Alpine peridotite massifs and mantle xenoliths) have shown that the Earth's upper mantle was affected principally by two complex processes; partial melting and refertilization during its long term evolution. The development of new analytical techniques provides new possibilities for investigating these ultramafic rocks, particularly at fine scales, to get more information about the composition, migration, trapping and origin of the different types of mantle melts/fluids which play significant role on the evolution of the mantle lithosphere. In the next few pages I will provide a brief review of the nature of metasomatic processes which refertilize previously depleted mantle. The main aim of this chapter is to summarize the most important characteristics of metasomatic agents, which could be detected in numerous upper mantle xenolith suites all over the world.

2.1 The composition of the ultramafic rocks in Alpine peridotite massifs and mantle xenoliths

Ultramafic bodies found as xenoliths in alkali basalts and kimberlitic magmas or as tectonically emplaced bodies usually contain four main mineral phases as olivine, orthopyroxene, clinopyroxene and an Al-rich phase (garnet/spinel/plagioclase depending on the equilibrium pressure and temperature) and numerous accessory minerals. Ultramafic rocks can be subdivided into two main groups based on their bulk compositions and the major element compositions of the clinopyroxenes which they contain.

Type-I (Frey & Prinz, 1978) or Cr-diopsidic (Wilshire & Shervais, 1975) xenoliths are depleted in the so-called basaltic components (TiO_2 , Al_2O_3 , Na_2O [FeO, CaO]) and their origin is associated with ancient partial melting and depletion processes of the upper mantle. This group consists mainly of spinel and garnet lherzolites, harzburgites, dunites and wehrlites and clinopyroxenites. The source of these xenoliths is the depleted lithospheric and asthenospheric upper mantle.

The Type-II (Frey & Prinz, 1978) or Al-Augite (Wilshire & Shervais, 1975) suite is characterized by the high clinopyroxene content. They are mostly clinopyroxenites, websterites and wehrlites, rarely lherzolites or orthopyroxenites. These xenoliths originated from the lithospheric mantle where they form veins in the peridotite wall rock due to the intrusion and crystallization of former melts. Another possibility for the formation of the Al-Augite suite is 'underplating' of magmas at the mantle/crust boundary (these magmas can

probably be the products of the early stage of the host magmatism) where the ‘underplated’ assemblage crystallized. Accessory minerals such as amphibole, phlogopite, carbonate, sulfides apatite, rutile ilmenite as well as silicate glass and fluid inclusions can be present in both Type-I and Type-II xenoliths which can be the fingerprints of different mantle processes predating the host magmatism.

2.2 The nature of metasomatism

‘Metasomatism describes a process or processes whereby the mineralogy and/or chemical composition of a solid rock is altered by the introduction of chemical components from an external source; the alteration process is commonly accompanied by loss of other components from the altered rock.’ (Wilshire, 1988, modified from AGI Glossary, 1980). During these reactions the compositions of both the peridotite and the metasomatic agent change. The metasomatic fluids and melts can move along fractures or grain boundaries in the mantle producing a mineral segregate of the fluxing melt in veins causing a modal and chemical modification of the preexisting peridotitic rock (Fig. 1) (defined as modal metasomatism by Harte, 1983). In many cases the mineral segregates form veins in the mantle and due to subsequent melt/fluid infiltration the previously formed veins can provide channels for further melt infiltration due to the different rheological properties of vein material (Fig. 1). The composition of the metasomatized rock depends on both the previous fertility of the wall rock and the melt/rock ratio for instance refractory harzburgites reach equilibrium with infiltrated melt at lower melt/rock ratios than more fertile lherzolites, resulting in different trace element compositions of metasomatized harzburgites and lherzolites (e.g.: Bedini et al., 1997).

There are many examples where only the trace element and/or isotopic composition of the rock changed during metasomatism (e.g. Downes et al., 1992; Wiechert et al., 1997; Dobosi et al, 1999). This is the so-called cryptic metasomatism defined by Dawson (1984). Wilshire (1988) ascribed the cryptic metasomatism to the effect of separated fluid phase propagated beyond the zone of hydrous melt injection.

In geodynamic point of view widespread mantle metasomatism occur in subduction settings, as the altered basaltic oceanic plate goes through metamorphic phase transitions providing hydrous (and CO₂-bearing) fluid phase which react with the overlying peridotitic mantle wedge (Fig. 2). The slab-derived fluid metasomatises the mantle wedge, whose subsequent partial melting yields arc-magmas. Because the metamorphism of hydrous oceanic basalts yields amphibolite rocks, early experimental works performed on oceanic basalt focused on amphibole stability.

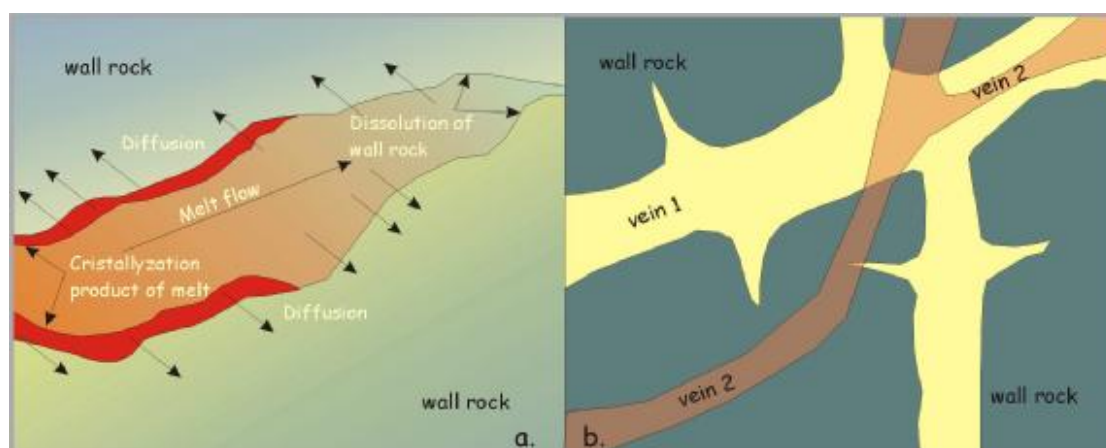


Fig. 1: The mechanism of metasomatism due to melt - wall rock reaction.

Fig. a indicates the dissolution of wall rock to the effect of melt flow and the crystallization of secondary assemblage on the wall. The diffusion also plays role during equilibration of vein and wall rock material.

Fig. b indicates that older veins can provide channels for subsequent melt infiltration.

These works have shown that amphibole breakdown (the amphibolite-eclogite transition), occurs at 22–25 kbar. More recent works have shown that, in addition to amphibole, there exists a number of other hydrous phases in metamorphosed hydrous basalts (e.g. zoizite, lawsonite, phengite) and serpentized peridotites (e.g. talc, A-phase, 10Å phase), each breaking down under widely different pressures (e.g. Schmidt & Poli, 1994, 1998; Poli & Schmidt 1995; Fumagalli et al., 2001 and references therein). As a consequence there is not only a single discontinuous dehydration reaction for fluid release from the slab, but instead there is a continuous volatilisation of metamorphic fluids toward the mantle wedge (Fig. 2). In contrast with the H₂O release from the subducting slab Yaxley & Green (1994) pointed out that carbonate is a refractory phase in eclogites in subduction regime, suggesting that CO₂ can be released only from young and hot subducting slab, but by the melting of carbonated eclogite siliceous melt is released from the down going slab which can be effective metasomatizing agent in the mantle wedge.

Predating the alkali mafic volcanism incipient asthenospheric melts upwell into the lithospheric mantle due to the extensional regime forming either hydrous (amphibole or phlogopite) or unhydrous metasomatic assemblage (clinopyroxenite) in the lithospheric mantle (e.g. Vaselli et al., 1995, Dobosi et al., 2003)

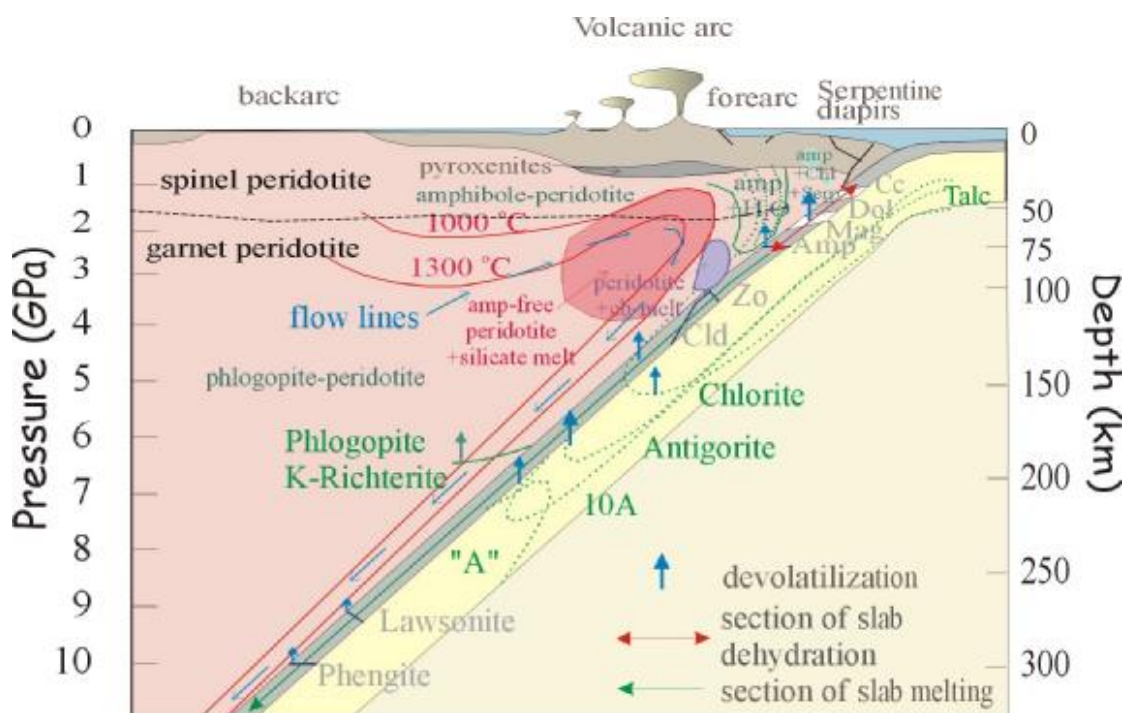


Fig. 2: Generalised cross-section of a modern subduction zone showing the position of the volcanic front and the phase transitions both in the subducted slab (Poli & Schmidt, 2002, and references therein) and in the mantle wedge (Wallace & Green, 1988; Niida & Green, 1999). Green contour lines indicate the phase transitions in the subducting serpentinitized ultramafics, blue contours indicate the phase transitions in the subducting basaltic crust.

Ce-calcite, Dol-dolomite, Mag-magnetite, Amp-amphibole, Zo-zoizite, Cld-Chloritoid, 10A (Fumagalli et al., 2001)- high pressure expandable sheet silicate ($\text{Mg}_3\text{Si}_4\text{O}_{10}(\text{OH})_2 \cdot n\text{H}_2\text{O}$), A (Schmidt & Poli, 1998) - ($\text{Mg}_3\text{Si}_2\text{O}_8(\text{OH})_6$ 11wt% H_2O).

In the last few years numerous studies have focused on the petrographic and chemical features of the newly formed mineral phases within peridotitic assemblage which can be attributed to different types of metasomatic events. Different mineral assemblages are considered to be good indicators of metasomatic agents. For example the trend of peridotite towards wehrlite and the presence of Si-, Na-rich clinopyroxenes and apatite is considered to be typical assemblage of metasomatism affected by carbonatite (e.g.: Yaxley et al., 1998 and references therein). Whereas the presence of hydrous phases such as amphibole and phlogopite are indicators of hydrous metasomatic agents which could be either mafic melt (when high Ti is found in the amphibole or phlogopite) or slab derived fluids (in the presence

of high LILE enrichment and HFSE in the hydrous phases) (e.g.: Vaselli et al., 1995; Parkinson & Pearce, 1998; Laurora et al., 2001).

3. The Cenozoic evolution of the Alpine-Carpathian-Pannonian region – Formation of the Pannonian basin

3.1. The recent setup of the basin

The paleo-biogeographic models of Géczy (1973, 1984), based on Jurassic fauna indicate that two units can be distinguished in the pre-Tertiary basement of the Pannonian basin (Fig. 3), the northern (ALCAPA) which has African affinity and the southern (TISZA) which has European affinity. The presence of these two units is supported by paleomagnetic data of Márton & Márton (1978, 1983) that indicate different rotations of these two mega units.

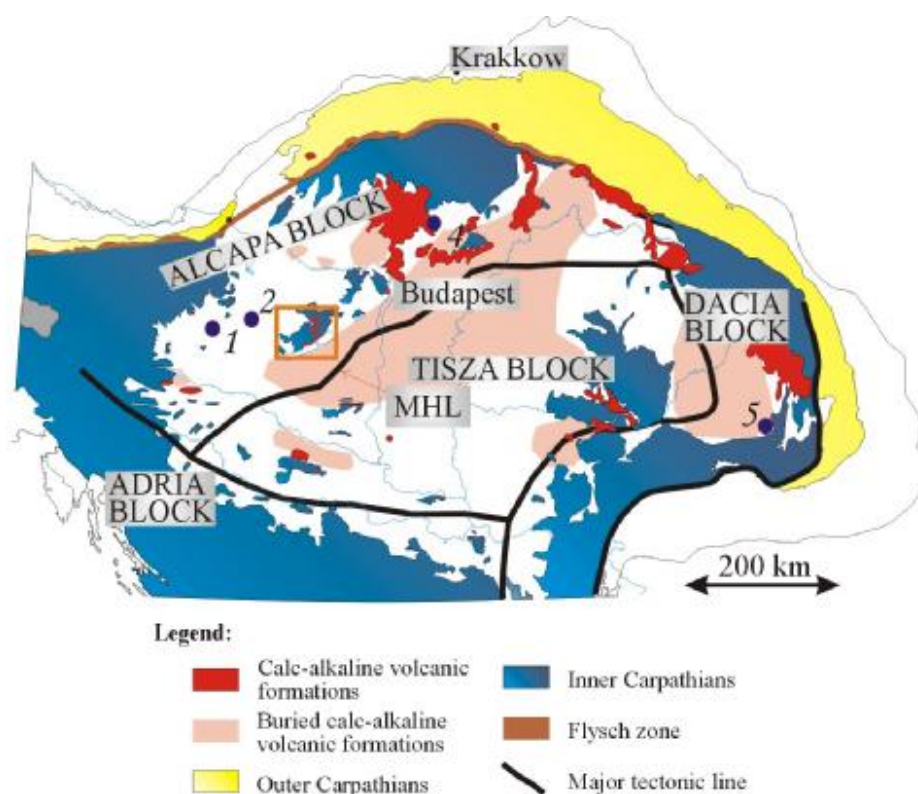


Fig. 3: Geological sketch map of the Carpathian - Pannonian region indicating the major tectonic units, the extent of Neogene calc-alkaline formations and the 5 major volcanic fields of Neogene-Quaternary alkaline basalts containing ultramafic xenoliths.

1 - Styrian basin; 2 - Little Hungarian Plain; 3 - Bakony - Balaton Highland; 4 - Nógrád-Gömör; 5 - Eastern Transylvanian basin. MHL - Middle Hungarian Line

The ALCAPA mega unit includes the Western Carpathians, the Bakony Mts., the Bükk unit (Balla, 1988a, b) and the Eastern Alps. Its southern border could be along the Mid-Hungarian line (Fig. 3) (e.g. Fodor et al., 2000, and references therein). Numerous stratigraphic, seismic and tectonic studies indicate the presence of different nappe structures in the pre-Tertiary basement of the unit, based mostly on seismic and drill hole data in the Little Hungarian Plain (e.g.: Tari, 1996, and references therein) and on stratigraphic and tectonic studies in the Bakony Mts. and Bükk Unit. The Mid-Hungarian Line is a right lateral shear zone which was rejuvenated several times during the evolution of the Pannonian basin (e.g.: Csontos & Nagymarosy, 1998 and references therein).

South of the Mid-Hungarian unit, the Tisza and Dacia mega units comprise the pre-Tertiary basement of the recent Pannonian basin (Fig. 3). The basement of this mega-unit, covered by thick Tertiary sediments, is also built up by nappes as shown by drill hole and seismic data. Although the basement of this unit is also strongly folded, its evolution is completely different from that of the northern ALCAPA unit (e.g. Géczy 1973, 1984; Márton & Márton 1978, 1983; Lelkes-Felvári, 1982; Szederkényi, 1984).

3.1.1. Lithospheric thickness in the Carpathian – Pannonian region

Based on seismic S-wave velocities the thickness of the lithosphere is 70-90 km in this region (Fig. 4). Delay times of teleseismic P waves also suggest about 50-70 km thick lithosphere in the Pannonian basin (Ádám et al., 1990), whereas in the Vrancea zone earthquakes at depths of 180 km can be related to a lithospheric slab remnant of Miocene subduction (Royden et al., 1982) this slab remnant is suggested by the results of seismic tomography (Spakman, 1990). The seismic gap between 40 and 70 km depth indicates that the slab has already detached (e.g. Onescu et al, 1984). Other interpretations however depict a deep, continuous lithospheric root (e.g. Chekunov & Sollogub, 1989), as a similar root can be observed in the Eastern Alps.

3.1.2. Crustal thickness in the Carpathian – Pannonian region

Thick crust is an attribute of the mountain range around the Pannonian basin. The western Carpathians are characterized by a 32-36 km thick crust whose structure is well-known from seismic profiles (e.g. Tomek & Thon, 1988). The images show a steeply dipping (40-50°) European foreland which is overlain by autochthonous or allochthonous molasses and a well-developed wedge made up from the Outer Carpathian flysch nappes. This subduction-

accretion complex is cut by horizontal reflectors at depth which can be interpreted as a new MOHO formed after the cessation of subduction in the Early Miocene (Tomek et al., 1989). The Eastern and Southern Carpathians are characterized by very thick crust (more than 40 km) and the crustal root coincides with the axis of the tomographic high, with an extremely deep MOHO in the Vrancea zone which rises steeply towards the Transylvanian basin.

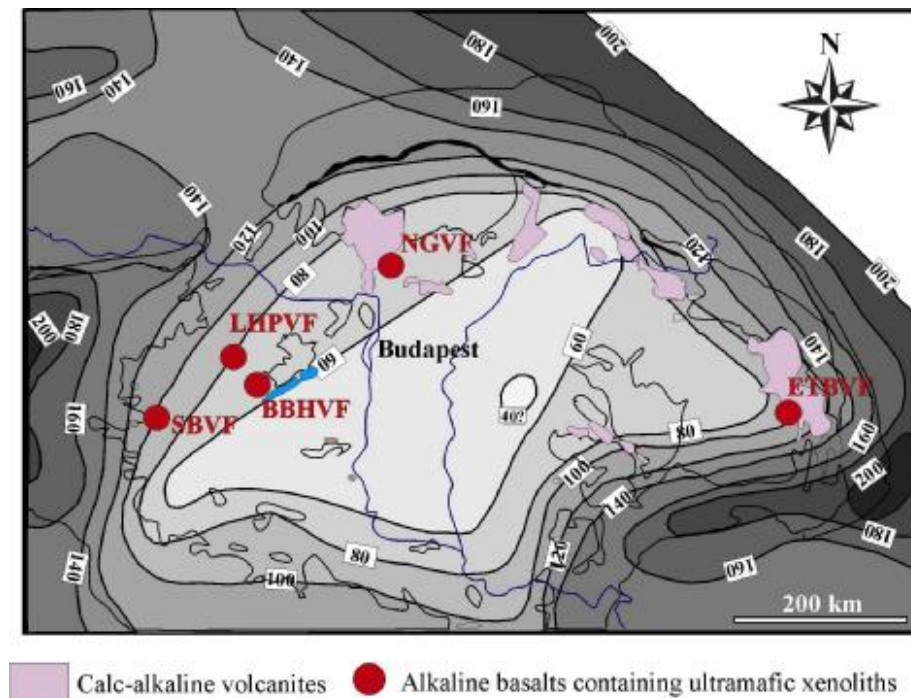


Fig. 4: Lithosphere thickness map of the Alpine - Carpathian - Pannonian region based on Lenkey (1999). Contours at 20 km intervals.

Thin crust is found in the Pannonian basin. The minimum thickness is located NW of Belgrade (22.5 km) (Aljanovic, 1987), whereas beneath the Transdanubian Central Range the crust is somewhat thicker than the average 30 km thickness characteristic of the basin. The high heat flow in the region may be compatible with the anomalous updoming of the upper mantle. Positive Bouguer anomalies observed in the Pannonian basin also suggest elevated upper mantle (Tomek, 1988), and the highest anomalies are always associated with the deepest part of the sub-basins. Modern reflection seismic profiling (e.g. Posgai et al., 1986) shows strongly layered lower crust in many areas, which is supported by observations of increased electric conductivity in deep crustal levels (Ádám et al. 1989). Warner (1990)

suggests that lower crustal layering is caused by subhorizontal shear zones developed during crustal extension and mostly by related intrusions of mantle derived mafic melts into the lower crust, and this model is also supported by interpretation of gravity anomalies.

3.2. The Cenozoic evolution of the Alpine-Carpathian-Pannonian region

3.2.1. Escape models

Based on the paleobiogeographic models of Géczy (1973, 1984) and paleomagnetic data of Márton & Márton (1978, 1983) described above, Kázmér & Kovács (1985) proposed a model in which the ALCAPA unit escaped eastwards from the Alpine-Dinaric System, moving up to 450 km (Fig. 5). The southern border of this escape could have been the Mid-Hungarian Line. Balla (1984) taken into account the paleomagnetic data and counted with an escape combined with the rotation of the ALCAPA and TISZA units (Fig. 5a) whereas Csontos et al. (1992) modeled the escape without block rotations (Fig. 5b). Below the unit large, low-angle normal faults controlled the movement, i.e. the downwards sliding from the Penninic unit (Ratsbacher et al., 1989, 1991a, b; Neubauer & Genser 1990; Decker & Perreson, 1996).

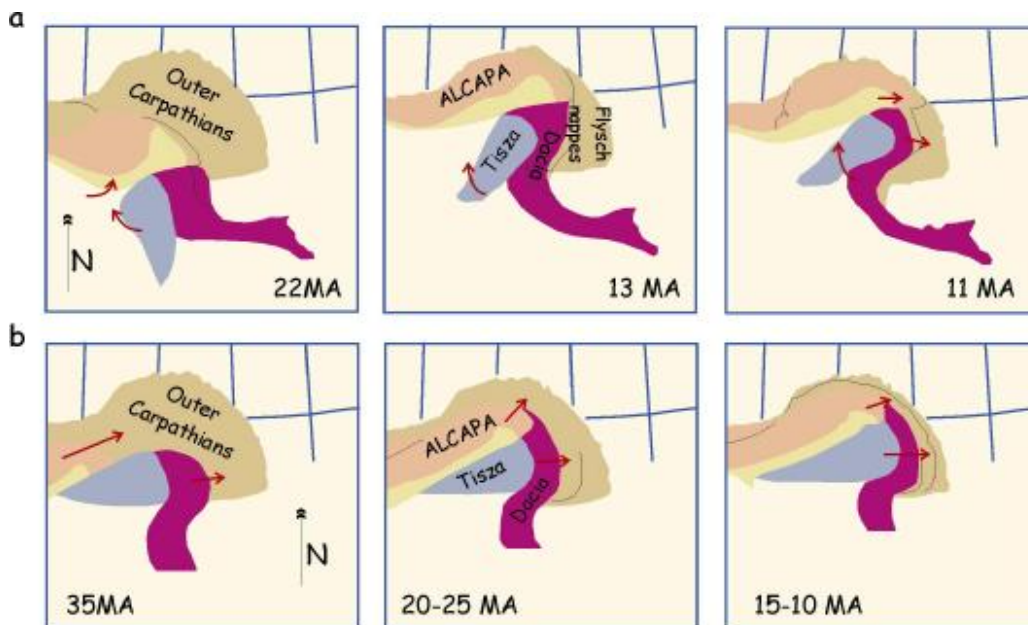


Fig. 5: Plate tectonic models for the Tertiary evolution of the Carpathian - Pannonian system (Csontos, 1995).

- a. Balla (1984) - escape model combined with block rotation.
- b. Csontos et al.(1992) - escape without rotation.

3.2.2. Subduction and slab break-off model

Nemcok et al. (1998) summarized and synthesized a wide range of diverse geological observations (the available dataset of seismic, gravity, conductivity studies, the nature of the volcanic activity, crustal and lithosphere thickness variations, uplift data, and facies correlations) and from this comprehensive survey they outlined a new model which provided further insights into the evolution of the Carpathian – Pannonian region.

They proposed that the 19-0 Ma calc-alkaline volcanism of the Inner Carpathian Volcanic Chain, as well as the 22.8-19.7 Ma old calc-alkaline magmatism in the Northern Croatian part of the Pannonian Basin (Simunic & Pamic, 1993), are the eastern continuation of the 42-25 Ma old Alpine calc-alkaline magmatism (von Blanckenburg & Davies, 1995) along the Periadriatic Lineament. The younger ages of the Croatian and Inner Carpathian volcanic rocks indicate propagation of slab break-off from west to east. The temporal and spatial development of Neogene foreland basins (e.g. Kovac et al., 1989), as constrained by the timing and direction of the last Flysch Belt thrusting (e.g. Jiricek, 1979) and by structural data (e.g. Nemcok, 1993), indicates that the oceanic plate underlying the remnant of the Carpathian Flisch Basin subducted south-westwards than westwards. This is supported by the seismic data of Tomek & Hall (1993) and Bielik et al. (1998) which point out a flat angle subduction of continental margin beneath the Western Carpathians propagating southwards. The Paleogene basins of the Carpathian-Pannonian region, which have compressional or transpressional origins (Fodor et al., 1992, 1994; Tari et al., 1993; Csontos & Nagymarosy, 1998), were formed in the background of this compressional belt (Tari et al., 1993). The ongoing subduction finally led to the collision between the European platform and the Carpathians at the end of the Early Miocene. The progressive change from the subduction to collision eastwards along the Carpathian arc controlled the break-off of the subducting slab (Seghedi et al., 2001), as indicated both by the calc-alkaline volcanism of the Inner Carpathians that started at 19-17.5 Ma until 0 Ma, and the ongoing detachment process in the Vrancea area (e.g.: Fuchs et al., 1979) (the detachment started in the West during the end of the Early Miocene and ran along the Carpathian arc to its present position in the Brassow area). The detachment-related volcanism was synchronous with collision.

3.2.3. The Neogene evolution of the Pannonian basin in the background of the Carpathian subduction

Extension caused by the role-back effect of the subducted slab was accompanied by the onset of crustally-derived volcanism above an asthenospheric upwelling (Stegena et al., 1975; Royden et al., 1983a, b; Salters et al., 1988; Lexa et al., 1993; Pécskay et al., 1995). Stegena et al. (1975) pointed out that mantle diapirism is the key phenomenon in the formation of the Pannonian basin, assuming that the Carpathian arc is a result of a lithosphere subduction process as suggested by numerous authors.

Horváth (1993) proposed a three layer extension model for the Pannonian basin based on the relations between the shallow and deeper lithospheric structure beneath the Little Hungarian Plain, which showed that:

- 1) In the brittle upper crust extension is accommodated by low-angle normal faults.
- 2) The lower crust is extended by subhorizontal ductile shear.
- 3) The mantle lid of the lithosphere is characterized again by high strength and extension is taken up primarily by movement along mantle fault and internal deformation of the mantle footwall.

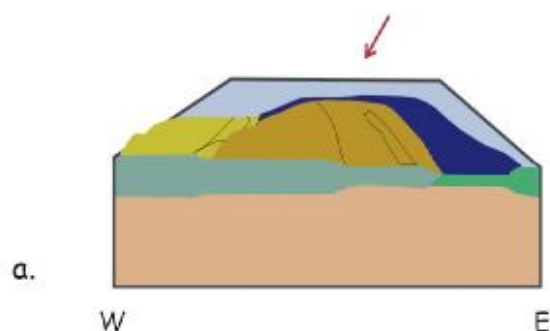
Furthermore, Horváth & Cloetingh (1996) modelled the formation of the Pannonian basin by a two-layer finite stretching model of the lithosphere incorporating lateral heat flow. They adopted crustal stretching parameters varying from 1.3 in Transdanubia to a maximum value of 1.8 in the Great Hungarian Plain. The stretching event was taken to be from 17-12 Ma taking into account the compaction of sediments. The basin formation process would be in association with thick postrift Alpine crust and high T regime. An important feature in the model is the incorporation of an increase in the level of stress during the last 2 Ma from 0 to 400 MPa compression to get the best fit between the predicted and the real stratigraphy in the basin. The modelling also suggests the notable absence of lithospheric strength in the mantle part. The strength profiles are characterized by a contraction of strength in the upper 15 km. Furthermore, the model points out that a dramatic change in the system occurred a few million years ago, when slab pull became inefficient as roll-back of the subducted slab could not proceed further. This occurred because the attenuated crust of the former marine basin had been fully consumed and the accretionary wedge had reached the Tornquist-Teisseyre zone of the East European foreland. From this time the Pannonian basin became completely locked in a stable continental environment without any chance of further extension in any direction.

This tectonic setting implies the establishment of a new stress field controlled by the Europe/Africa convergence.

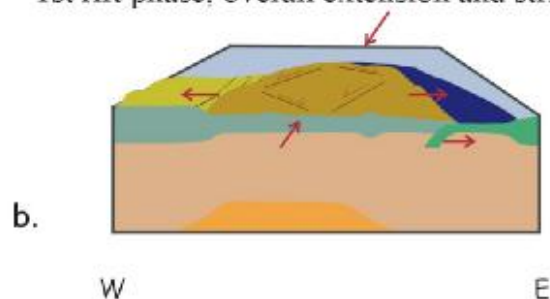
Quantitative models of extensional basin formation have explored the possible role of lower crustal flow toward the rift flanks in response to MOHO uplift (Moretti & Pinet, 1987) or in response to surface processes where erosion of the rift flanks may enhance lower crustal thinning in the basin area (Burov & Cloetingh, 1997). Such processes potentially explain the observed differential thinning of the lower crust with respect to the upper crust. Modeling shows that small-scale convective upwelling following a first phase of passive rifting may explain the late synrift to postrift mantle lithosphere thinning. It should be emphasized that no external heat source (i.e. mantle plume) is needed to drive the convective flow.

Huismans et al. (2001) applied a two-dimensional thermomechanical finite element model to the Pannonian basin history to investigate the conditions of small-scale convective upwelling in the mantle following the first passive rift phase. On the basis of tectonic evolution the following model provides the most reasonable scenario: in the model the thickness of the initial lithosphere was 150 km and the total amount of extension is 100 km (Fig. 6a). The first phase of extension happened between 17.5 and 14 Ma due to the role-back effect of the subducted slab. At 14 Ma an ~150 km wide surface depression and ~200 km wide upwelling of the asthenosphere developed. The subsidence of the center of the basin area was about 1800 m, whereas the asthenosphere had risen 40 km (Fig. 6b). At the end of the synrift the stretching factor for the crust was 1.3 whereas the mantle lithosphere was thinned by a factor of 2.2. In the postrift phase the asthenosphere has risen an additional 7-8 km, with a total mantle lithosphere thinning at 0 Ma of 3.0 (Fig. 6c). The asthenospheric dome obtained its peak rise velocity 7.6 km/my at 2.3 Ma following the initiation of the second rift phase.

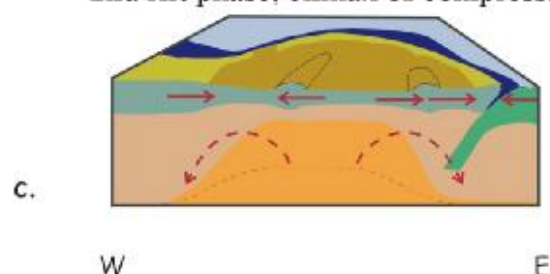
Late oligocene - Early Miocene N-S compression



Karpatian - Badenian (Middle Miocene) 1st rift phase, overall extension and strike slip



Late Miocene - Early Pliocene 2nd rift phase, climax of compression



| | |
|--------------------------------|---------------------------|
| European foreland | Subducting European plate |
| Flysch basin | Continental plate |
| Alpian-Carpathian thrust belts | Lithospheric mantle |
| Pannonian basin | Upwelling asthenosphere |

Fig. 6: The Miocene to Pliocene evolution of the Pannonian basin system based on Huisman et al. (2001).

- a. Prerift thickening.
- b. Passive rifting driven by slab roll-back
- c. Active rifting due to asthenosphere doming.

4. Sampling localities

The Transdanubian Central Range (TCR) is situated in the northern, ALCAPA, unit of the Carpathian – Pannonian region (Fig. 1). The boundaries of the TCR are the Balaton line in the south, the Rába – Diósjenő line in the west and north, but its eastern boundary is not clear. The Palaeozoic and Mesozoic sequences can be correlated to those in the Southern Alps. The oldest known sediments from the TCR were deposited during the Early Palaeozoic (e.g. Albani et al., 1985). These beds are characterized by low grade metamorphic rocks which had silty and clayey protolithes (e.g. Oravecz, 1964; Lelkes-Felvari, 1983). Numerous subsequent sedimentary cycles deposited km-thick sequences of platform and pelagic carbonates in the Permo-Triassic-Jurassic (e.g. Galácz & Vörös, 1972; Haas et al., 1988; Broglia Lorgia et al., 1990) and in the Late Cretaceous (e.g. Haas, 1979; Császár, 1986). Sedimentation during the Carboniferous (e.g. Barabás - Stuhl, 1975, Mihály, 1980) and the Permian and Oligocene (e.g. Gyalog & Korpás, 1996), was dominated by molass formation. From the Neogene onwards, the area was considered to be the part of the Pannonian basin (see Chapter 3) and sedimentation took place in the Pannonian Lake characterized by shore line to deep water sediments (e.g. Hámor, 1996; Jámor, 1996; Kókay, 1996). The thickness of these sediments can reach 4 km).

The Neogene-Quaternary alkaline basaltic volcanics (Fig. 7) known as Bakony -Balaton Highland Volcanic Field cross cut predominantly sedimentary sequence and the volcanics themselves are situated partly on Mesozoic carbonates and partly on Miocene clastic sediments (e.g. Jugovics, 1968, Embey-Isztin et al., 1993, Harangi et al., 1995, Németh & Martin, 1999). Both the Pannonian Lake sediments and the Mesozoic carbonates had a significant influence on the morphology of the volcanic edifices because their water content controlled the mechanism of the eruptions (Németh & Martin, 1999).

Furthermore, lithoclasts of these underlying formations are found in significant quantities in the basaltic pyroclastics. The studied peridotite xenoliths were collected from Szentbékállá and Szigliget which are two well-known xenolith localities in the Bakony-Balaton Highland Volcanic Field, (Fig. 7). It is interesting to note that xenoliths occur in pyroclastic sequences in both localities.

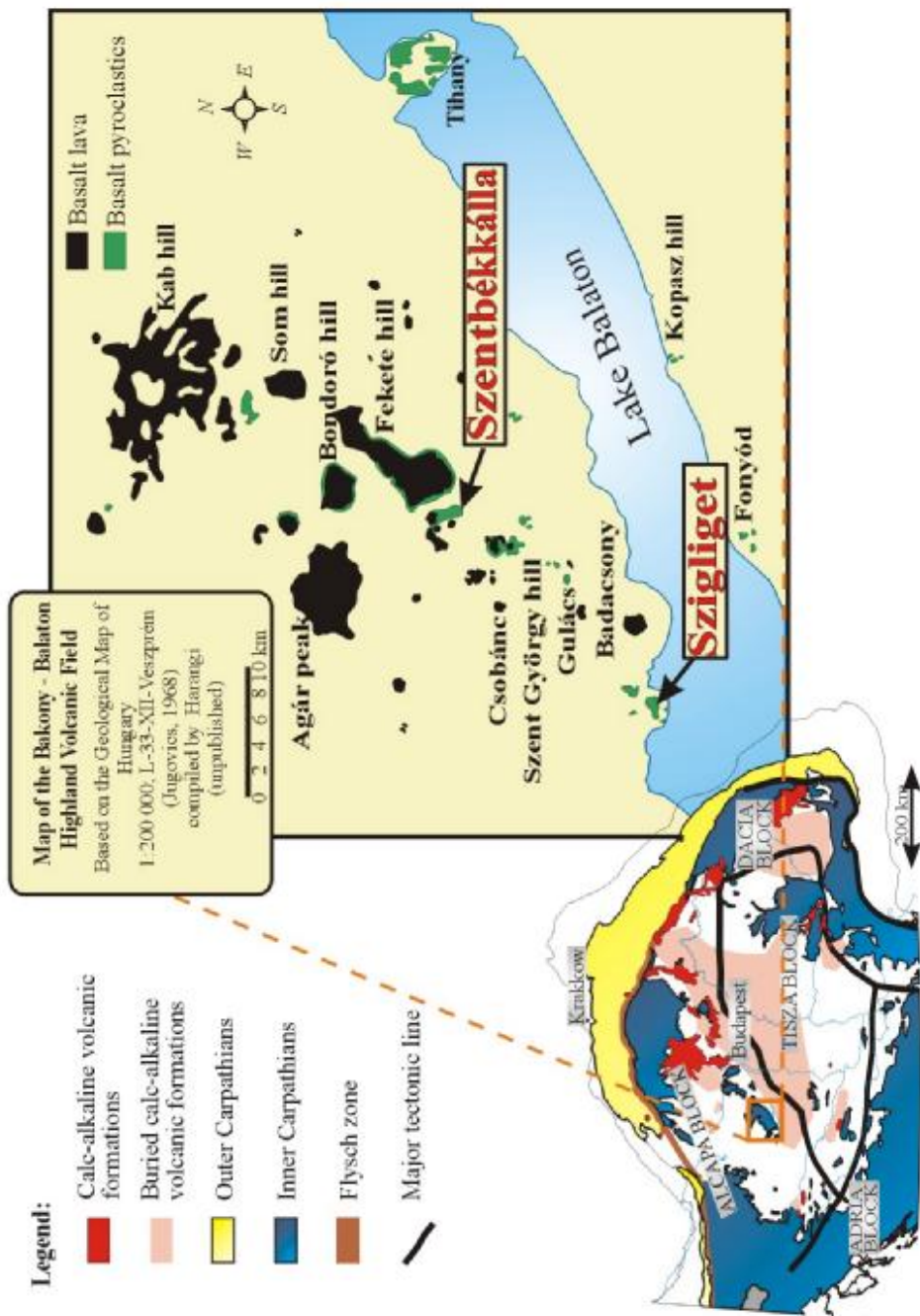


Fig. 7: Geological sketch map of the Bakony - Balaton Highland Volcanic Field showing the basaltic lava and pyroclastics outcrops. The studied localities are shown in red.

Szentbékállya: The Fekete hill volcanic complex is located in the northern part of the Káli basin (Fig. 7). The volcanic rocks of the Fekete Hill form a hydrovolcanic sequence which can be divided into two lithofacies (Fig. 8).

The lower unit comprises a massive block-bearing lapilli tuff, containing a high amount of polymict, angular lithic fragments about 10 cm, in diameter (Fig. 7). These fragments are usually Mesozoic and Tertiary carbonates, Triassic sandstones and high amount of Neogene (Pannonian) sand grains are also present. This unit contains large amount of ultramafic xenoliths. Scour fill structures as well as gas segregation channels are common in this lithofacies. The dominance of lithic fragments and the lack of bedding in the pyroclastic sequence indicate that it was deposited from a pyroclastic flow which filled a N-S oriented palaeovalley (Németh & Martin, 1999).

The upper unit consists of cross-bedded lapilli tuff and tuff beds with abundant lithic fragments (Fig. 8) but less ultramafic xenoliths than in the lower unit. Bedding indicates a N-S transport of the pyroclastic material. The presence of large volcanic bombs is characteristic. These bombs are either ballistic bombs or were transported in base surge formed by a Thaalian type eruption (Németh & Martin, 1999).

The age of the volcanism is 2.64-2.92 Ma (Balogh et al., 1986). The juvenile fragments at this locality have not previously been studied, although Németh & Szabó (1998) analyzed several dacitic glass fragments whose origin is not certain.

Szigliget: The volcanic edifice of the Szigliget peninsula (Fig.7) can be divided in three major units. The beds of the Unit1 crop out in the southern part of the peninsula, close to the Lake Balaton shore line (Fig. 7). They consist of thickly bedded, unsorted, matrix supported lapilli tuff/tuff breccia rich in accidental lithic fragments from the pre- volcanic basement. The sequence contains many peridotite and granulite xenoliths that have been studied in detail by Embey-Isztin (1976), Embey-Isztin et al. (1989), Downes et al. (1992). The accidental clasts are predominantly angular and distributed chaotically in the sand-rich matrix. Juvenile fragments comprise about the 20% of the unit. These are moderately vesiculated glass shards with phonotephritic composition (Németh et al., 2000). This sequence is interpreted as conduit-filling lapilli tuff deposited from a collapsing phreatomagmatic eruption column (Németh et al., 2000).

The beds of Unit2 have the largest volume in the pyroclastic sequence of Szigliget. This unit consists of coarse-grained, unsorted, accidental lithic clast-rich normal graded, bedded vitric lapilli tuff and tuff. Deep-seated accidental lithic clasts are common, but peridotite xenoliths are rare and present as cm or mm sized olivine or broken lherzolite fragments. The lapilli tuff beds are poor in matrix and calcite cemented, whereas the tuff is well-bedded. Juvenile clasts are weakly vesiculated and weakly to moderately microcrystalline, with tephritic to phonotephritic composition (Németh et al., 2000). The beds formed by subsurface phreatomagmatic explosion that created tuff rings/maars. The fine grained beds were deposited from a low concentration pyroclastic density current, whereas the coarse grained beds could be the result of fall out from the phreatomagmatic eruption column (Németh et al., 2000).

Unit3 represents the highest stratigraphic position cropping out on the NW side of the area. It is built up by fine to coarse grained, bedded accidental lithic clast-rich vitric lapilli tuff and tuff. Deep seated clasts as well as peridotites are rare, the accidental clasts derived from the shallow part of the pre-volcanic basement. The amount of juvenile vesiculated glass shards increases upwards in the section. The large amount of lithic clasts of shallow origin suggests a shallow sub-surface phreatomagmatic explosion (Németh et al., 2000). The undulatory, dune or parallel bedding of the sequence suggests a deposition by low concentration pyroclastic density currents and associated fall out (Németh et al., 2000).

The age of the volcanism is 3.4 Ma according to Balogh et al. (1986). Based on the chemical composition of the juvenile clasts, the rock is a slightly differentiated olivine-basanite with a S.I. (saturation index) of between 36.0 and 35.8, a D.I (differentiation index) of between 35.9 and 37.0, and mg# is 61.5 (Embey-Isztin et al., 1993).

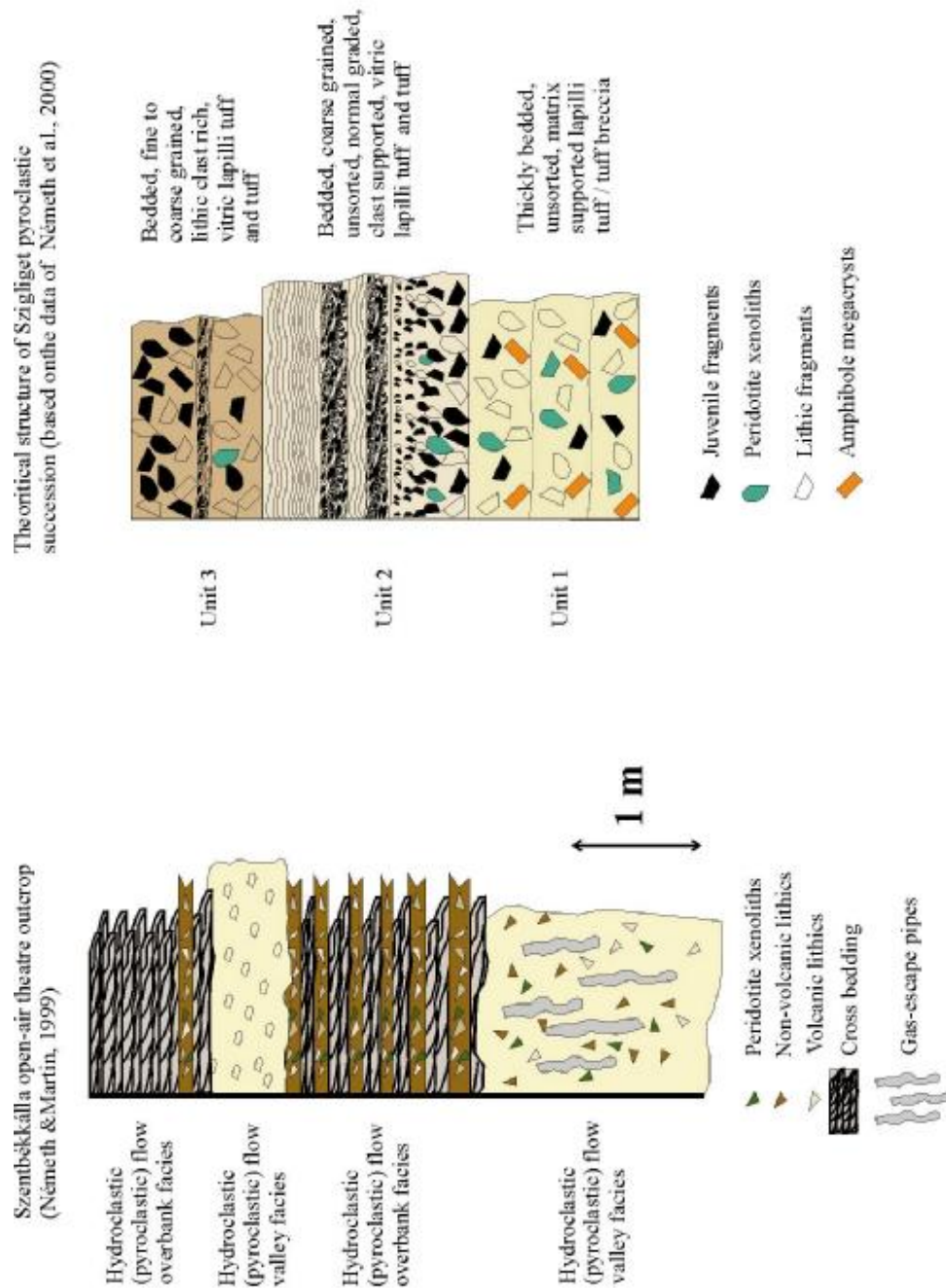


Fig. 8: Simplified stratigraphy column of Szentbékállá open-air theatre outcrop (Németh & Martin, 1999) and theoretical stratigraphy column of Szigliget volcano (Németh et al. 2000) showing the ultramafic xenolith - bearing beds.

5. Petrography

11 xenoliths from two localities of the Bakony-Balaton Highland Volcanic Field (BBHVF) were selected for detailed study. Nine samples are from Szentbékállá (Szb04, Szb21, Szb36, Szb50, Szb52, Szb55, Szb59, Szb62 and Szb63), and the rest (Szg01 and Szgk99/11) were collected from the Szigliget. Based on petrographical features and the abundance of the different mineral phases (olivine, orthopyroxene, clinopyroxene, spinel) and +/- silicate melt pockets/veins, the xenoliths were divided into 3 major groups (Table 1., Fig. 9). For the textural analyses the nomenclatures of Mercier & Nicolas (1975) and Embey-Isztin (1984) were applied.

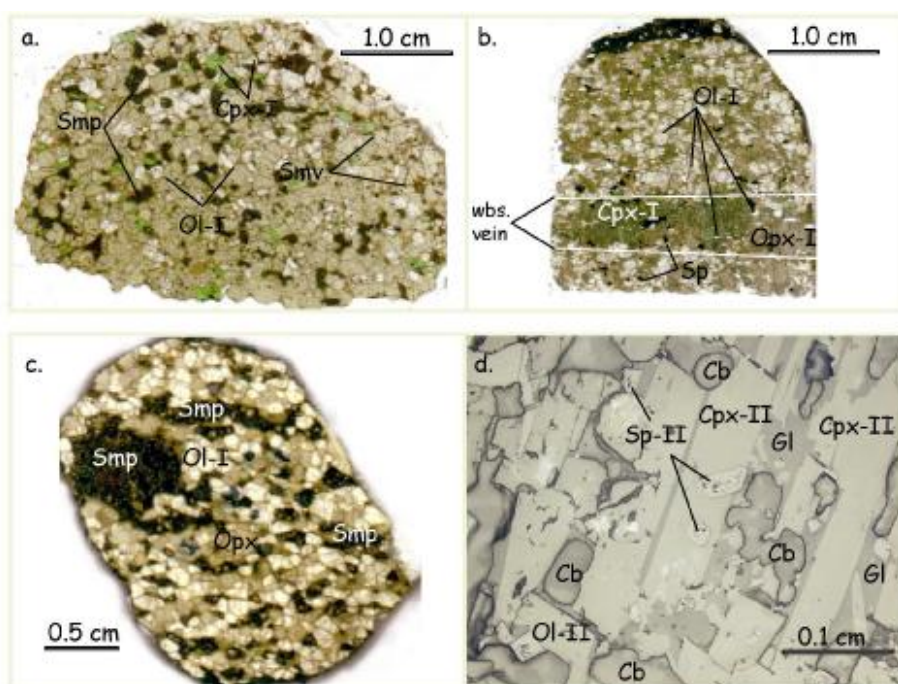


Fig. 9: The characteristic rock types of the Bakony-Balaton Highland Volcanic Field upper mantle xenolith suite.

a., Poikilitic textured orthopyroxene-rich websterite containing silicate melt pockets and veins. Scanned thin section of sample Szb36.

b., Porphyroclastic spinel ilherzolite containing magmatic textured websterite vein. Scanned thin section of sample Szb62/1.

c., Spinel peridotite with silicate melt pockets. Scanned thin section of equigranular textured Szb55 spinel harzburgite.

d., Typical texture of a carbonate-bearing silicate melt pocket. Photomicrograph of poikilitic textured Szb50 olivine clinopyroxenite, reflected light, 1N.

wbs - websterite, Ol-I - mantle olivine, Cpx-I - mantle clinopyroxene, Opx-I - mantle orthopyroxene, Sp-I - mantle spinel, Smp - silicate melt pocket, Smv - silicate melt vein, Ol-II - melt pocket olivine, Cpx-II - melt pocket clinopyroxene, Sp-II - melt pocket spinel, Cb - melt pocket carbonate.

These groups are:

- 1) Orthopyroxene-rich websterites (Szb36 and orthopyroxene-rich part [Szb59/2] of the composite xenolith Szb59) with poikilitic texture (after the nomenclature of Embey-Isztin, 1984) (Table 1, Fig. 9a, 10);
- 2) Protogranular and porphyroclastic (after the nomenclature of Mercier & Nicolas, 1975) spinel lherzolites containing one or two magmatic textured websterite or clinopyroxenite veins (in samples Szb62, Szb63, Szgk99/11 and Szg01) (Table 1, Fig. 9b, 10);
- 3) Spinel peridotites and pyroxenites with silicate melt pockets and veins (samples Szb04, Szb21, Szb36, Szb50, Szb52, Szb55, Szb59) (Table 1, Fig. 9d, 10).

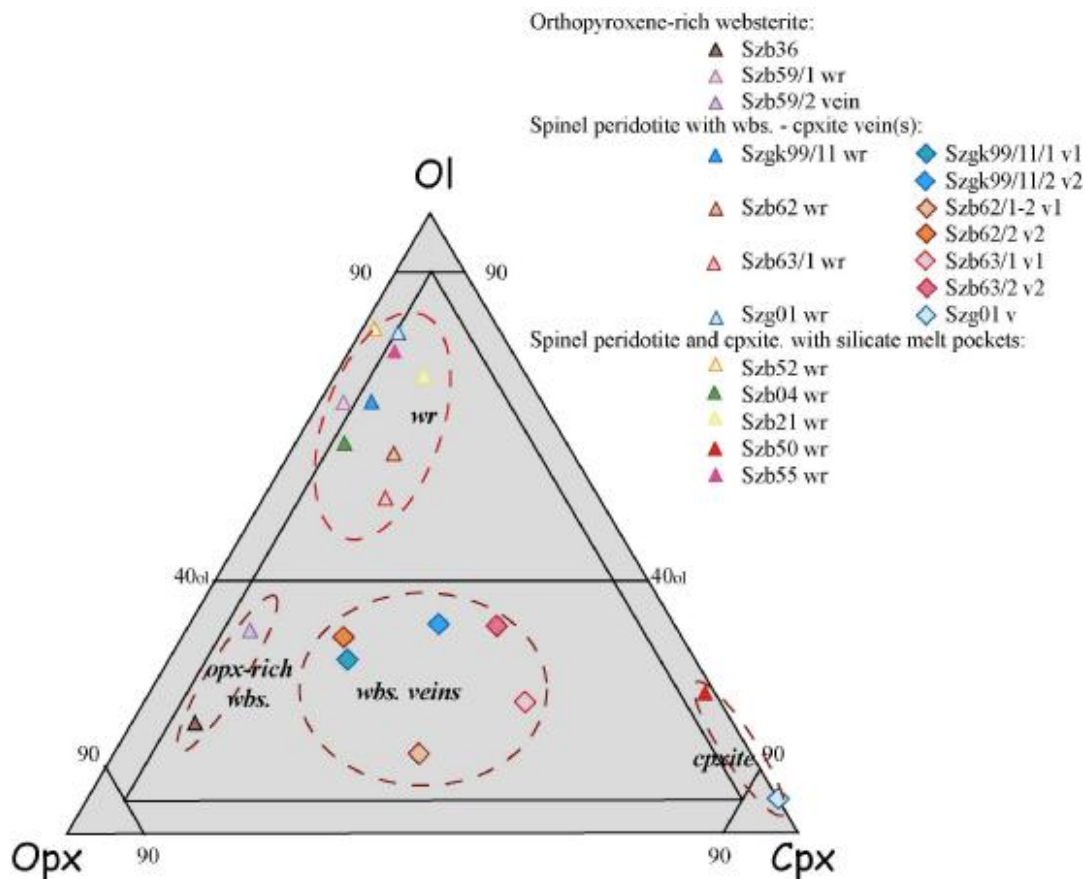


Fig. 10: Modal compositions of the studied Szentbékállya and Szigliget ultramafic xenoliths in Streckeisen's (1976) classification diagram. The wall rocks (wr) and veins (v) are indicated separately.

The detailed petrographical description of the studied samples is given based on these three main petrological types. The modal compositions are shown in Table 1.

| petrographic type | Sample | texture | Modal composition | | | | | Equilibrium T (in C) | dlogfO ₂ | p (in MPa) |
|-------------------------------------|---------------------|-----------------|-------------------|-----|----|----|-----|-------------------------|---------------------|----------------|
| | | | opx | cpx | sp | ol | amp | smp/vein/silmi | opx/cpx | |
| Opx-rich websterite | szb36 | poikilitic | 64 | 7 | 1 | 15 | tr | 13 | 9.1 | 1207-1947 |
| Opx-rich websterite (wr) | szb59/1 | poikilitic | 26 | 3 | 1 | 65 | - | 5 | 8.7 | 2000 |
| Opx-rich websterite | szb59/2 | magnetic | 41 | 6 | 2 | 22 | - | 29 | 6.8 | 2205-2271 |
| Spinel peridotite with webst. veins | szgk99/11 wall rock | porphyroclastic | 23 | 7 | 2 | 68 | - | tr | 3.3 | 1888-2095 |
| | szgk99/11/1 vein1 | magnetic | 32 | 33 | 2 | 33 | - | tr | 1.0 | 1969-1972 |
| | szgk99/11/2 vein2 | magnetic | 46 | 24 | 3 | 27 | - | tr | 1.9 | 1911-1934 |
| Spinel peridotite with webst. veins | szb62 wall rock | porphyroclastic | 24 | 14 | 3 | 59 | - | tr | 1.7 | 2075-2246 |
| | szb62/1-2 vein1 | magnetic | 44 | 41 | 3 | 12 | - | tr | 1.1 | 2097-2215 |
| | szb62/2 vein2 | magnetic | 43 | 21 | 7 | 29 | - | tr | 2.1 | 2193 |
| Spinel peridotite with webst. veins | szb63/1 wall rock | progranular | 28 | 16 | 5 | 51 | - | tr | 1.8 | 1976-2129 |
| | szb63/1 vein1 | magnetic | 25 | 49 | 7 | 19 | - | tr | 0.5 | 1857-2063 |
| | szb63/2 vein2 | magnetic | 23 | 40 | 6 | 31 | - | tr | 0.6 | not calculated |
| Spinel peridotite with opxite. vein | szg01 wall rock | porphyroclastic | 14 | 5 | 2 | 79 | - | tr | 2.8 | 2150-2310 |
| | szg01 vein | magnetic | - | 85 | 9 | 6 | - | - | - | 2110 |
| Spinel pyroxenite with smp | szb50 | poikilitic | 1 | 70 | 1 | 14 | - | 14 | 0.01 | 815-927 |
| Spinel peridotite with smp | szb21 | equigranular | 13 | 11 | 1 | 65 | tr | 10 | 1.2 | 953-971 |
| Spinel peridotite with smp | szb52 | poikilitic | 15 | 1 | tr | 70 | 1 | 13 | 15 | 1016-1024 |
| Peridotite with smp | szb55 | equigranular | 13 | 5 | - | 58 | 1 | 24 | 2.6 | 913-980 |
| Spinel peridotite with smp | szb04 | equigranular | 27 | 6 | 2 | 56 | - | 9 | 4.5 | 895-957 |

Table 1: Texture, modal composition and equilibrium conditions of studied Szentbékálka and Szigliget ultramafic xenoliths (BBHVF).

ol - mantle olivine, opx - mantle orthopyroxene, cpx - mantle clinopyroxene, sp - mantle spinel,
mp - silicate melt pocket, vein - silicate melt vein, silmi - silicate melt inclusions, tr - in traces
T - Brey & Köhler (1990) [range given by the methods BKN and Ca-in-opx], T* - Mercier (1980), p - Mercier (1980) [range given by
the methods en-sp and di-sp], dfo₂ - Ballhaus et al. (1991).

5.1. Orthopyroxene-rich websterites

The group of orthopyroxene-rich websterites (Fig. 9a, 11) is composed of two samples from Szentbékálla.

Szb36: This sample is a small (~ 3 cm in diameter) poikilitic textured orthopyroxene-rich websterite. Orthopyroxenes form large (up to 3 mm in diameter) tabular grains surrounding usually smaller (up to 1.5 mm in diameter) clinopyroxenes and olivines. The grain boundaries are straight or gently curved. These phases all contain small (up to 0.1 mm in diameter), rounded or subhedral, black spinel inclusions. Grains do not display evidence for internal strain.

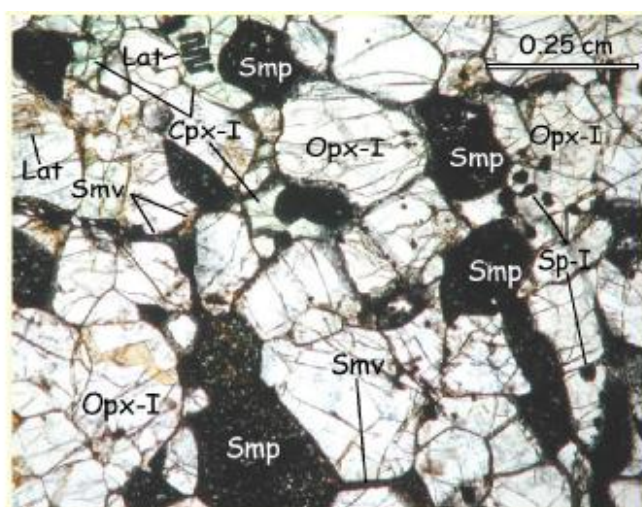


Fig. 11: Textural distribution of carbonate-free silicate melt pockets and veins in poikilitic textured, orthopyroxene-rich websterite of Szb36. Plane polarized light, 1N.

Opx-I - mantle orthopyroxene, Cpx-I - mantle clinopyroxene, Sp-I - mantle spinel, Smp - silicate melt pocket, Smv - silicate melt vein, Lat - laser ablation track.

A further characteristic of this sample is the presence of silicate melt pockets and veins. The silicate melt pockets are usually 1.0 to 3.0 mm in diameter, and their shapes are rectangular, in several cases slightly rounded towards the mantle phases (olivines, orthopyroxenes, clinopyroxenes) (Fig. 9a, 11). Silicate melt pockets are composed of euhedral clinopyroxenes, olivines, spinels (up to 0.1 mm in diameter) and pale brown interstitial silicate glass (Table 2., Fig. 11). Rounded empty bubbles also occur in the melt pockets. The silicate melt pockets are connected to each other by thin (0.1 mm) silicate melt

veins (Fig. 9a, 11) filled up by silicate glass. One grain of resorbed amphibole was also observed in one of the silicate melt pockets.

Szb59: This sample Szb59 is a composite xenolith composed of spinel harzburgite and orthopyroxene-rich websterite parts. In the following, the spinel harzburgite part will be referred as sample Szb59/1 and the orthopyroxene-rich part as Szb59/2 (Table 1, Fig.12a, b).

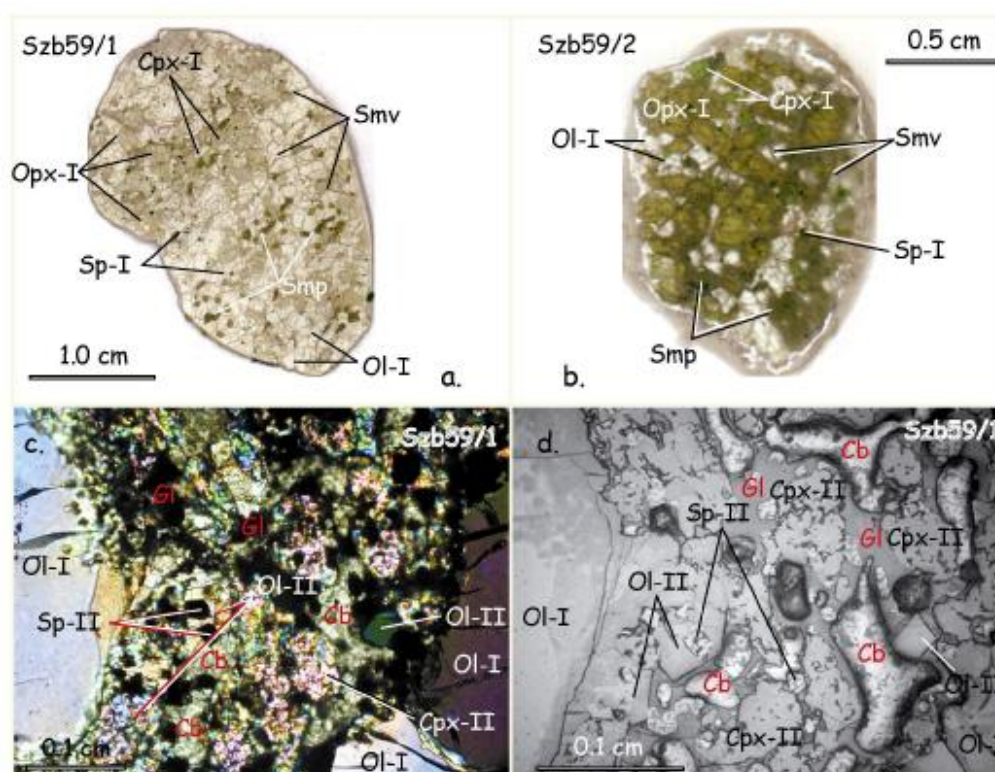


Fig. 12: Textural appearance of composite sample Szb59, and a carbonate-bearing melt pocket in Szb59/1.

a., The texture of poikilitic, spinel harzburgite wall rock (Szb59/1) of composite xenolith Szb59. Scanned thin section.

b., The texture of poikilitic orthopyroxene-rich vein (Szb59/2) of composite xenolith Szb59. Scanned thin section.

c., Photomicrograph of carbonate-bearing silicate melt pocket from poikilitic, spinel harzburgite Szb59/1. Plane polarized light, +N.

d., Photomicrograph of carbonate-bearing silicate melt pocket from poikilitic, spinel harzburgite Szb59/1. Reflected light, 1N.

Ol-I - mantle olivine, Opx-I - mantle orthopyroxene, Cpx-I - mantle clinopyroxene, Sp-I - mantle spinel, Smp - silicate melt pocket, Smv - silicate melt vein, Ol-II - melt pocket olivine, Cpx-II - melt pocket clinopyroxene, Sp-II - melt pocket spinel, Cb - carbonate, Gl - glass.

Sample Szb59/1 is a poikilitic textured spinel harzburgite. Olivines and orthopyroxenes form usually large (up to 1.0 cm) tabular grains whereas clinopyroxenes are usually smaller

(up to 3.0 mm) with straight or slightly curved grain boundaries. The large olivine grains are slightly deformed occasionally showing kink bands. Spinels only occur in triple junctions or as small (up to 0.1 mm in diameter), rounded or subhedral, black inclusions in orthopyroxenes and olivines.

Silicate melt pockets are large (up to 5.0 mm) patches with rectilinear or curvilinear borders towards the mantle minerals. Melt pockets are composed of euhedral-subhedral clinopyroxenes, olivines, spinels (up to 0.1 mm in diameter) and pale brown interstitial glass, and rounded carbonate crystals also occur (Fig. 12c, d, Table 2). Melt pockets are usually connected to each other by up to 0.1 mm thick silicate melt veins which are composed predominantly of pale brown silicate glass.

Sample Szb59/2 is a poikilitic orthopyroxene-rich websterite. Orthopyroxenes form 5.0-7.0 mm large tabular grains surrounding smaller olivine (up to 4.0 mm) and clinopyroxene (1.0-2.0, but occasionally 5.0 mm in diameter) crystals. Spinels only occur as 0.5 to 1.0 mm large rounded, black inclusions in orthopyroxene and olivine grains.

Silicate melt pockets, which are connected to each other with 0.1 to 0.2 mm wide veins, are the dominant phase of this sample. They usually form rounded to rectangular patches among the mantle minerals. They are composed of euhedral clinopyroxenes, olivines, spinels (up to 0.2 mm in diameter) and pale brown interstitial glass (Table 2). Very few, small (~10µm) carbonate crystals were observed in this sample.

5.2. Spinel peridotites with websterite-clinopyroxenite vein(s)

This group comprises two different subgroups based on the modal abundance of the different phases: most of the xenoliths are protogranular or porphyroclastic spinel lherzolites containing websteritic veins (Szb62, Szb63, Szgk99/11 and), whereas sample Szg01 is composed of spinel lherzolite wall rock and spinel clinopyroxenite vein.

5.2.1. Spinel lherzolites with websterite veins

Szgk99/11: This is a porphyroclastic textured spinel lherzolite crosscut by two magmatic textured spinel websteritic veins (Fig. 13b). Two thin sections were made in order to examine both veins shown in Table 1. In the spinel lherzolitic wall rock olivines and orthopyroxenes form up to 5.0 mm large, tabular grains. Olivines are usually kink banded and show undulatory extinction. Clinopyroxenes are small (up to 1.5 mm) having straight grain boundaries. They are surrounded by larger olivines and orthopyroxenes which have

curvilinear boundaries. Spinel is up to 2.0 mm long, usually elongated phases occurring predominantly as interstitial minerals among the previously mentioned phases or rarely as inclusions in them.

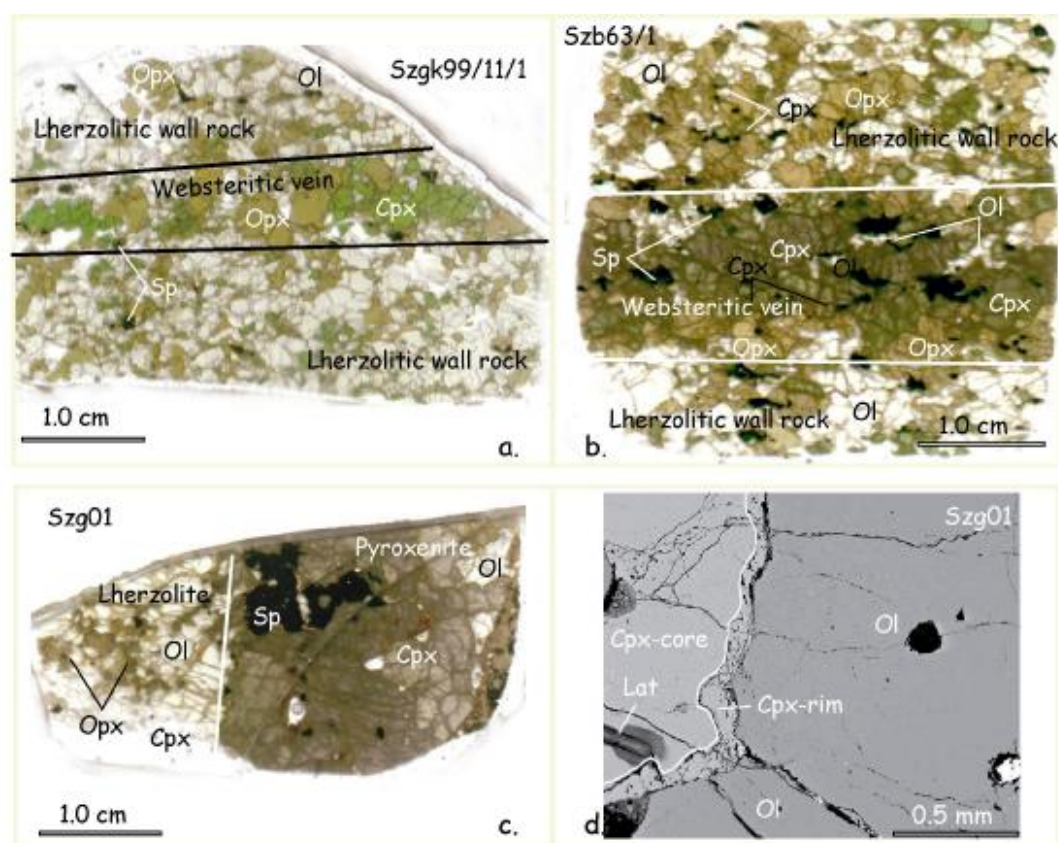


Fig. 13: Petrographic features of websterite and clinopyroxenite veined spinel peridotites.

a., Porphyroclastic spinel lherzolite with magmatic textured websterite vein. Scanned thin section of sample Szgk99/11/1.

b., Protogranular spinel lherzolite with magmatic textured websterite vein. Scanned thin section of sample Szb63/1.

c., Porphyroclastic spinel lherzolite - magmatic textured spinel clinopyroxenite composite xenolith. Scanned thin section of sample Szg01.

d., Spongy rim containing tiny silicate melt inclusions developed on mantle clinopyroxene of Szg01 composite xenolith. Development of these rims are characteristic both the spinel lherzolite and spinel clinopyroxenite halves of the xenolith. Back scattered electron image from the clinopyroxenite part of the xenolith.

Ol - olivine, Opx - orthopyroxene, Cpx - clinopyroxene, Sp - spinel, Lat - laser ablation track

One 0.6 cm wide (vein1) and another 0.4 cm wide (vein2) magmatic textured websterite vein was distinguished in this sample. The large (up to 8.0 mm long and 0.3 cm wide)

clinopyroxene and orthopyroxene crystals of the veins enclose smaller (up to 2.0 mm) olivines and spinels (Fig. 13b). Large crystals of clinopyroxene display recrystallization in the term of small (~0.5 mm) subgrains. Subgrain formation rarely occur in orthopyroxenes. The transition between the veins and the wall rock is smooth.

The network of fine (up to 80 microns wide) silicate melt veins composed mainly of colorless silicate glass enmeshes the whole xenolith, but its modal amount does not reach 1 V%. Furthermore, trails of secondary silicate melt inclusions (up to 15 microns) along healed fractures were also observed in all mineral phases.

Szb62: This is a porphyroclastic spinel lherzolite crosscut by two magmatic textured spinel websterite veins. Two thin sections were made in order to examine both websteritic veins shown in Table 1.

In the spinel lherzolite wall rock olivines and orthopyroxenes form 5.0 to 7.0 mm large, grains surrounding smaller grains of clinopyroxenes and spinels. These large crystals show undulatory extinction and in the olivines subgrain formation can be observed. Most of the clinopyroxenes are small (up to 1.5 mm) and surrounded by olivines or orthopyroxenes some of them however form large (up to 3.0 mm) crystals enclosing olivines and spinels. Spinel are up to 1.0 mm long, usually elongated phases occurring both as inclusions of the previously mentioned phases or as interstitial minerals.

Two 1.0 cm wide magmatic textured websterite veins were distinguished in this sample (Fig. 9b). The large (up to 2.0 cm long and 0.3 cm wide) orthopyroxene and clinopyroxene crystals have curvilinear boundaries enclose smaller (up to 2.0 mm) olivines and spinels and even each other. The contacts between the veins and wall rock are smooth.

Spongy rims (up to 0.2 mm wide) of clinopyroxenes containing abundant primary silicate melt and fluid inclusions (up to 20 microns) (Fig. 13d) are characteristic of both the veins and the lherzolitic wall rock. The network of tiny (up to 50 microns wide) silicate melt veins composed mainly of colorless silicate glass enmeshes the whole xenolith, but its modal amount does not reach 1 V%.

Szb63: This is a protogranular spinel lherzolite crosscut by two magmatic textured spinel websteritic veins (Fig. 13b). Two thin sections were made in order to examine both veins shown in Table 1.

In the spinel lherzolitic wall rock the crystals show weak to moderate shape preferred orientation. Olivines form up to 4.0 mm large grains occasionally showing kink banding. Orthopyroxenes are large (up to 5.0 mm), irregular shaped crystals. Clinopyroxenes are small (up to 1.5 mm) and surrounded by olivines or orthopyroxenes. Spinel are up to 1.0 mm long,

usually elongated phases occurring both as inclusions of the previously mentioned phases or as interstitial minerals. They are usually parallel to the websterite veins.

One 1.0 cm wide (vein1) and another 0.5 cm wide (vein2) magmatic textured websteritic vein was distinguished in this sample. The large (up to 2.0 cm long and 0.3 cm wide) orthopyroxene and clinopyroxene crystals of the veins enclose smaller (up to 1.5 mm) olivines and spinels and even each other (Fig. 13b). The long axes of the minerals are subparallel. The transition between the veins and wall rock is smooth.

Spongy rims of clinopyroxenes (up to 0.2 mm wide) (Fig. 13d) containing abundant primary silicate melt and fluid inclusions (up to 30 microns) are characteristic of both the veins and the lherzolitic wall rock. Secondary silicate melt inclusions along healed fractures of mantle minerals were also observed. The network of tiny (up to 80 microns wide) silicate melt veins composed mainly of colorless silicate glass enmeshes the whole xenolith, but its modal amount does not reach the 1 V%.

5.2.1. Spinel lherzolites with clinopyroxenite vein

This subgroup is composed only of one sample.

Szg01: This is a composite xenolith composed of a spinel lherzolitic and a spinel clinopyroxenitic half (Fig. 13c).

The spinel lherzolitic part i.e. wall rock of the xenolith is porphyroclastic. The large (up to 6.0 mm) tabular olivines are usually kink banded. Orthopyroxenes form smaller (up to 4.0 mm), irregular shaped crystals, whereas clinopyroxene neoblasts are usually tabular with a size of 1.0 to 2.0 mm, in diameter. Spinel is present as elongated (up to 1.0 mm long) minerals among the other phases.

The spinel clinopyroxenitic part i.e. vein of the xenolith has a magmatic texture. Clinopyroxenes form large (up to 7.0 mm) irregular shaped crystals enclosing rounded (up to 2.0 mm) olivines and holey-leaf shaped spinels (up to 5.0 mm, in diameter). The clinopyroxenes occasionally contain rounded sulphide inclusions with a size up to 50 microns. Spongy rims of clinopyroxenes (up to 0.2 mm wide) (Fig. 13d) containing abundant silicate melt and fluid inclusions (up to 30 microns) are characteristic of both the veins and the lherzolitic wall rock.

5.3. Spinel peridotites and clinopyroxenites with silicate melt pockets

This group is composed of eight samples, but as the melt pockets of samples Szb36, Szb59/1 and Szb59/2 have already been outlined (chapter 5.1), only samples Szb04, Szb21, Szb50, Szb52, Szb55 will be described here. Based on the modal composition of the melt pockets, two subgroups can be distinguished as the melt pockets of samples Szb21, Szb50 and Szb55 contain rounded carbonate aggregates (as already mentioned in sample Szb59/1) whereas this phase is absent from the melt pockets of samples Szb04 and Szb52 (as well as from Szb36).

5.3.1. Spinel peridotites with silicate melt pockets with carbonate

Szb21: This is an equigranular textured spinel lherzolite. Moderate shape preferred orientation is observed as the mineral phases (0.5 mm long and 0.3 mm wide) (Fig. 14a) and silicate melt pockets are elongated (later ones situated interstitially among the mentioned phases) having an average length of 0.7 mm. Internal strain features in the mantle minerals are absent or very rarely present in olivines. The grain boundaries are straight or gently curved. Black spinels are present in triple junctions and as inclusions in other mantle phases. Amphibole was not seen in the thin sections, but several grains of it were found during hand picking for further analyses.

The borders of the melt pockets are usually sharp and curvilinear towards the mantle phases. They composed of euhedral – subhedral clinopyroxenes, olivines, spinels, (up to 0.1 mm in diameter) and colorless to pale brown interstitial glass furthermore, large amount of rounded carbonate crystals (Table 2). Large silicate melt pockets are connected to each other by thin (up to 120 micron) silicate melt veins (Fig. 14b) which predominantly composed of colorless silicate glass and rounded carbonate aggregates.

Szb50: This is a poikilitic textured olivine clinopyroxenite with clinopyroxenes forming large (up to 3.0 mm) equidimensional grains surrounding smaller (0.5 to 1.0 mm, in diameter) orthopyroxene and olivine grains, connecting with straight boundaries. No internal strain features are observed. Spinel is present only as rounded or cubic, black inclusions in large clinopyroxene grains. Silicate melt pockets predominantly can be found in a 1.0 cm wide melt zone of the xenolith (Fig. 15a). Silicate melt pockets usually have curvilinear or occasionally rectilinear boundaries towards the mantle phases. They are composed of euhedral clinopyroxenes, olivines (up to 0.1 mm) and fine (up to 10 microns) spinels

interstitial glass and large amount of carbonate aggregates forming rounded boubles (Table 2, and Fig. 15b). Silicate melt veins were not observed among the melt pockets.

| Phases | Samples Szb36 (n=3) | | Szb52 (n=8) | | Szb04 (n=9) | | Szb55 (n=6) | |
|------------------|---------------------|--------|-------------|-------|-------------|-------|-------------|-------|
| | m.c. | s.d. | m.c. | s.d. | m.c. | s.d. | m.c. | s.d. |
| Olivine-II | 6.1 | 0.120 | 8.8 | 5.753 | 8.0 | 2.750 | 16.0 | 6.459 |
| Spinel-II | 1.1 | 0.475 | 3.0 | 1.979 | 1.9 | 1.875 | 1.2 | 0.413 |
| Clinopyroxene-II | 59.8 | 11.095 | 60.6 | 14.60 | 41.9 | 10.28 | 24.8 | 2.737 |
| Glass | 32.8 | 11.325 | 27.3 | 8.341 | 48.0 | 5.775 | 47.4 | 5.329 |
| Carbonate | 0.0 | - | 0.0 | - | 0.0 | - | 10.5 | 5.690 |

| Phases | Samples Szb50 (n=8) | | Szb21 (n=5) | | Szb59/1 (wr) (n=5) | | Szb59/2 (v) (n=5) | |
|------------------|---------------------|-------|-------------|-------|--------------------|-------|-------------------|-------|
| | m.c. | s.d. | m.c. | s.d. | m.c. | s.d. | m.c. | s.d. |
| Olivine-II | 16.9 | 3.697 | 8.3 | 4.528 | 14.6 | 4.394 | 6.7 | 5.430 |
| Spinel-II | 0.5 | 0.538 | 0.6 | 0.286 | 3.2 | 2.017 | 1.7 | 0.510 |
| Clinopyroxene-II | 21.9 | 8.403 | 25.1 | 12.86 | 19.1 | 6.900 | 57.8 | 8.947 |
| Glass | 37.9 | 11.76 | 53.9 | 4.686 | 55.1 | 7.450 | 33.8 | 8.860 |
| Carbonate | 22.8 | 7.420 | 12.1 | 6.302 | 8.0 | 2.689 | in traces | - |

Table 2: Modal compositions (m.c.) and standard deviations (s.d.) of silicate melt pockets in ultramafic xenoliths from the Bakony - Balaton Highland Volcanic Field.

Amphiboles (amp-I), occurring as residual phases in the melt pockets, and empty bubbles (bub) have been ignored from the modal composition.

Letter n indicates number of melt pockets studied; olivine-II, spinel-II, clinopyroxene-II, glass, carbonate indicate phases forming the melt pockets.

Szb55: This is an equigranular textured lherzolite. The olivines, orthopyroxenes and clinopyroxenes are usually elongated (2.0 mm long and 1.0 mm wide) displaying moderate shape preferred orientation, showing no internal strain features. The grain boundaries are straight or gently curved, triple junctions are abundant.

Silicate melt pockets have curvilinear boundaries and are usually elongated forming thin (1.0 – 2.0 mm wide, several mm to cm long) continuous melt zones parallel to the mantle phases (Fig. 16a). Some of them however form large melt patches (up to 6.0 mm, in diameter) containing resorbed amphiboles (Fig. 16b).

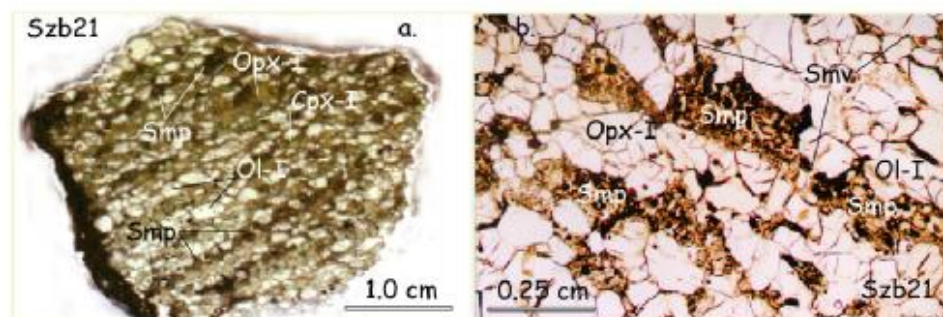


Fig. 14: Distribution of silicate melt pockets and veins in Szb21 equigranular spinel lherzolite.
a., Silicate melt pocket - rows running parallel with the plane of the elongated primary mantle minerals. Scanned thin section of sample Szb21.
b., Silicate melt pockets connected to each other by silicate melt veins. The silicate melt pockets are composed of fine grained, newly formed mineral phases and interstitial silicate glass, whereas the veins contain predominantly contain silicate glass. Photomicrograph of sample Szb21, plane polarized light, 1N.

Ol-I - mantle olivine, Opx-I - mantle orthopyroxene, Cpx-I - mantle clinopyroxene, Smp - Silicate melt pocket, Smv - silicate melt vein.



Fig. 15: Distribution of silicate melt pockets and texture of carbonate-bearing silicate melt pocket in Szb50 coarse grained inequigranular olivine clinopyroxenite.
a., Silicate melt pocket - zone cross cutting the olivine clinopyroxenite. Scanned thin section of sample Szb50.
b., Photomicrograph of a carbonate - bearing silicate melt pocket bulding up the melt zone in sample Szb50. Plane polarized light, 1N.

Ol-I - primary mantle olivine, Cpx-I - primary mantle clinopyroxene, Opx-I - mantle orthopyroxene, Smp - Silicate melt pocket, Ol-II - melt pocket olivine, Cpx-II - melt pocket clinopyroxene, Sp-II - melt pocket spinel, Gl - silicate glass, Cb - melt pocket carbonate.

Melt pockets are composed of euhedral clinopyroxenes, olivines (up to 0.2 mm in diameters) and fine, black spinels (up to 20 microns) as well as large rounded carbonate aggregates and pale brown interstitial glass (Table 2, Fig. 16b). Silicate melt pockets are often meet or connected to each other by thin (up to 150 microns wide) silicate melt veins composed predominantly of pale brown to colorless silicate glass.

5.3.2. Spinel peridotites with silicate melt pockets without carbonate

Szb04: Sample Szb04 is an equigranular textured spinel lherzolite. The olivines, orthopyroxenes and clinopyroxenes form up to 2.0 mm large tabular grains. These phases have straight grain boundaries with abundant triple junctions. Dark brown spinel occurs either as elongated (up to 1.5 mm) interstitial phases or as rounded or cubic inclusions in olivines. Silicate melt pockets form irregular shaped patches up to 2.0 mm in diameter. Melt pockets are composed of euhedral clinopyroxene, olivine and black spinel crystals (up to 0.2 mm, in diameter) and colorless interstitial glass. A further characteristic of these melt pockets is the presence of large amount of empty bubbles (Fig. 17b). Silicate melt pockets are connected to each other by thin (up to 120 microns wide) silicate melt veins composed predominantly of colorless silicate glass.

Szb52: Sample Szb52 is a protogranular textured spinel harzburgite. The olivines, orthopyroxenes and clinopyroxenes are usually 5.0-6.0 mm large (up to 1.5 cm) tabular grains showing no internal features. Triple junctions among them are frequent. A few black spinels occur as rounded inclusions of olivines.

Silicate melt pockets form irregular patches (up to 7.0 mm, in diameter) among the mantle phases with curvilinear boundaries towards them (Fig. 17a). Melt pockets are composed of euhedral clinopyroxenes, olivines (up to 0.1 mm, in diameter), brown spinels (up to 50 microns) and colorless interstitial glass. Furthermore, large (up to 2.0 mm) resorbed amphiboles occasionally occur in the melt pockets. Silicate melt veins do not occur in this xenolith.

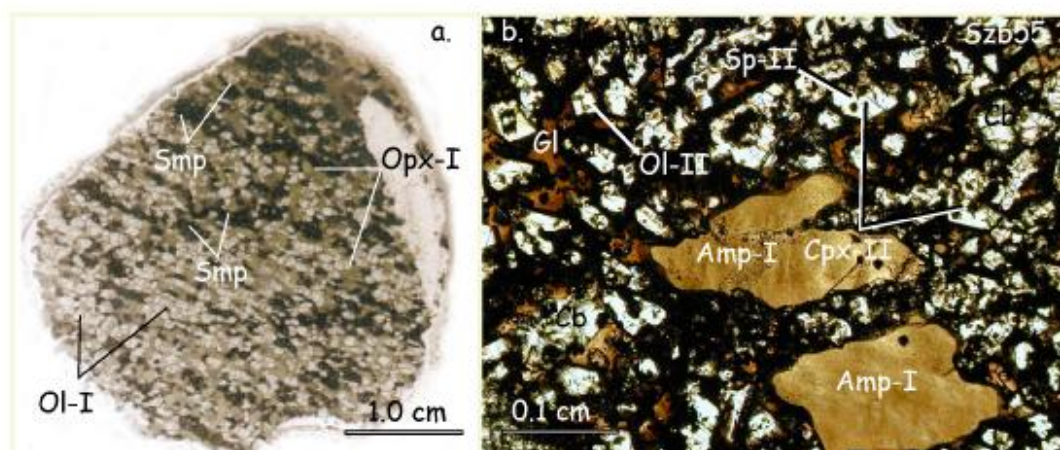


Fig. 16: Distribution of silicate melt pockets in Szb55 equigranular spinel lherzolite.
a., Silicate melt pocket - rows running parallel with the plane of the elongated primary mantle minerals. Scanned thin section of sample Szb55.
b., Resorbed primary mantle amphibole in carbonate - bearing silicate melt pocket. The silicate melt pockets are composed of fine grained, newly formed mineral phases and interstitial silicate glass. Photomicrograph of sample Szb55, plane polarized light, 1N.

Ol-I - mantle olivine, Opx-I - mantle orthopyroxene, Amp-I - mantle amphibole, Smp - Silicate melt pocket, Ol-II - melt pocket olivine, Cpx-II - melt pocket clinopyroxene, Sp-II - melt pocket spinel, Gl - silicate glass, Cb - carbonate.

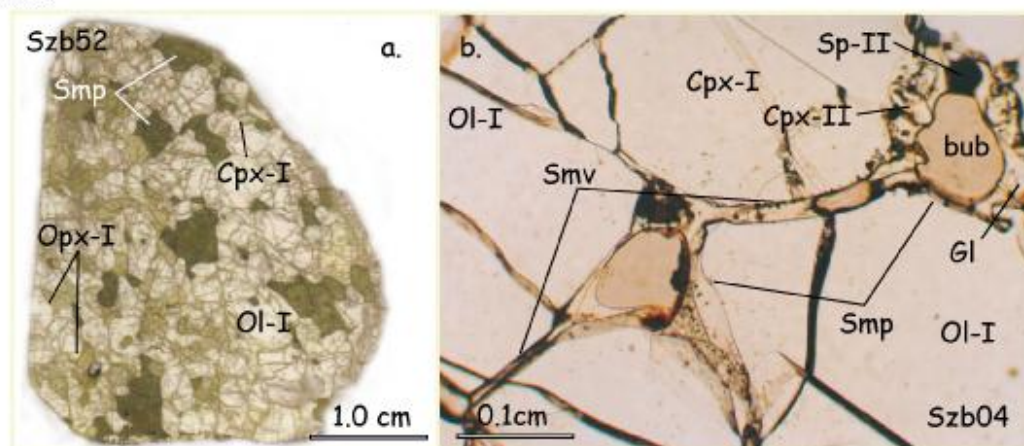


Fig. 17: Distribution of carbonate - free silicate melt accumulations in Szb04 and Szb52 lherzolites.
a., Silicate melt pockets in protogranular textured spinel lherzolite. Scanned thin section of sample Szb52.
b, Photomicrograph of a carbonate - free silicate melt pocket and veins in Szb04 equigranular spinel lherzolite. Plane polarized light, 1N.

Ol-I - mantle olivine, Cpx-I - mantle clinopyroxene, Opx-I - mantle orthopyroxene, Smp - Silicate melt pocket, Smv - Silicate melt vein, Cpx-II - melt pocket clinopyroxene, Sp-II - melt pocket spinel, Gl - silicate glass, bub - empty bubble.

6. Analytical techniques

Microprobe analyses were carried out using a JEOL Superprobe JXA-8600 WDS at the Department of Earth Sciences, University of Florence and a JEOL Superprobe JXA-8200 WD/ED at the Geocenter Copenhagen. For the analyses in Florence, an accelerating voltage of 15 kV was used, with a 10 nA sample current and a beam diameter of 5 microns, except for H₂O-bearing minerals and silicate glass, for which a defocused beam in size of 10 microns was used. Counting times were 20 seconds for each element. For the analyses in Copenhagen the accelerating voltage was 15 kV, with a 15 nA probe current and a beam size of 5 microns for all analyses. The counting time was 10 seconds for each element. In both laboratories natural and synthetic standards were employed for the analyses, and the method of Bence & Albee (1968) was applied for correction.

Laser ablation ICP–MS measurements were carried out using an Elan 6100 ICP-MS equipped with CETAC LSX-200 laser ablation system in the Geocenter Copenhagen. A beam size of 100 microns was used for the analyses and a single line scan or raster method was applied in order to check the homogeneity of the measured phases. NIST610 and NIST612 synthetic glass standards were used as calibration standards (using the values in Pearce et al. 1997). The CaO contents of the analysed phases measured on the electron microprobe were used as the internal standard. For the silicate melt pockets, analysis of small constituents (clinopyroxenes, olivines, spinels +/- carbonates and interstitial glass) in several cases was not possible because of their small sizes. In these cases the material of the bulk melt pocket was ablated and the CaO contents of the bulk melt pocket calculated by Bali et al. (2002) was used as the internal standard. In the following these analyses are referred as bulk melt. In those samples where the compositions of different phases could be measured, the silicate glass was also measured (referred as glass) and attempts for bulk melt measurements were also carried out to check the differences and the rate of inhomogeneities. The precision and accuracy for all measured trace elements was $\leq \pm 10\%$ and mostly below $\pm 5\%$, with the exception of xenolith Szb21 and for several elements for xenoliths Szb50 and Szb01 (see in Appendix 1).

For isotopic measurements, clinopyroxenes and melt pockets were separated by electromagnetic separator followed by hand picking under a binocular microscope. Separated clinopyroxenes of 12 samples were optically free from amphibole and spinel inclusions. Clinopyroxenes were leached in 8N HCl on a hot plate for an hour in teflon beakers. The hand picked melt pockets of 3 samples were not leached. Samples were then dissolved in 7N HNO₃+HF mixture, 7N HNO₃, then 6M HCL. Pb was then separated from the dissolved material by a double pass over small pre-cleaned disposable columns loaded with 0.1ml anion

exchange resin, using 1M HBr and 7M HCl. Samples were then redissolved in 0.75ml of 0.2M HNO₃ for analysis. Pb samples were analysed using the double spike method on the Axiom multi-collector ICPMS at the Danish Lithosphere Centre, Copenhagen using methods described in detail by Baker et al. (submitted). In brief, following an on-peak zeroes measurement, samples are introduced to the MC-ICPMS using an Aridus desolvating nebuliser and analysed statically for 2 blocks of 75 x 1 sec integration. The on-peak zeroes treatment eliminates residual Pb background signals and isobaric interferences from Hg. An appropriate amount of ²⁰⁷Pb - ²⁰⁴Pb double spike is then added to the sample and it is analysed again using a similar procedure. The double spike values are then used to correct for mass bias offline using an Excel spreadsheet and an exponential approximation of Johnson and Beard (1999). Replicate analyses of SRM981 standard during this analytical session gave ²⁰⁶Pb/²⁰⁴Pb = 16.941, ²⁰⁷Pb/²⁰⁴Pb = 15.498 and ²⁰⁸Pb/²⁰⁴Pb = 36.723, in agreement with the long-term reproducibility in the lab of ²⁰⁶Pb/²⁰⁴Pb = 16.9416±11, ²⁰⁷Pb/²⁰⁴Pb = 15.4999±11 and ²⁰⁸Pb/²⁰⁴Pb = 36.7258±31. Low Pb contents in several of the samples analysed here have resulted in somewhat larger internal errors for individual analyses.

The waste collected during Pb-chemistry was used for Sr column chemistry. Sr was separated from other elements on a conventional cation exchange chromatography column followed by an extra clean up step using Eichrom Sr-specific resin (see Waight et al. 2002 for more details). Sr samples were loaded onto Re filaments in a mixture of H₃PO₄ and TaF activator and then analyzed automatically in dynamic peak jumping mode on a VG sector 54 TIMS at the Geological Institute, University of Copenhagen. Replicate analyses of Sr standard SRM987 over the period of analysis gave ⁸⁷Sr/⁸⁶Sr = 0.710232±17 (2SD, n=8), in good agreement with the long term average of the instrument in 2002 (0.710236±19). All chemical separations were carried out in clean room environments and the measured Sr and Pb blanks were 30 pg and 100 pg respectively.

7. Mineral chemistry

In the followings the detailed description of major and trace elements of minerals is given in those groups determined by petrographical features.

7.1. Major elements

7.1.1. Olivines

Comparing olivine compositions in all rock types it can be established that they cover a very narrow range. With the exception of the olivines in Szb62 and Szb63 websterite veined lherzolites and the mantle olivines in Szb50 olivine clinopyroxenite, no significant differences can be observed among the different groups. The olivines of these latter samples have lower mg# compare to the others, and the mantle olivines of sample Szb50 have lower NiO and CaO contents as well.

7.1.1.1. Orthopyroxene-rich websterites

7.1.1.1.1. Mantle olivines

Mantle olivines in orthopyroxene-rich websterites and harzburgite wall rock Szb59/1 show a restricted composition (Table 3) with mg# from 90.4 to 91.1, NiO 0.33 - 0.42 wt% and CaO between 0.06 and 0.08 wt%. Olivines in Szb59/2 (the orthopyroxene-rich vein of sample Szb59) show zonation, as the thin (up to 15 microns) rim of the olivines have lower mg# (89.5) and NiO (0.35 wt%), and higher CaO (0.08 wt%) compared to the olivine core compositions (Table 3).

7.1.1.1.2. Melt pocket olivines

Olivines in the melt pockets of orthopyroxene-rich websterites and the wall rock peridotite Szb59/1 have mg# 87.8 to 92.4, NiO 0.23 to 0.31 wt% and CaO 0.13 to 0.17 wt%. Compared to the mantle olivines the mg#-range is wider, the NiO content is lower and the CaO content is higher in the melt pocket olivines (Table 3).

7.1.1.2. Spinel lherzolites with websterite and clinopyroxenite vein(s)

There are no significant differences between the compositions of vein olivines and wall rock olivines in individual samples, but olivines in the different samples show certain deviations (Table 3). Olivines of the websterite veined lherzolite Szbk99/11 have the highest

mg# (90.8), whereas the clinopyroxene veined lherzolite Szg01 have the lowest mg#-values (87.6-88.6). Olivines of samples Szb62 and Szb63 have intermediate mg# (Table 3). The NiO contents show similar distribution i.e. increase with increasing mg# (0.23 to 0.33 wt% in Szg01 to 0.40 to 0.47 wt% in Szgk99/11). Other elements do not show unequivocal differences, as CaO is between 0.07 and 0.12 wt%.

7.1.1.3. Spinel peridotites and pyroxenites with silicate melt pockets and veins

7.1.1.3.1. Mantle olivines

With the exception of olivine clinopyroxenite Szb50 the composition of mantle olivines have a narrow range with mg# between 88.7 and 90.8, NiO between 0.32 and 0.38 wt% and CaO between 0.04 and 0.08 wt%. Olivines of Szb50 olivine clinopyroxenite have lower mg# and NiO content compared to the peridotitic xenoliths, with no difference in CaO content (Table 3).

7.1.1.3.2. Silicate melt pocket olivines

The olivines of carbonate-bearing melt pockets are usually richer in CaO, but show lower NiO and mg# values compared to those in the carbonate-free melt pockets (Table 3).

7.1.1.3.2.1. Olivines in carbonate-bearing silicate melt pockets

Olivines in carbonate-bearing melt pockets of Szb21 and Szb55 lherzolites and Szb50 olivine clinopyroxenite have mg# from 90.1 to 92.6, NiO from 0.22 to 0.39 wt%, CaO from 0.15 to 0.29 wt%. The olivines in the melt pockets of sample Szb59/1 which also contain carbonate have similar mg# and NiO content (90.3 and 0.31 wt%, respectively), but slightly lower CaO content (0.13 wt%). The melt pocket olivines always have higher mg# and CaO content compared to the coexisting mantle olivines with a wider range of NiO (Table 3).

7.1.1.3.2.2. Olivines in carbonate-free silicate melt pockets

Olivines in carbonate-free silicate melt pockets of Szb04 lherzolite and Szb52 harzburgite have mg# between 92.1 and 94.4, NiO between 0.34 and 0.39 wt% and CaO between 0.15 and 0.27 wt%. These values are always higher than those in the coexisting mantle olivines. The olivines in the melt pockets of sample Szb36 and Szg08 (which are also carbonate-free melt pockets) fall into the same range, whereas the melt pocket olivines of sample Szb59/2 show lower values (Table 3).

Table 3. olivine compositions

7.1.2. Orthopyroxenes

The orthopyroxenes in orthopyroxene-rich websterites and in their wall rocks show the lowest Al_2O_3 contents, whereas those in the samples Szb62 and Szb63 containing websterite veins have the highest Al_2O_3 values (Table 4, Fig. 18). Usually no differences between the wall rock and vein orthopyroxenes can be observed, with the exception of samples Szb62 and Szb63. Considering the other components, orthopyroxenes vary in a narrow compositional range having usually higher mg#s compared to those in the coexisting mantle olivines (Table 3 and Table 4). The orthopyroxenes of the studied xenoliths show larger compositional range than those studied by Downes et al. (1992) from the same locality (Fig. 18).

7.1.2.1. Orthopyroxene-rich websterites

The mg# of orthopyroxene in the orthopyroxene-rich websterites is between 91.1 and 92.0, which are somewhat higher than the coexisting mantle olivines. The Al_2O_3 contents of orthopyroxenes in these websterites and wall rocks is relatively low, varying between 2.38 and 2.77 wt%, with the highest value in the peridotitic wall rock of the composite xenolith Szb59 (referred as Szb59/1) and the lowest values in sample Szb36. Na_2O contents of orthopyroxenes are slightly variable between 0.02 and 0.15 wt%. Compared to the composition of orthopyroxenes reported from lherzolites by Downes et al. (1992) the Al_2O_3 of these orthopyroxenes is low, whereas the mg#-values are high (Fig. 18a).

7.1.2.2. Spinel lherzolites with websterite and clinopyroxenite vein(s)

Orthopyroxenes in xenoliths Szb62, Szb63 and Szg01 have significantly lower mg# but higher Al_2O_3 and Na_2O contents compared to those in Szgk99/11 and in the peridotites studied by Downes et al. (1992) from the area. As the chemical differences between these samples can be observed in all mineral compounds, chemical division is used in the followings.

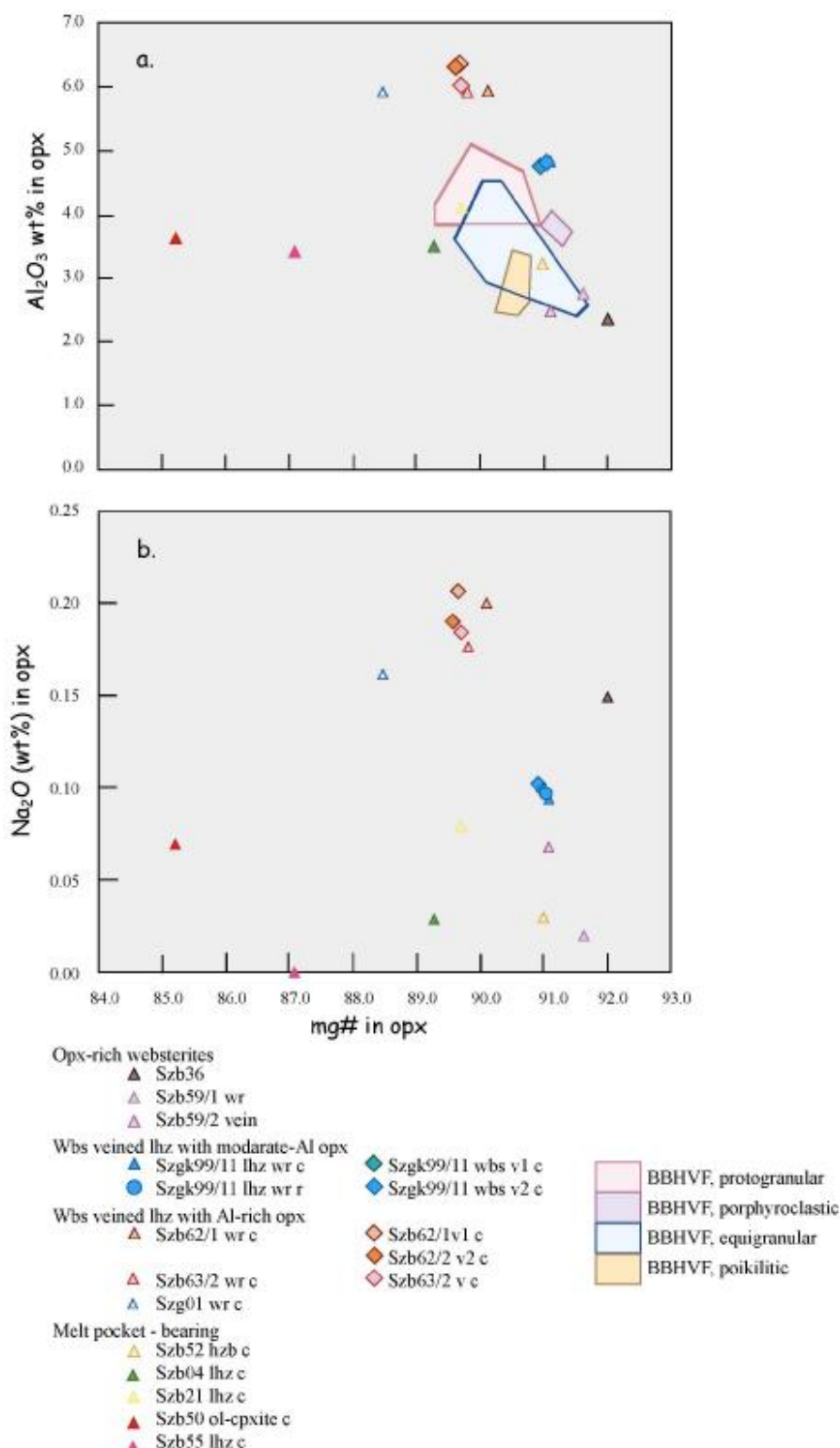


Fig. 18: Mg# vs Al₂O₃ (a) and mg# vs Na₂O (b) diagrams for orthopyroxenes of Bakony - Balaton Highland ultramafic xenoliths, this study. Mg# was calculated as $100 \cdot (\text{Mg}^{2+}) / (\text{Mg}^{2+} + \text{Fe}^{2+})$. wr - wall rock, v - vein, c - core of opx, r - rim of opx. The composition fields of orthopyroxenes from ultramafic xenoliths with different textures from the BBHVF reported by Downes et al. (1992) are also shown for comparison.

Table 4. Opx compositions

No differences were observed between the compositions of orthopyroxenes in the veins and the wall rock for xenolith Szgk99/11 (lherzolite veined dunite and websterite veined lherzolite, respectively) containing orthopyroxenes with mg# varying from 90.9 to 91.1, Al_2O_3 between 4.75 and 4.83 wt% and Na_2O contents 0.09-0.10 wt%. These compositions are very similar to those observed in orthopyroxenes of protogranular peridotites by Downes et al. (1992) from the BBHVF (Fig. 18a). As the orthopyroxenes in this xenolith has intermediate Al_2O_3 content between the orthopyroxenes of Al-poor opx-rich websterite and the websterite and clinopyroxenite veined Szb62, Szb63 and Szg01 xenoliths (Fig. 18) this sample will be referred as websterite veined lherzolite with moderate Al-orthopyroxenes. Websterite veined lherzolites Szb62, Szb63 differ from the previously mentioned xenolith Szgk99/11, as there are slight differences between the orthopyroxenes found in veins or in the wall rock, with the wall rock orthopyroxenes having slightly lower Al_2O_3 contents (5.92-5.98 wt%) compared to those in the veins (6.04-6.39 wt%). However, they show no differences in mg# (89.7-90.2) or Na_2O contents (0.18 to 0.24 wt%). However the wall rock orthopyroxenes of clinopyroxene veined lherzolite Szg01 have somewhat lower mg# and Na_2O contents than observed in these xenoliths. The group of these xenoliths will be referred as websterite and clinopyroxenite veined lherzolites with Al-rich orthopyroxenes.

7.1.2.3. *Spinel peridotites and pyroxenites with silicate melt pockets and veins*

Orthopyroxenes of melt pocket bearing xenoliths have a large composition range compared to the previously mentioned groups as their mg# varies from 85.2 to 91.0, Al_2O_3 contents are between 3.25 and 4.12 wt% and Na_2O contents are between 0.00 and 0.08 wt%. The lowest mg# is in Szb50 olivine clinopyroxenite sample, whereas the highest one is in Szb52 harzburgite sample.

7.1.3. Clinopyroxenes

Clinopyroxenes of the different xenoliths show wide compositional range from augitic to diopsidic (Table 5, Fig. 19). Mantle clinopyroxenes of melt pocket - bearing peridotites usually show the highest CaO and the lowest Al_2O_3 and Na_2O contents. In contrast, cores of clinopyroxenes in websterite and clinopyroxene veined lherzolites Szb62, Szb63 and Szg01 have the highest Na_2O and lowest CaO contents (Fig. 20). The mantle clinopyroxenes follow the compositional trends drawn by the peridotites studied by Downes et al (1992) however

they have a wider compositional range (Fig. 20). The melt pocket clinopyroxenes deviate from these trends towards high Al contents.

The nomenclature of Morimoto (1989) is used.

7.1.3.1. Orthopyroxene-rich websterites

7.1.3.1.1. Mantle clinopyroxenes

Mantle clinopyroxenes of orthopyroxene-rich websterites are chromian-aluminian-augites and chromian-aluminian-diopsides having mg# between 87.8 and 92.3, which is a wider range compared to the mg#s of coexisting olivines or orthopyroxenes. Furthermore, clinopyroxenes are poor in TiO₂ (up to 0.71 wt%) and Al₂O₃ (3.10 to 4.87 wt%), with the highest values in Szb59/1 (harzburgite wall rock of Szb59/2, orthopyroxene-rich websterite), and also rich in Cr₂O₃ (0.89 to 1.39 wt%). Their Na₂O contents are variable with particularly high value in xenolith Szb36 (1.54 wt%) (Table 5).

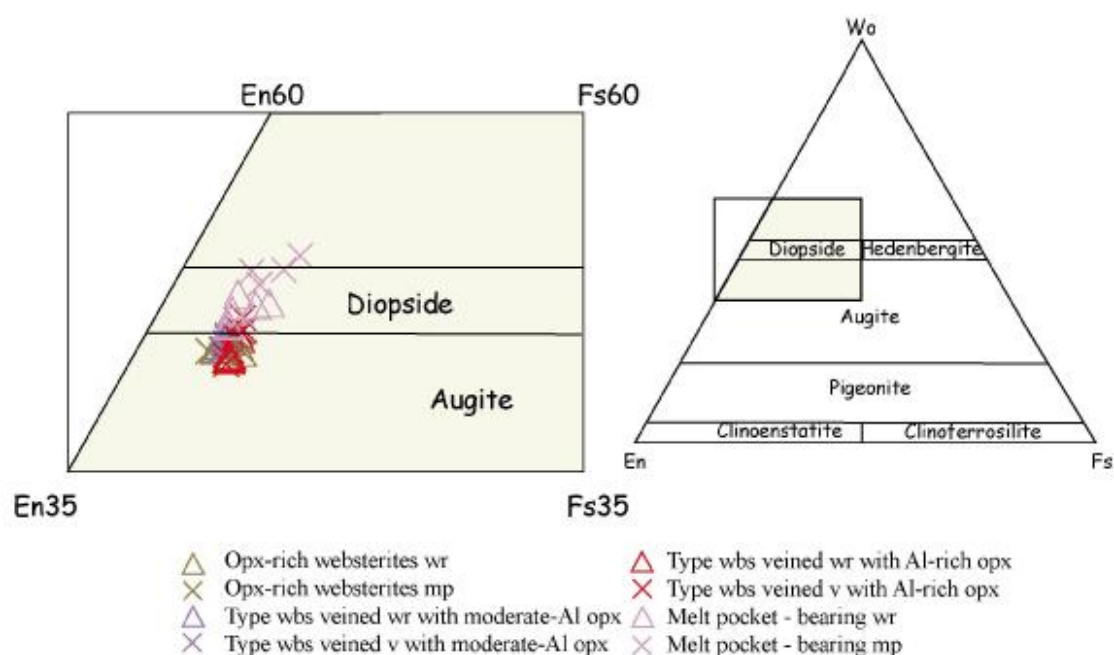


Fig. 19: Composition of Bakony - Balaton Highland clinopyroxenes, this study in Enstatite - Wollastonite - Ferrosillite diagram. wr - wall rock, v - vein, mp - melt pocket.

7.1.3.1.2. Melt pocket clinopyroxenes

Melt pocket clinopyroxenes in the same samples are chromian-aluminian-titanoan - augites having mg# between 87.9 and 91.8, which are usually higher than in the coexisting mantle clinopyroxenes (with the exception of orthopyroxene-rich vein, Szb59/2). Their TiO₂ (0.13 to 1.26 wt%), Al₂O₃ (5.40 to 5.90 wt%) and Cr₂O₃ (1.17 to 2.63 wt%) contents are higher than in the mantle clinopyroxenes (Table 5, Fig. 20), whereas they usually contain less Na₂O (between 0.82 and 0.96 wt%) (Table 5, Fig. 20).

7.1.3.2. Spinel lherzolites with websterite and clinopyroxenite vein(s)

No clear differences can be observed between the vein clinopyroxenes and wall rock clinopyroxenes inside an individual sample. The only difference (with the exception of sample Szgk99/11) is the zonation of clinopyroxenes, as the spongy rims of both vein and wall rock clinopyroxenes of xenoliths Szb62, Szb63 and Szg01 differ from the composition of their cores (Table 5, Fig. 20). Furthermore, the compositions of clinopyroxenes in websterite veined lherzolite Szgk99/1 strongly differ from those in xenoliths Szb62, Szb63 and Szg01 (Table 5, Fig. 20) as was also observed in orthopyroxene compositions. All clinopyroxenes of this group belong to the Al-augitic i.e. Type II clinopyroxenes.

7.1.3.2.1. Websterite veined lherzolite with moderate Al-orthopyroxenes

Clinopyroxenes in xenolith Szgk99/11 are chromian-aluminian-(titanoan) - augites in composition. They have restricted mg# range between 90.3 and 90.7. Both cores and rims of the pyroxenes have low TiO₂ (0.32 to 0.40 wt%) and moderate Al₂O₃ (5.87 and 5.94 wt%) whereas high Cr₂O₃ (1.00 to 1.11 wt%) contents (Table 5). Na₂O contents are also in a narrow range (1.11 to 1.13 wt%) (Table 5, Fig. 20).

7.1.3.2.1. Websterite and clinopyroxenite veined lherzolite with Al-rich orthopyroxenes

Clinopyroxenes in samples Szb62, Szb63 and Szg01 have aluminian-chromian-(titanoan) - augitic compositions. Their mg#'s vary between 86.9 and 89.9, which is lower than observed in Szgk99/11 xenolith. Al₂O₃ and TiO₂ contents are higher whereas Cr₂O₃ contents are lower in these samples (5.71 to 8.80 wt%; 0.76 to 1.23 wt% and 0.06 to 0.72 wt%, respectively). Na₂O contents show a high variability from 0.56 to 1.97 wt%.

Table 5. cpx composition, page 1.

Table 5. cpx composition page 2

The clinopyroxenes of these three samples have strong zonation (Table 5, Fig. 20) which is petrographically manifested in the presence of spongy rims (Fig. 13d). The cores of clinopyroxenes always have higher Al_2O_3 and lower CaO and Na_2O contents compared to the rims compositions which later ones trend towards chromian-diopsidic compositions (Table 5). The cores have higher Na and lower Ca contents than that was observed in the peridotites studied by Downes et al. (1992).

7.1.3.3. *Spinel peridotites and pyroxenites with silicate melt pockets and veins*

7.1.3.3.1. Mantle clinopyroxenes

Mantle clinopyroxenes of melt pocket – bearing xenoliths are chromian-aluminian (-titanoan) - diopsides. Their mg# varies between 87.5 and 91.4 with the lowest value in sample Szb50 olivine clinopyroxenite. They have low TiO_2 , Al_2O_3 , Na_2O and Cr_2O_3 contents (0.17 to 0.47 wt%, 2.95 to 4.48 wt%, 0.18 to 0.77 wt% and 0.21 to 0.78 wt%, respectively).

7.1.3.3.2. Melt pocket clinopyroxenes

Melt pocket clinopyroxenes are chromian-aluminian-titanoan (ferroan) - diopsides and always have higher TiO_2 , Al_2O_3 , Na_2O and Cr_2O_3 contents than coexisting mantle clinopyroxenes.

7.1.3.3.2.1. Clinopyroxenes in carbonate-bearing melt pockets

Clinopyroxenes in carbonate-bearing melt pockets of samples Szb21, Szb50 and Szb55 have mg# between 86.3 and 89.7, which are always lower than the mg#s in the coexisting mantle clinopyroxenes (Table 5). Their TiO_2 , Al_2O_3 and Cr_2O_3 contents are higher than in the mantle clinopyroxenes (1.21 to 2.08 wt%; 8.65 to 8.74 wt% and 0.65 to 1.82 wt%, respectively). The clinopyroxenes in carbonate-bearing melt pockets of harzburgite wall rock Szb59/1 have lower TiO_2 and Al_2O_3 contents than these melt pocket clinopyroxenes, but they show the same distribution, i.e. increase in both components (Table 5) compared to the mantle phase.

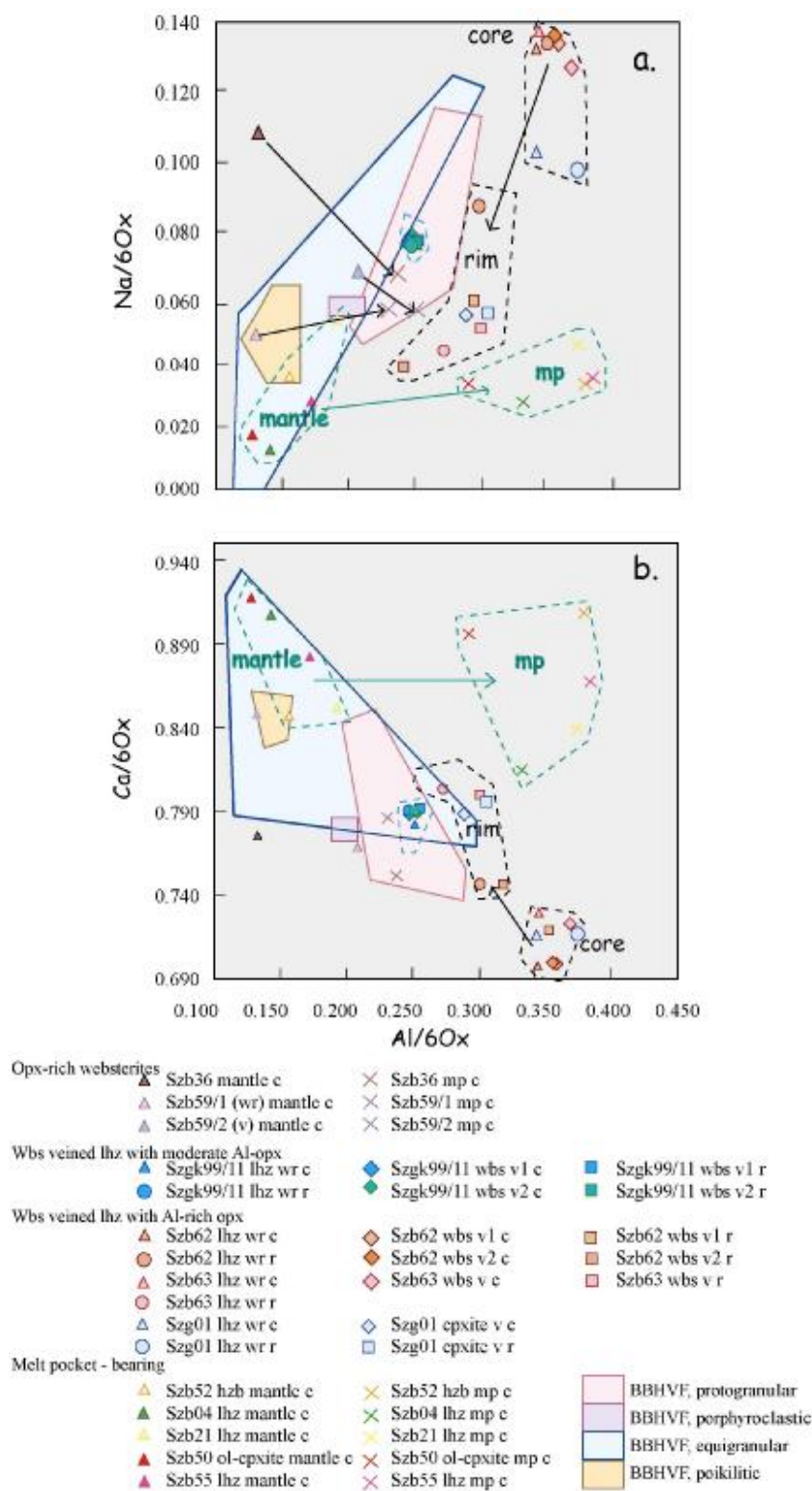


Fig. 20: Na vs. Al and Ca vs. Al diagrams for the clinopyroxenes of the BBHVF ultramafic xenoliths, this study. The Al, Na, Ca values are given in cation numbers calculated for 6 oxygens. The composition fields of clinopyroxenes from ultramafic xenoliths with different textures from the BBHVF reported by Downes et al. (1992) are also shown for comparison. wr - wall rock; v - vein; mantle - mantle clinopyroxene; mp - melt pocket clinopyroxene, c - core, r - rim.

7.1.4. Spinels

Spinels show the most widespread compositions (Table 6, Fig. 21) among all mineral phases. Most of them however follow a well defined trend in mg# vs cr# diagram falling in a narrow range with the lowest cr# and highest mg# in spinels of xenoliths Szb62 and Szb63 and the highest cr# and lowest mg# in the mantle spinels of the orthopyroxene-rich websterites (Fig. 21). Spinels of other samples usually have intermediate compositions between these, although deviations are observed, mainly by both the mantle and melt pocket spinels of melt pocket - bearing samples (Fig. 21). Either the studied spinels have wider compositional range than those studied by Downes et al. (1992) (Fig. 21).

7.1.4.1. Orthopyroxene-rich websterites

7.1.4.1.1. Mantle spinels

Mantle spinels of orthopyroxene-rich websterites have the highest cr#-values among all rock types (from 42.5 to 54.2). They have low mg# varying between 70.5 and 73.5. The TiO₂ contents fall between 0.03 and 0.16 wt%, and the NiO contents are relatively low (0.19 to 0.24 wt%).

7.1.4.1.2. Melt pocket spinels

Melt pocket spinels have a diverse compositional range, as is seen from their mg#s (71.3 to 80.9). Compared to the mantle spinels, they have much lower cr# values (23.8 to 36.8) and higher TiO₂ and NiO contents (0.10 to 1.47 wt% and 0.19 to 0.39 wt% respectively in melt pocket phases) (Table 6).

7.1.4.2. Spinel lherzolites with websterite and clinopyroxenite vein(s)

Spinel compositions of this group have a restricted range, with relatively low cr#s and high mg#s. Differences in spinel compositions confirm the previous observation that the Szgk99/11 xenolith and samples Szb62, Szb63 and Szg01 form distinct groups (Fig. 21). Vein and wall rock spinels are compositionally similar.

7.2.3.2.1. Websterite veined lherzolite with moderate Al-orthopyroxenes

Spinels in xenolith Szgk99/11 have relatively low cr# (19.8 to 20.1) and high mg# (from 80.5 to 81.1), with the exception a spinel rim that trending towards higher cr# and lower mg# (41.9 and 73.9 respectively) (Fig. 21). The TiO₂ contents vary between 0.21 and 0.26 wt%,

the NiO is between 0.32 to 0.41 wt%. The spinel rim shows deviations from the core compositions with much higher TiO₂ and lower NiO contents (Table 6).

7.2.3.2.1. Websterite and clinopyroxenite veined lherzolite with Al-rich orthopyroxenes

Spinel of xenoliths Szb62, Szb63 and Szb01 have also very uniform compositions with cr# between 1.3 and 8.9 and mg# between 79.8 and 82.9 with the lowest cr#-values in spinels of clinopyroxenite vein of xenolith Szb01. The NiO contents of these spinels are the highest, varying from 0.36 to 0.42 wt%, whereas their TiO₂ contents are between 0.18 and 0.41 wt% with the highest TiO₂ in the vein spinels of Szb01. The cr#s of spinels in these xenoliths are lower than those were observed in the spinels of peridotites studied by Downes et al. (1992).

7.1.4.4. *Spinel peridotites and pyroxenites with silicate melt pockets and veins*

Spinel of this group show the widest compositional range (Fig. 21). Both mantle and melt pocket spinels are very variable in composition.

7.1.4.4.1. Mantle spinels

Mantle spinels usually show relatively low cr#-values with a wide range in mg#'s. Only spinels of Szb52 harzburgite have relatively high cr# (35.6) the other samples are between 9.6 and 23. Mg#s in the majority of the samples fall into the 76.2 to 80.6 range, with the exception of spinels from sample Szb50 olivine clinopyroxenite that have lower values (Table 6). Whereas the TiO₂ contents show high variability (0.05 to 0.26 wt%), the NiO contents fall between 0.21 and 0.35 wt%.

7.1.4.4.2. Melt pocket spinels

No unequivocal differences can be found between the spinels in different types of melt pockets (i.e. carbonate-bearing or carbonate-free). They usually have higher mg#s and TiO₂ compared to the coexisting mantle spinels but their cr# is very variable (Table 6, Fig. 21). Their NiO contents are between 0.25 and 0.37 wt%.

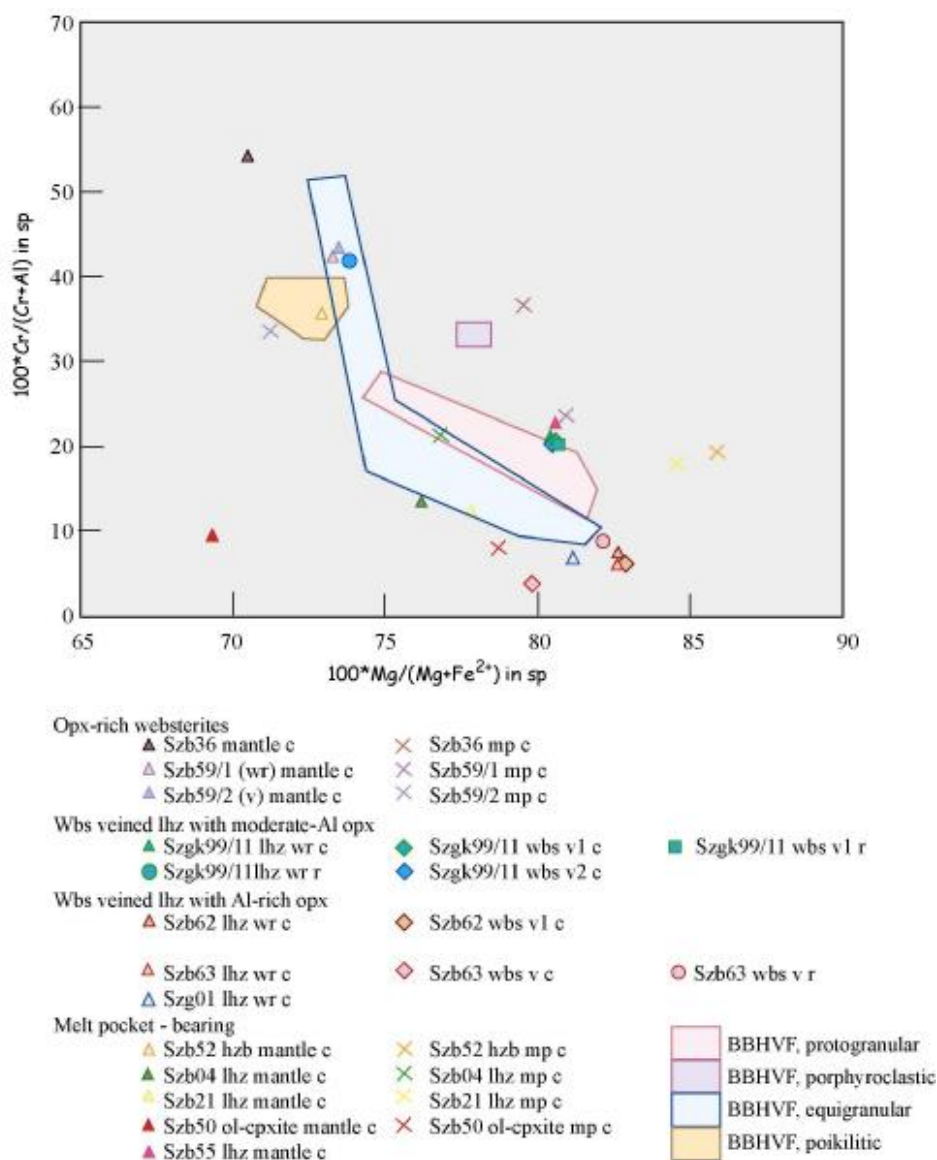


Fig. 21: Composition of spinels in Bakony - Balaton Highland ultramafic xenoliths, this study. Cr, Al, Mg, Fe²⁺ are cation numbers calculated for 32 oxygens. Fe²⁺ was calculated based on spinel stoichiometry. The composition fields of spinels from ultramafic xenoliths with different textures from the BBHVF reported by Downes et al. (1992) are also shown for comparison. wr - wall rock, v - vein, mantle - mantle spinel, mp - melt pocket spinel, c - core, r - rim.

Table 6. spinel compositions

7.1.5. Amphiboles

| Rock type | Opx-rich wbs | Hzb | Lhz |
|------------------------------------|-------------------------------|-------------------------------|-------------------------------|
| Sample amp type No. of anal. | Szb36 res in mp av of 3 | Szb52 res in mp av of 2 | Szb55 res in mp av of 2 |
| SiO ₂ | 44.8 | 43.9 | 43.1 |
| TiO ₂ | 0.30 | 0.65 | 1.73 |
| Al ₂ O ₃ | 12.3 | 13.6 | 14.0 |
| Cr ₂ O ₃ | 2.33 | 1.71 | 0.98 |
| FeO | 3.67 | 3.94 | 5.65 |
| MnO | 0.06 | 0.08 | 0.06 |
| MgO | 18.9 | 18.7 | 17.3 |
| CaO | 10.5 | 11.4 | 11.7 |
| Na ₂ O | 3.41 | 2.55 | 2.49 |
| K ₂ O | 0.59 | 0.95 | 0.95 |
| Total | 96.8 | 97.4 | 98.0 |
| Si | 6.408 | 6.253 | 6.074 |
| Ti | 0.032 | 0.069 | 0.183 |
| Al | 2.082 | 2.287 | 2.325 |
| Cr | 0.264 | 0.192 | 0.109 |
| Fe | 0.439 | 0.470 | 0.666 |
| Mn | 0.007 | 0.009 | 0.007 |
| Mg | 4.024 | 3.980 | 3.635 |
| Ca | 1.604 | 1.738 | 1.767 |
| Na | 0.947 | 0.705 | 0.680 |
| K | 0.107 | 0.172 | 0.171 |
| sum | 15.914 | 15.876 | 15.618 |
| mg# | 90.2 | 89.4 | 84.5 |

mg#=100*Mg/(Mg+Fe²⁺)
all Fe was calculated as Fe²⁺

Table 7: Composition of amphiboles in Bakony - Balaton Highland ultramafic xenoliths, this study. Res in mp - resorbed phase in silicate melt pocket.

Dobosi (2003). For comparison an amphibole megacryst and amphiboles from clinopyroxenite vein are also plotted. These later ones have much higher Ti than those were observed in the resorbed amphiboles, this study.

Amphiboles of orthopyroxene-rich websterite Szb36 and harzburgite Szb52 are pargasites whereas those in lherzolite Szb55 are Mg-Hastingsite (Fig. 22) after the nomenclature of Leake et al., (1997). They have high mg#s between 84.5 and 90.2 which are slightly lower than those in the coexisting mantle phases (Table 7). Resorbed amphiboles from melt pockets of samples Szb36 and Szb52 have low TiO₂ (0.3 to 0.65 wt%) and K₂O (0.59 to 0.95 wt%) and high Cr₂O₃ (1.71 to 2.33 wt%) contents. The amphibole of lherzolite Szb55 has relatively high TiO₂ (1.73 wt%) and low Cr₂O₃ (0.98 wt%) contents (Table 7). Compared to interstitial amphiboles from peridotites of the same locality (Dobosi, 2003) the resorbed phases of Szb36 and Szb52 are poor in Ti and Fe (Fig. 22), whereas rich in Cr. The amphiboles in lherzolite Szb55 have similar Ti content to those interstitial amphiboles studied by

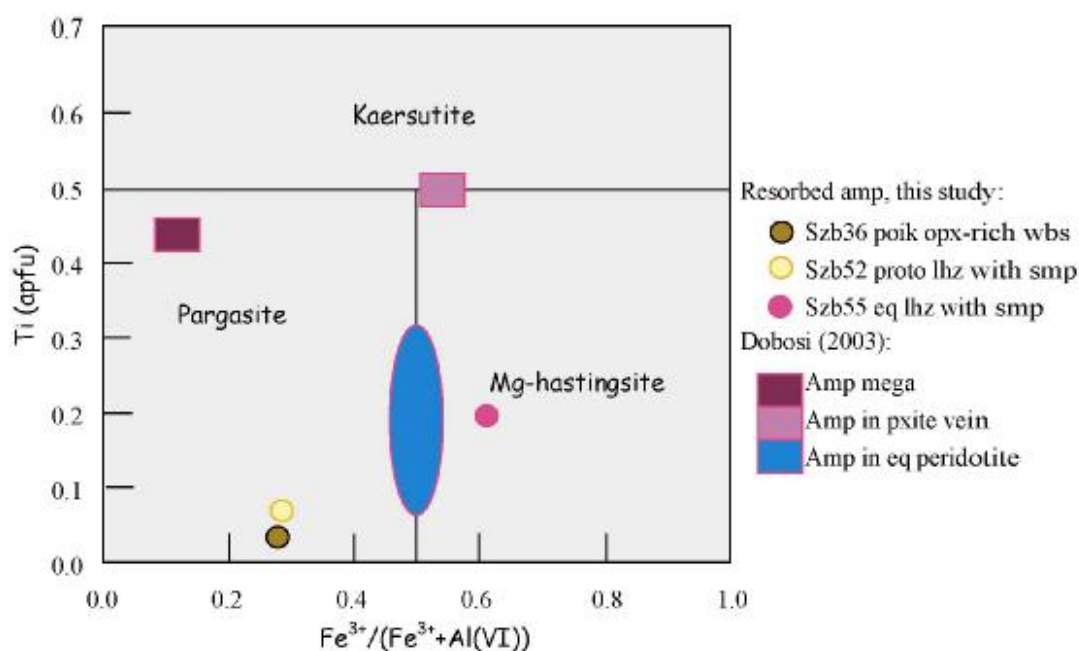


Fig. 22: Classification of amphiboles in Bakony - Balaton Highland ultramafic xenoliths, this study, based on Leake et al. (1997). Amphiboles showing different textures from the BBHVF are shown for comparison (Dobosi, 2003).
amp - mantle amphibole, smp - silicate melt pocket, mega - megacryst,
poik - poikilitic, proto - protogranular, eq - equigranular.

7.1.6. Glasses

Almost all the xenoliths contain different types of silicate melt accumulations (as primary and secondary silicate melt inclusions, silicate melt veins and silicate melt pockets). Their compositions show a very wide range from basaltic to trachy-dacitic (Fig. 23). Glasses in silicate melt pockets are the most variable, whereas the compositions of primary and secondary melt inclusions have quite restricted variations (Table 8, Fig. 23). The glass compositions inside single samples show also less variation independent of the type of glass accumulation (i.e. melt pockets, veins or inclusions) (Fig. 24).

Glass compositions are different from the host alkaline basalt (Embey-Isztin et al., 1993, Harangi unpubl.) and cover a much larger range than the calc-alkaline magmatites of the North Pannonian Basin (Harangi et al., 2001, unpubl.) (Fig. 23, 24).

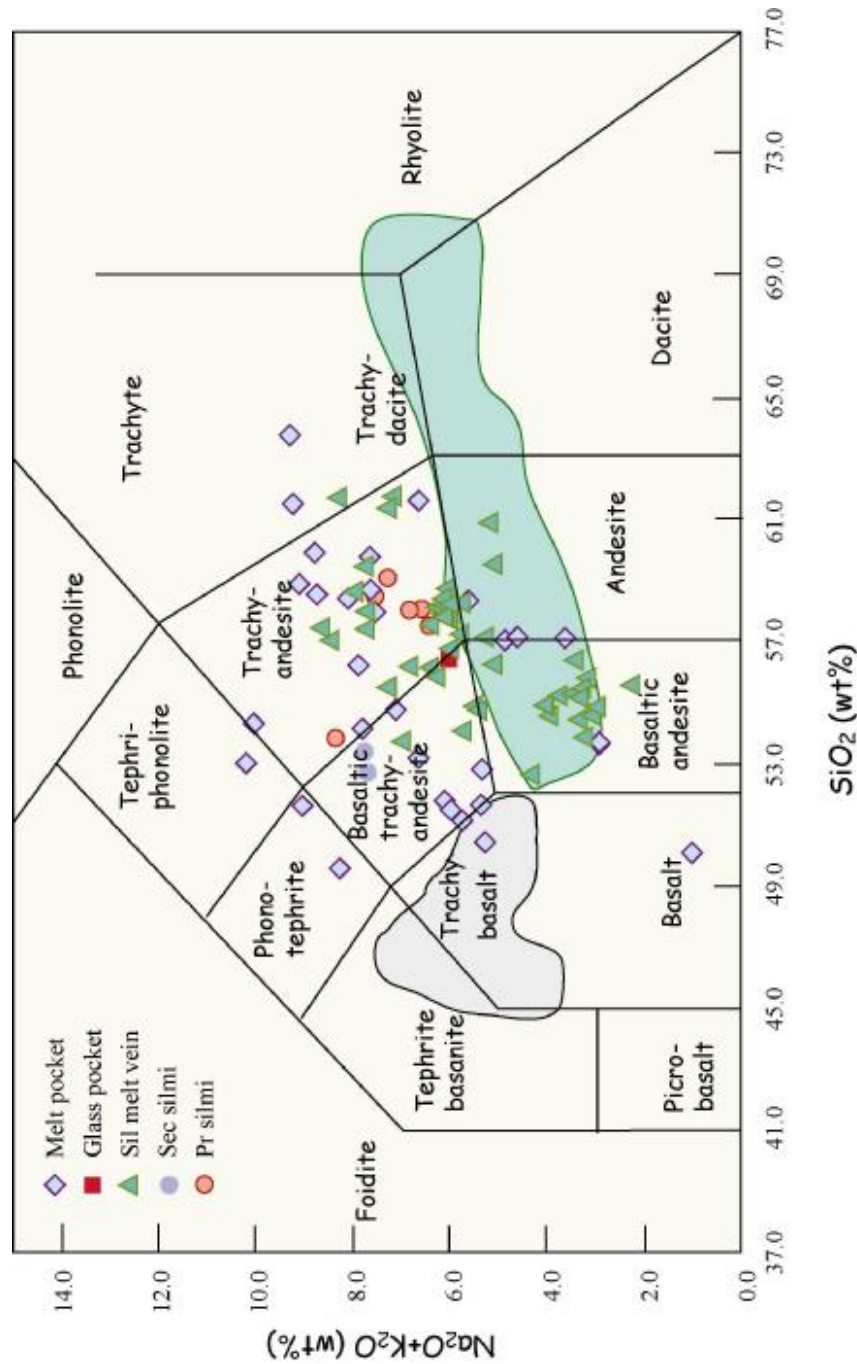


Fig. 23: Total alkali vs silica (TAS) diagram for silicate glasses in Bakony - Balaton Highland ultramafic xenoliths, this study. Different symbols indicate the different type of melt accumulations. Sil melt vein - silicate melt vein, Sec silmi - secondary silicate melt inclusion, along healed fractures. Pr silmi - primary silicate melt inclusion in spongy rims of mantle clinopyroxenes (Fig. 13d). Gray field represents the composition of Bakony - Balaton Highland alkali basalts (Embey-Isztin et al., 1993 and Harangi unpubl), green field show the composition of Northern Pannonian Basin Calc-alkaline volcanites (Harangi et al., 2001, unpubl). Field boundaries are after Le Bas et al. (1986).

7.1.6.1. Orthopyroxene-rich websterites

In Szb36 orthopyroxene-rich websterite and wall rock harzburgite Szb59/1, silicate glass was analyzed in silicate melt pockets. In orthopyroxene-rich websterite Szb59/2, in addition to the silicate melt pocket glasses, the composition of glass veins and a primary silicate melt inclusion trapped in the spongy rim of mantle clinopyroxene have also been determined (Table 8). Considering all elements, the glasses of the different xenoliths (i.e. Szb36 and Szb59) have a narrow compositional range (Table 8, Fig. 24) with the exception of the SiO₂ content which is between 50.9 and 62.8 wt% in xenolith Szb59, and between 57.2 and 60.6 wt% in xenolith Szb36. The glasses have medium CaO, MgO, Al₂O₃ contents compared to the glass accumulations of the other samples (2.99 to 6.77 wt%, 1.69 to 4.64 wt% and 15.9 to 21.0 wt%, respectively in sample Szb59, compared to 2.26 to 2.55 wt%, 2.64 to 3.04 wt% and 20.8 to 21.6 wt%, respectively in sample Szb36) (Fig. 24). Significant differences between the glass compositions of the two samples can be observed in TiO₂ and P₂O₅ contents as sample Szb36 is poor in both elements (0.20 to 0.26 and 0.00 to 0.03, respectively) whereas glasses of sample Szb59 are the richest in TiO₂ among all samples (1.61 to 2.46 wt%) and have relatively high P₂O₅ contents (0.23 to 1.13 wt%) with the highest amount in the silicate melt inclusion (Table 8).

7.1.6.2. Spinel lherzolites with websterite and clinopyroxene vein(s)

For xenolith Szgk99/11 only silicate melt veins were analyzed from the lherzolitic wall rock whereas from Szb63 glasses of primary and secondary silicate melt inclusions, silicate melt veins and melt pockets could have been analyzed from both the websterite vein and the lherzolitic wall rock. In several cases, the silicate melt veins and inclusions were so thin or small (<10 microns), that the surrounding mineral (either clinopyroxene or olivine) was included in the measurements (shown e.g. by high mg#s of the glasses). In such cases, the corrected compositions (i.e. measured composition – the composition of certain amount of the surrounding phase until reaching mg#-range of the pure silicate glasses of the same samples) are also shown in Table 8 and Fig. 24. The glasses in xenolith Szgk99/11 have a quite restricted compositional range. With the lowest Al₂O₃ (17.1 to 18.2 wt%) and highest P₂O₅ (0.49 and 0.72 wt%) compared to the glasses in other xenoliths.

Table 8. glass compositions, page 1.

Table 8. glass compositions, page 2.

The TiO_2 content of these glasses is also relatively high, varying between 1.46 and 2.03 wt%. Only the glasses in silicate melt accumulations of xenoliths Szb59/2 and Szb55 show higher TiO_2 concentrations. Considering the other components, these glasses show the same variations as those in the other xenoliths, relatively high SiO_2 -contents (56.4 to 60.5 wt%).

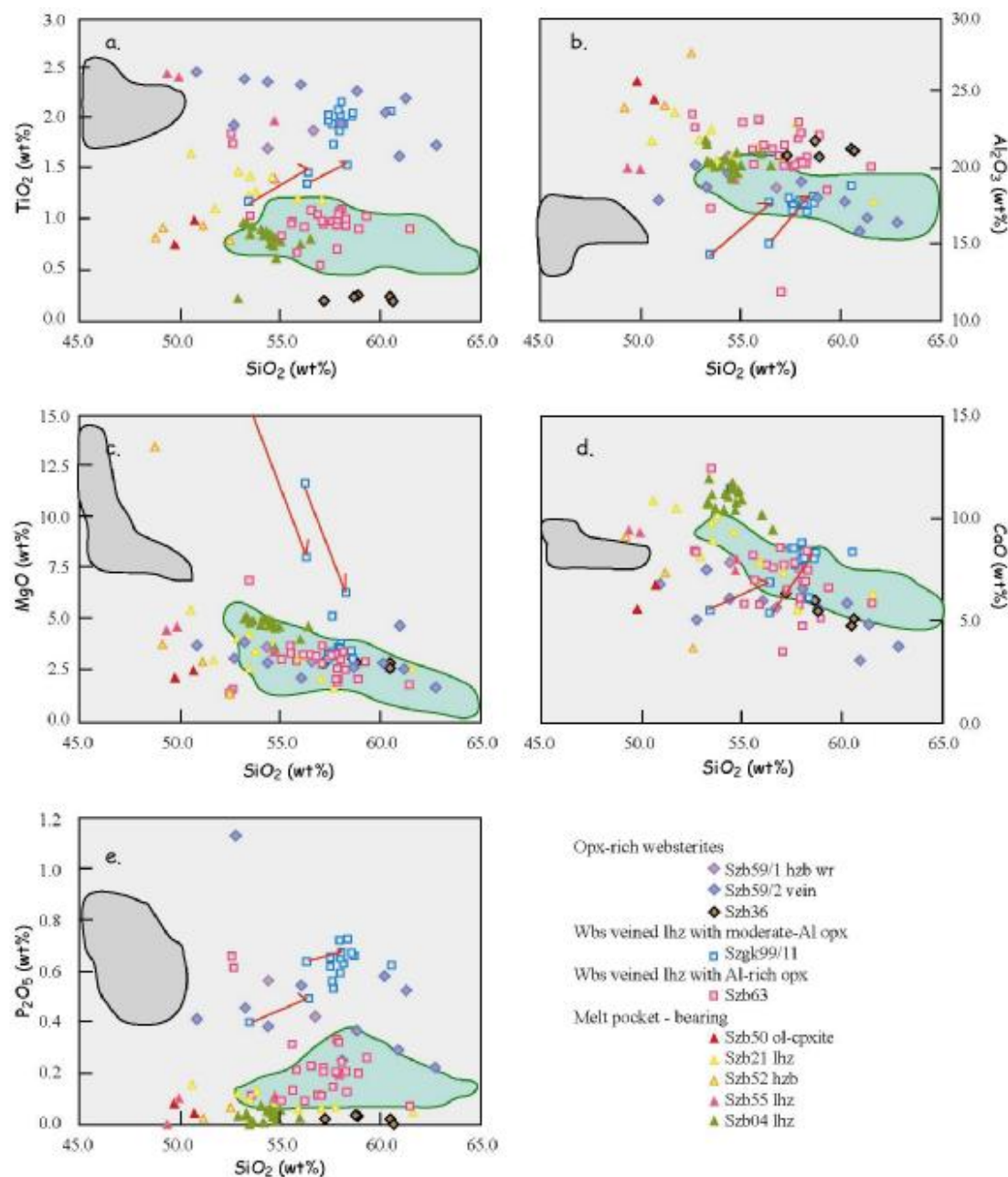


Fig. 24: Compositional variation of silicate glasses in Bakony - Balaton Highland ultramafic xenoliths. Red arrows indicate the change of glass composition after correction (see the text and Table 8). Gray and green fields indicate the compositions of Bakony - Balaton Highland alkaline basalts [23 samples] (Embey-Isztin et al., 1993 and Harangi et al., unpubl.) and Northern Pannonian Basin calc-alkaline andesites [35 samples] (Harangi et al., 2001 and unpubl.) respectively.

The largest dataset on the various types of silicate melt accumulations is available from websterite veined lherzolite Szb63 (Table 8, Fig. 25). Compared to the glass accumulations of other samples, Szb63 glasses usually have intermediate compositions, with restricted ranges of MgO, Al₂O₃, and TiO₂ and more variable CaO and P₂O₅ contents (Fig. 25). No difference can be observed in glass compositions analyzed in the wall rock or in the websteritic vein of the xenolith.

The compositions of the two analyzed secondary silicate melt inclusions found in olivines represent a distinct group, as their SiO₂ and MgO contents are lower and TiO₂ and P₂O₅ contents are higher, compared to the other melt accumulations, and they do not follow the trends shown by the other analyzed glasses (Fig. 24, 25). The other glass accumulations found as primary silicate melt inclusions in spongy rims of clinopyroxenes (Fig 13d), silicate glass veins, silicate glass pocket (do not contain crystalline phase) and silicate melt pocket show decreases in Al₂O₃, FeO, MgO, CaO, with increasing SiO₂ contents. However in case of Al₂O₃ MgO, and CaO contents, the silicate melt inclusions show slight deviations from the previously-mentioned trends. No unequivocal trends were observed in alkalis, as the Na₂O contents show quite large variations whereas the K₂O contents fall in a restricted range (Table 8).

7.1.6.3. *Spinel peridotites and pyroxenites with silicate melt pockets and veins*

7.1.6.3.1. Glasses in carbonate-bearing silicate melt pockets and veins

The glasses of this group show the most wide spread compositions as their SiO₂ varies between 49.4 and 61.6 wt%, their TiO₂ contents are between 0.75 and 2.44 wt% and the Al₂O₃ contents run from 17.82 to 25.66 wt% (Table 8, Fig. 24). All TiO₂, Al₂O₃, MgO and CaO show negative correlation with SiO₂, but the glasses of sample Szb50 fall slightly below the trend line drawn by the compositions of glasses in sample Szb21 and Szb55. All glasses have very low P₂O₅ contents (up to 0.16 wt%).

7.1.6.3.2. Glasses in carbonate-free silicate melt pockets and veins

Glass compositions in lherzolite Szb04 and harzburgite Szb52 are slightly different from the carbonate-bearing glass accumulations and they differ from each other (Table 8, Fig. 24). These glasses have lower TiO₂ (0.63 to 0.96 wt%) and higher P₂O₅ (up to 0.07 wt%) contents compared to the carbonate-bearing ones. Furthermore glasses in sample Szb04 have the highest CaO content among all glasses (9.43 to 11.9 wt%) and their compositions are situated

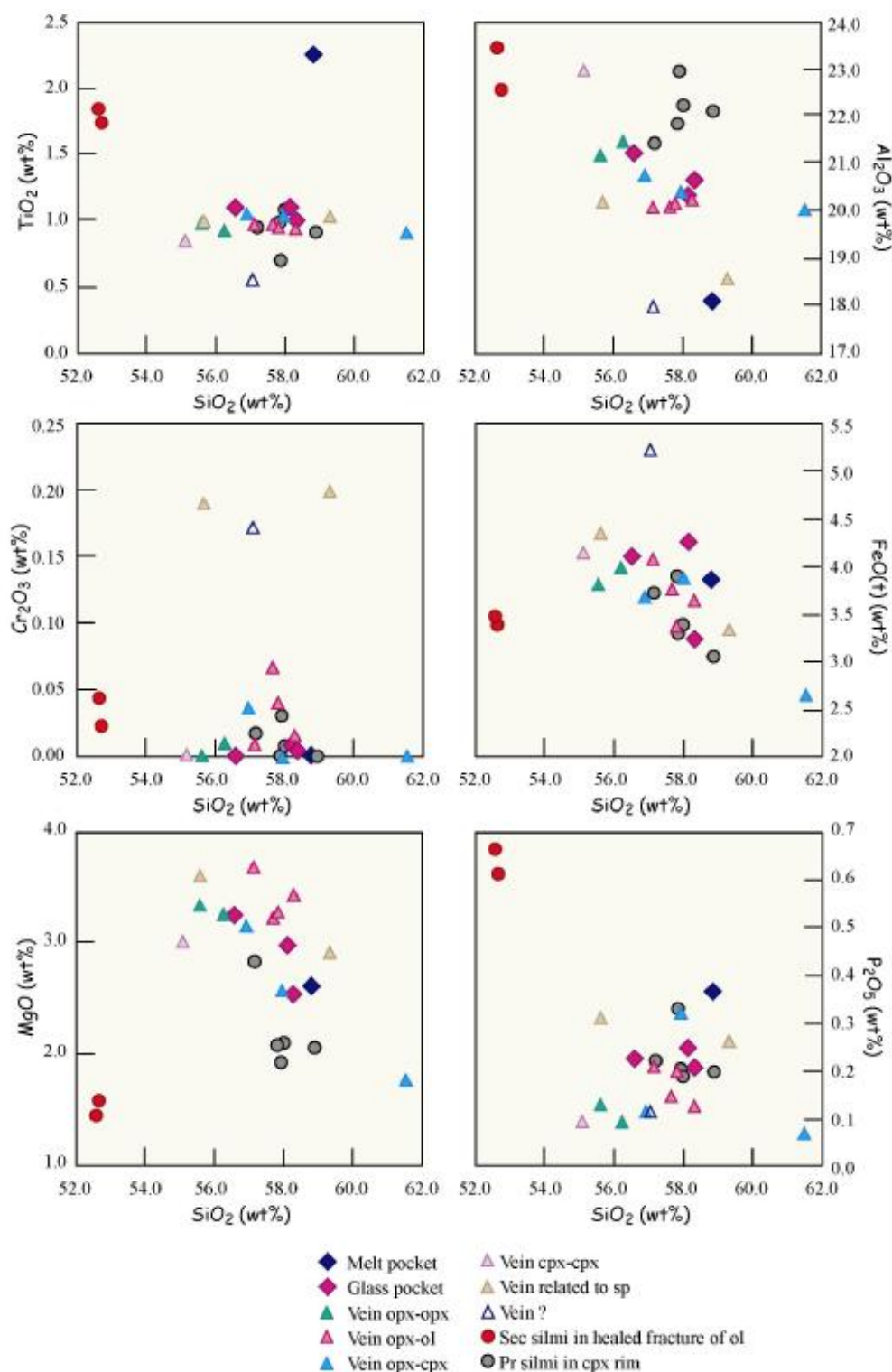


Fig. 25: Compositional variation of different silicate melt accumulations in websterite veined lherzolite, Szb63. Note that only the secondary silicate melt inclusions deviate from the compositional field drawn by the other glass compositions.

above the trend line of MgO-SiO₂, determined by the compositions of glasses in carbonate-bearing samples (Fig. 24). Glasses in sample Szb52 have lower CaO and MgO contents either.

7.1.7. Carbonates

Carbonates in carbonate-bearing silicate melt pockets are Mg-calcites with low FeO (up to 0.54 wt%), MgO (1.15-3.65 wt%), MnO (up to 1.51 wt%), and SrO (up to 0.12 wt%) contents (Bali et al., 2002).

7. 2. Trace elements

7.2.1. Clinopyroxenes

The rare earth element (REE) and trace element compositions of clinopyroxenes have a very large compositional range (Fig. 26 to 34) from light rare earth (LREE) depleted and middle

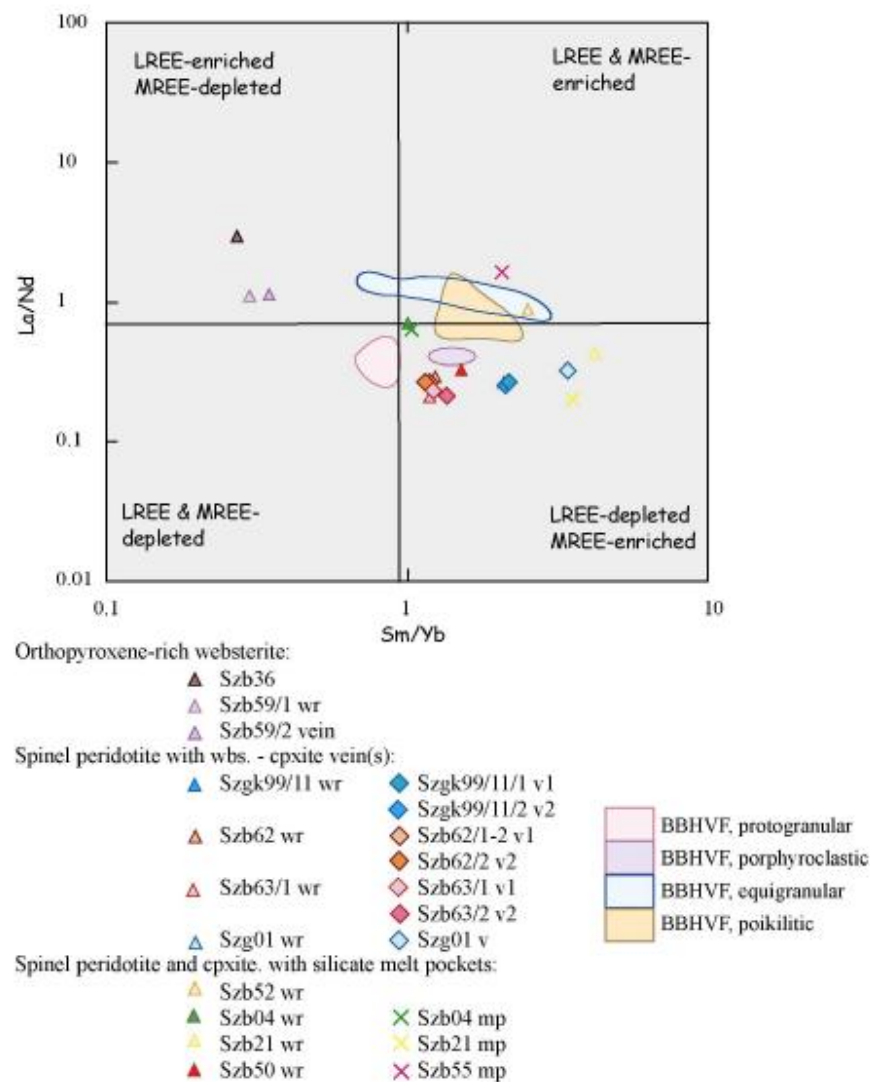


Fig. 26: Rare Earth Element distribution in clinopyroxenes of BBHVF ultramafic xenoliths in Sm/Yb vs La/Nd diagram. For comparison the compositional fields of clinopyroxenes from ultramafic xenoliths with different textures from the BBHVF reported by Downes et al. (1992) are also shown for comparison.

rare earths (MREE) enriched showing n-shaped patterns in chondrite normalized diagrams (normalizing values from Anders & Grevesse, 1989), but several xenoliths have clinopyroxenes with LREE-enrichment and MREE-depletion (u-shaped patterns) or enrichment in both LREE and MREE (Fig. 26 to 34). No LREE and MREE depleted

clinopyroxenes were found.

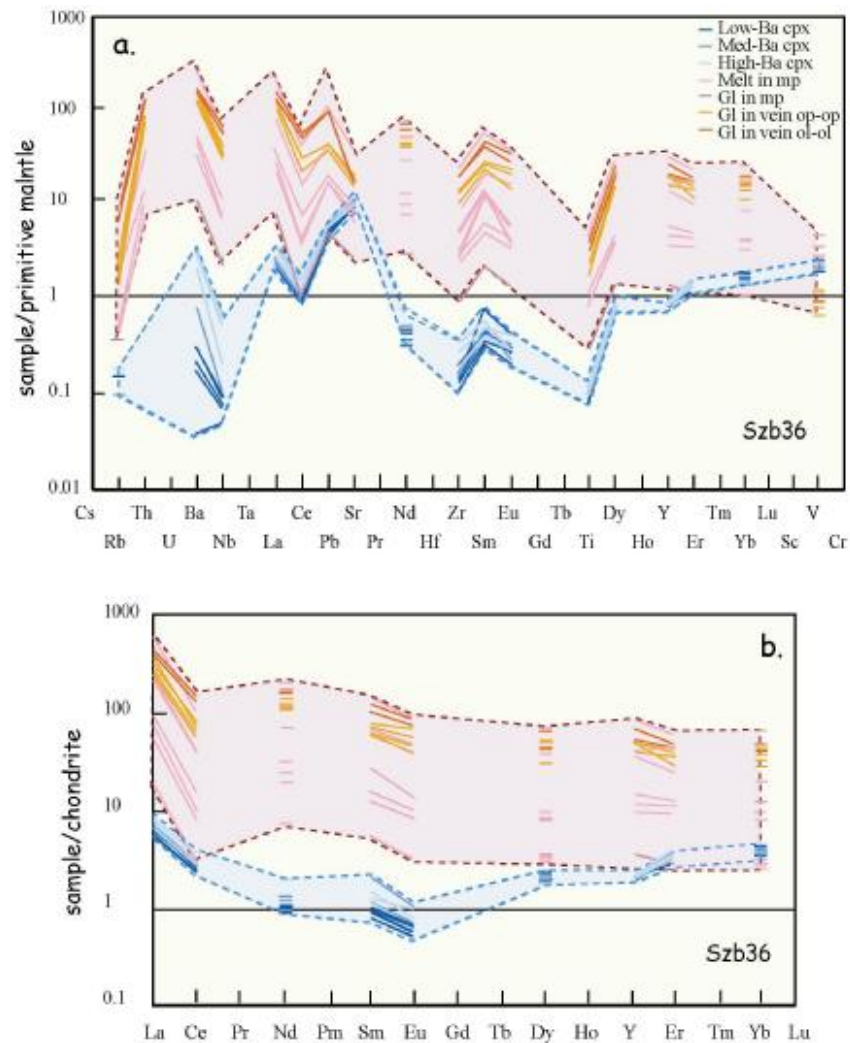


Fig. 27: Primitive mantle normalized multi element (a) and chondrite normalized rare earth element (b) diagrams for clinopyroxenes, melt accumulations of orthopyroxene-rich websterite, Sz36. Low-Ba, Med-Ba, High-Ba cpx - mantle clinopyroxene with relatively low, medium and high Ba contents, melt in mp - bulk melt in silicate melt pockets, Gl in vein op-op - silicate glass in silicate melt vein running between orthopyroxenes, Gl in vein ol-ol - silicate glass in silicate melt vein running between primary olivines. Normalizing values - Anders & Grevesse (1989) for chondrite, McDonough & Sun (1995) for primitive mantle.

The compositional range of clinopyroxenes is much larger than those in the BBHVF ultramafic xenoliths studied by Downes et al. (1992) (Fig. 26).

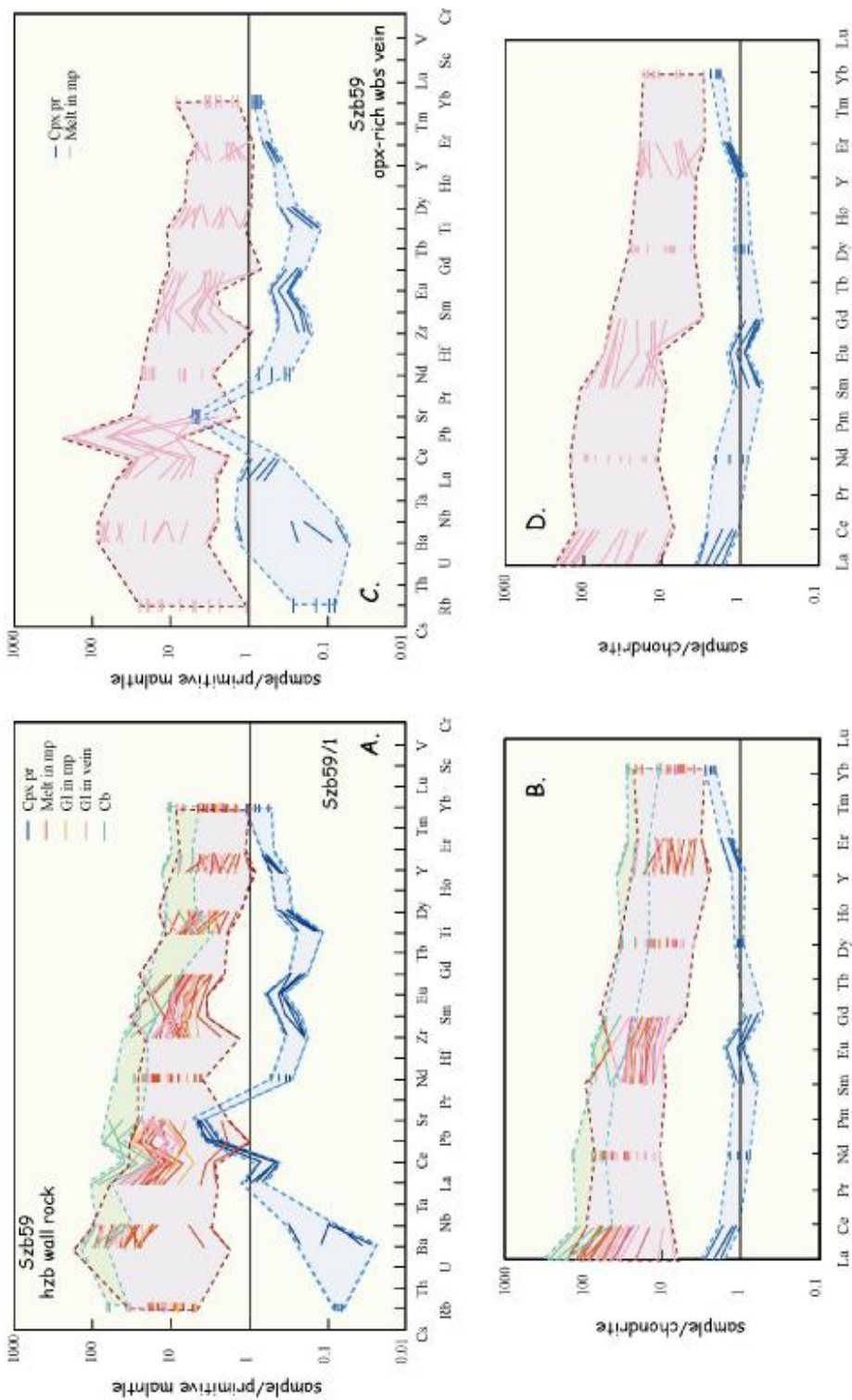


Fig. 28: Primitive mantle normalized multi element and chondrite normalized rare earth element diagrams for clinopyroxenes, melt accumulations and melt pocket carbonates of harzburgite/opx-rich websterite composite xenolith, Szab59. Cpx pr - mantle clinopyroxene, melt in mp - bulk melt in silicate melt pockets, Gl in mp - silicate glass in silicate melt pocket, Gl in vein - silicate glass in silicate melt vein, Cb in mp - carbonate in silicate melt pocket. Normalizing values - Anders & Grevesse (1989) for chondrite, McDonough & Sun (1995) for primitive mantle.

7.2.1.1. Orthopyroxene-rich websterites

The clinopyroxenes of orthopyroxene-rich websterites and of harzburgitic wall rock Szb59/1 have LREE-enriched and MREE-depleted (u-shaped) chondrite normalized rare earth element patterns. Within individual samples the clinopyroxene compositions have a restricted range (Fig. 27, 28).

The strongest LREE-enrichment relative to MREEs is shown by clinopyroxenes of Szb36 (Table 9, Fig. 27). The heavy rare earth elements (HREE) also show enrichment compared to the middle rare earths with $Sm_N/Yb_N < 1$ and the LREEs are usually enriched compared to the heavy rare earths with La_N/Yb_N above 1 (Table 10, 11).

Considering other trace elements, the Nb depletion in clinopyroxenes of Szb36 xenolith is evident from the high Ba_N/Nb_N (usually above 1) and low Nb_N/La_N ratios, and this negative anomaly is observed in the primitive mantle normalized trace element diagram (Fig. 26). Clinopyroxenes neither in the orthopyroxene-rich websterite part nor its harzburgite wall rock have a negative Nb anomaly, (Table 10, 11, Fig. 27). Enrichment in Pb and Sr and depletion in Zr and Ti is observed in most clinopyroxenes (Fig. 26, 27).

7.2.1.2. Spinel lherzolites with websterite and clinopyroxenite vein(s)

Clinopyroxenes of this group have LREE-depleted MREE-enriched (n-shaped) chondrite normalized rare earth element patterns. No differences between clinopyroxenes of websterite/clinopyroxenite vein and lherzolite wall rock were observed in any of the xenoliths (Fig. 29, 30, 31). The clinopyroxenes have very uniform compositions within individual samples.

7.2.1.2.1. Websterite veined lherzolite with moderate Al-orthopyroxenes

Clinopyroxenes of Szgk99/11 have very uniform compositions (Fig. 29). Clinopyroxenes are depleted in light rare earth elements compared to the middle rare earths (with $La_N/Sm_N < 1$) and are enriched in MREE compared to the HREE. The La_N/Yb_N values are always above 1 (Table 12, 13) showing LREE enrichment compared to the HREEs.

Considering other trace elements the clinopyroxenes show negative peaks of Zr and Ti compared to the neighboring elements.

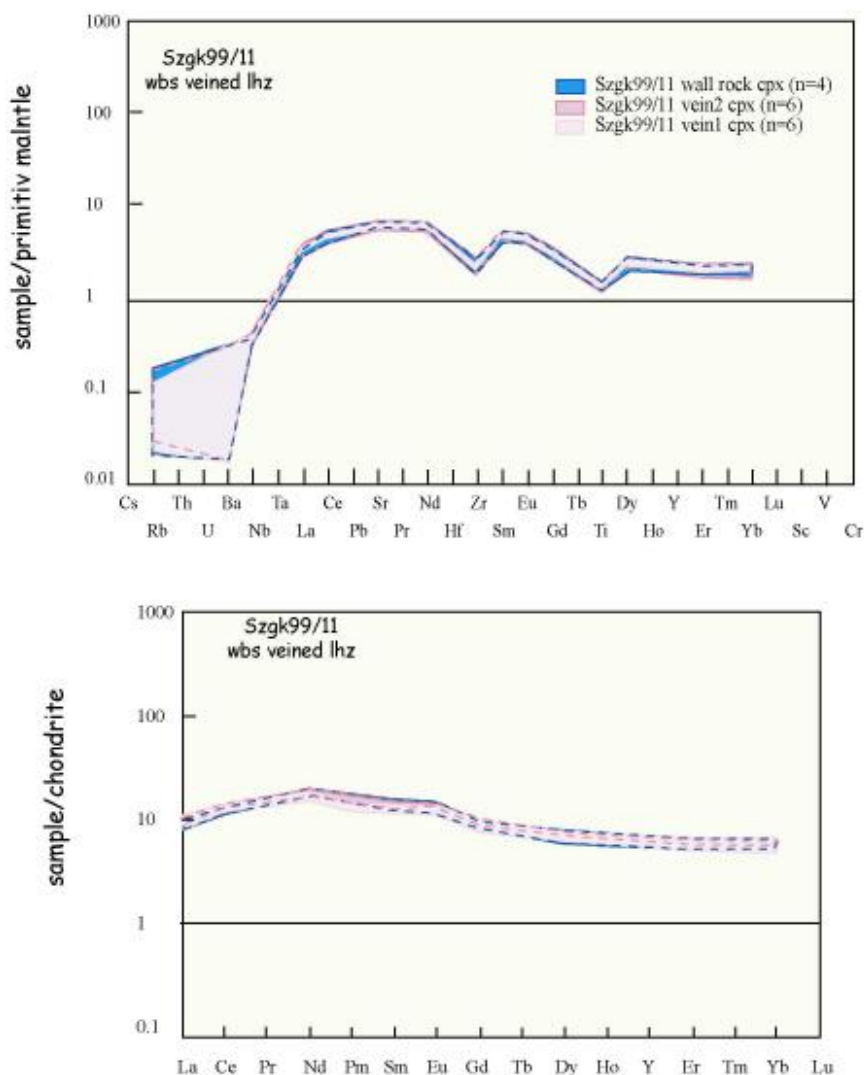


Fig. 29: Primitive mantle normalized multi element and chondrite normalized rare earth element diagrams for clinopyroxenes of websterite veined lherzolite, Szgk99/11 containing moderate-Al orthopyroxenes. n - number of analyzed clinopyroxenes which build up the compositional fields. Normalizing values - Anders & Grevesse (1989) for chondrite, McDonough & Sun (1995) for primitive mantle.

7.2.1.2.2. Websterite and clinopyroxenite veined lherzolite with Al-rich orthopyroxenes
Clinopyroxenes of samples Szb62, Szb63 and Szg01 also show MREE enrichment compared to both LREE and HREE (Table 14, 15, 16, Fig. 30, 31). In xenoliths Szb62 and Szb63 the LREEs are depleted compared to the HREEs (with $La_N/Yb_N < 1$) (Table 14, 15).

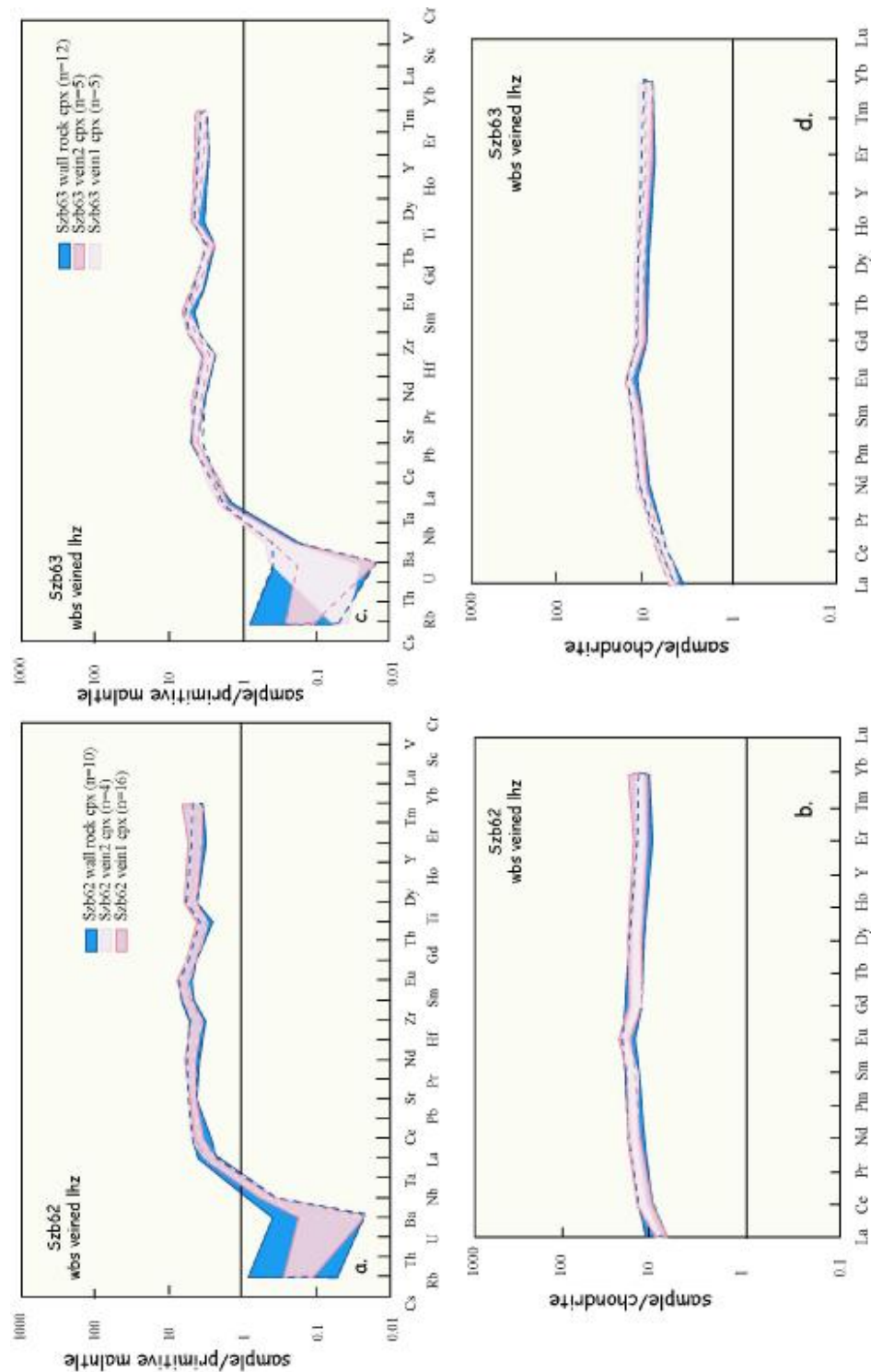


Fig. 30: Primitive mantle normalized multi element and chondrite normalized rare earth element diagrams for clinopyroxenes of websterite veined lherzolites containing Al-rich orthopyroxenes (samples Szb62 and Szb63). n - number of analyzed clinopyroxenes which build up the compositional fields. Normalizing values - Anders & Grevesse (1989) for chondrite, McDonough & Sun (1995) for primitive mantle.

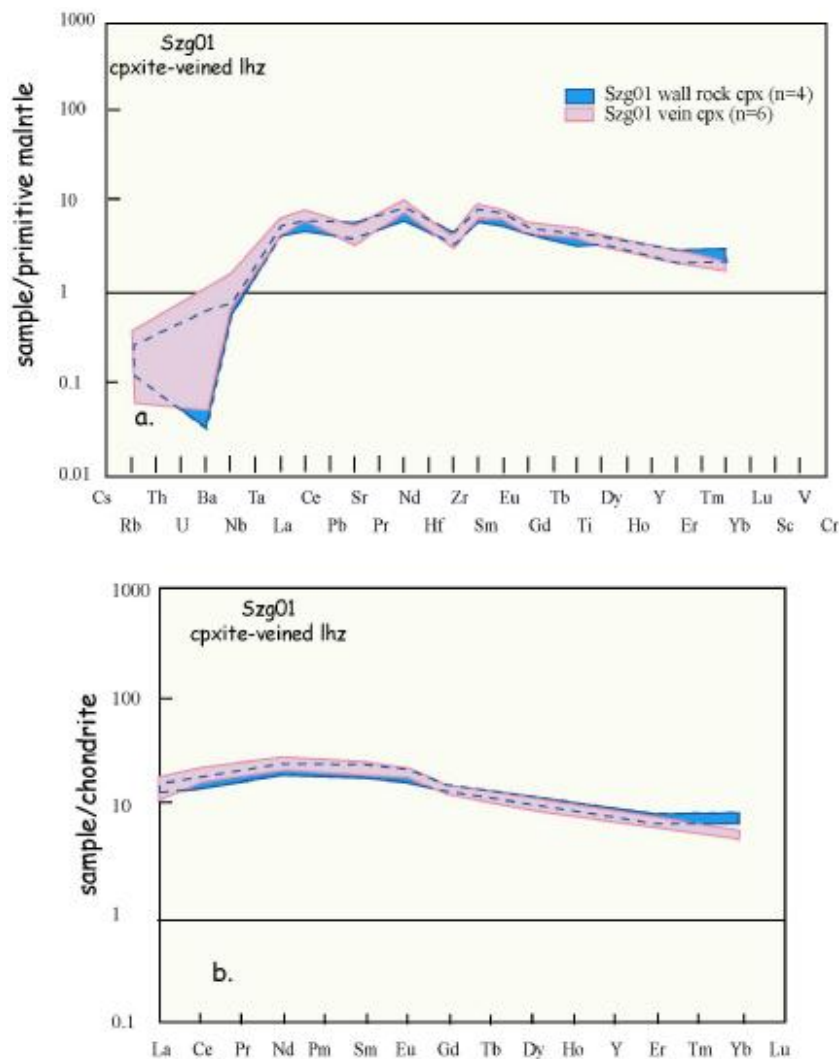


Fig. 31: Primitive mantle normalized multi element and chondrite normalized rare earth element diagrams for clinopyroxenes of clinopyroxenite veined lherzolite, Szg01 containing Al-rich orthopyroxenes. n - number of analyzed clinopyroxenes which build up the compositional fields. Normalizing values - Anders & Grevesse (1989) for chondrite, McDonough & Sun (1995) for primitive mantle.

Clinopyroxenes in these two samples have higher HREE-contents compared to those in sample Szg01, in which the clinopyroxenes are enriched in both LREE and MREE compared to HREE (Fig. 30).

Clinopyroxenes in all xenoliths have quite a large compositional range in Ba (Fig. 30, 31). Ba_N/Nb_N ratios are usually below 1. Small negative peaks of Zr are found in all samples whereas the negative Ti anomaly is absent in sample Szg01 (and clinopyroxenes in the

clinopyroxenite vein of this xenolith have slight positive peak).

7.2.1.3. Silicate melt pocket – bearing xenoliths

7.2.1.3.1 Mantle clinopyroxenes in silicate melt pocket – bearing xenoliths

Mantle clinopyroxenes of silicate melt pocket – bearing samples show the most wide spread compositions with LREE-depleted – MREE-enriched (samples Szb21, Szb50) or LREE- and MREE-enriched (Szb52) or flat (Szb04) chondrite normalized rare earth element patterns (Fig. 32, 33, 34). Again, the clinopyroxenes of individual samples have uniform compositions (Table 19 to 23, Fig. 32, 33, 34).

Among the xenoliths having clinopyroxenes with n-shaped REE patterns, lherzolite Szb21 shows less depleted LREE compared to MREEs (Fig. 32) with La_N/Sm_N nearly 1 and the MREEs are strongly enriched compared to HREEs, whereas clinopyroxenes in olivine-clinopyroxenite Szb50 has stronger LREE-depletion and less significant MREE-enrichment. Furthermore, in clinopyroxenes of lherzolite Szb21 the LREEs are always enriched compared to HREEs whereas no, or slight LREE enrichment can be found in the clinopyroxenes of olivine clinopyroxenite, Szb50. Considering other trace elements clinopyroxenes of both samples have quite variable Ba contents (Table 19, 20). In case of sample Szb21 Ba_N/Nb_N ratios vary between 0.06 (Nb-enriched) to 1.08 (Ba-enriched) whereas this variation is more significant in sample Szb50 (from 0.16 to 29.28) with the highest values observed in the rim of cpx9. Sr, Zr and Ti have negative peaks compared to the neighboring elements in primitive mantle normalized trace element diagrams (Fig. 32).

Mantle clinopyroxenes of lherzolite Szb04 and harzburgite Szb52 are LREE-enriched, but to different degrees. Clinopyroxenes in lherzolite Szb04 have nearly flat REE-patterns, whereas the clinopyroxenes in harzburgite Szb52 show strong LREE and MREE enrichment compared to the HREEs. In case of other trace elements the Ba-contents are also variable in these xenoliths usually with enrichment compared to Nb. Furthermore in lherzolite Szb04 small positive peak of Pb, and negative peaks of Zr and Ti can be observed in trace element diagrams whereas in harzburgite Szb52 only the negative anomalies of Zr and Ti are present (Fig. 34).

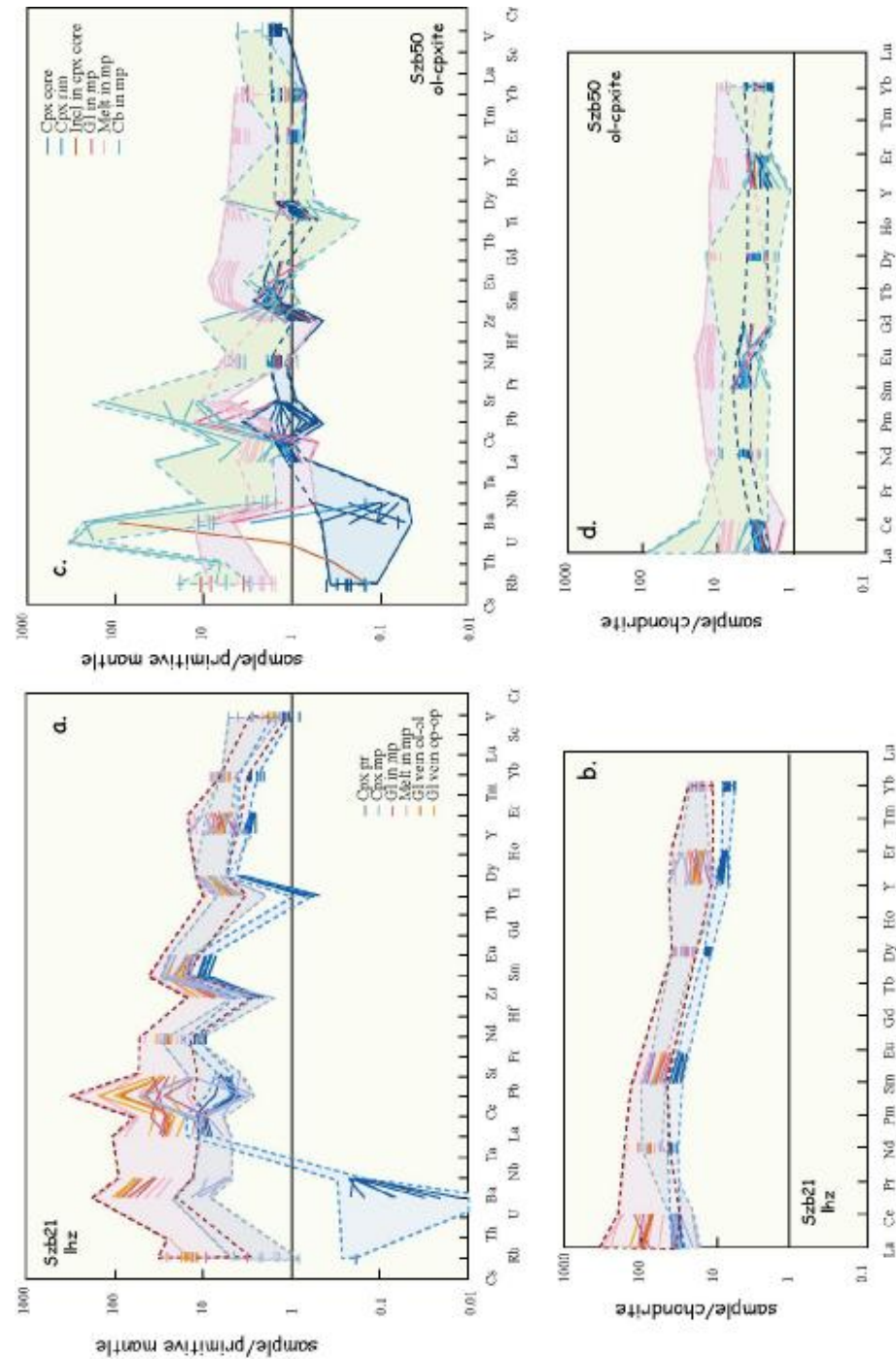


Fig. 32: Primitive mantle normalized multi element and chondrite normalized rare earth element diagrams for clinopyroxenes, melt accumulations and carbonates of samples Sz621 and Sz650. Cpx pr - primary mantle clinopyroxene, cpx mp - newly formed clinopyroxenes in silicate melt pockets, melt in mp - bulk melt in silicate melt pockets, Gl in mp - silicate glass in silicate melt pocket, gl vein - silicate glass in silicate melt vein (among primary mantle olivines - ol-ol or primary mantle orthopyroxenes - op-op), cb - carbonate in silicate melt pocket. Normalizing values - Anders & Grevesse (1989) for chondrite, McDonough & Sun (1995) for primitive mantle.

7.2.1.4.2. Melt pocket clinopyroxenes in silicate melt pocket – bearing samples

In lherzolites Szb04 (with carbonate-free melt pockets), Szb21 (with carbonate-bearing melt pockets) and Szb55 (with carbonate-bearing melt pockets), the newly formed clinopyroxenes in silicate melt pockets were large enough to analyze. They usually show slightly different REE-patterns and wider compositional range compared to the coexisting mantle clinopyroxenes (Fig. 32, 34).

Newly formed melt pocket clinopyroxenes in lherzolite Szb21 also have n-shaped REE-patterns but they are more depleted in LREEs and more enriched in MREEs compared to the primary clinopyroxenes (Fig. 32). Melt pocket clinopyroxenes of lherzolite Szb04 also show enrichment in MREE and HREE compared to those in the mantle clinopyroxenes (Fig. 34), but their LREE show great variability. Melt pocket clinopyroxenes in lherzolite Szb55 have smooth REE pattern with slight depletion in LREE compared to MREE. The overall REE content of Szb55 melt pocket clinopyroxenes is higher than those were observed in Szb04 and Szb21 melt pocket clinopyroxenes.

Considering other trace elements the melt pocket clinopyroxenes of all samples are enriched in Ba compared to Nb. Furthermore melt pocket clinopyroxenes are richer in Rb compared to the coexisting mantle ones (Fig. 32, 34). In sample Szb04 melt pocket clinopyroxenes show high positive peak of Pb in primitive mantle normalized trace element diagrams whereas this peak usually absents in melt pocket clinopyroxenes of sample Szb21.

7.2.2. Amphiboles

The trace element content of Szb52 and Szb55 amphiboles were analyzed. Amphiboles in sample Szb52 and Szb55 always show strong LREE- and MREE-enrichment relative to HREEs with slight variation in the individual xenoliths (Fig. 33, 34, Table 18, 20). REE pattern of amphiboles in Szb52 harzburgite run sub-parallel to the pattern of the coexisting mantle clinopyroxenes, but with higher REE contents. Considering other trace elements (Fig. 33, 34) amphiboles have positive Nb and Ti anomalies and negative Zr peaks relative to the neighbor elements, furthermore in amphiboles of Szb52 slight negative Pb-anomaly is also present (Fig. 33, 34).

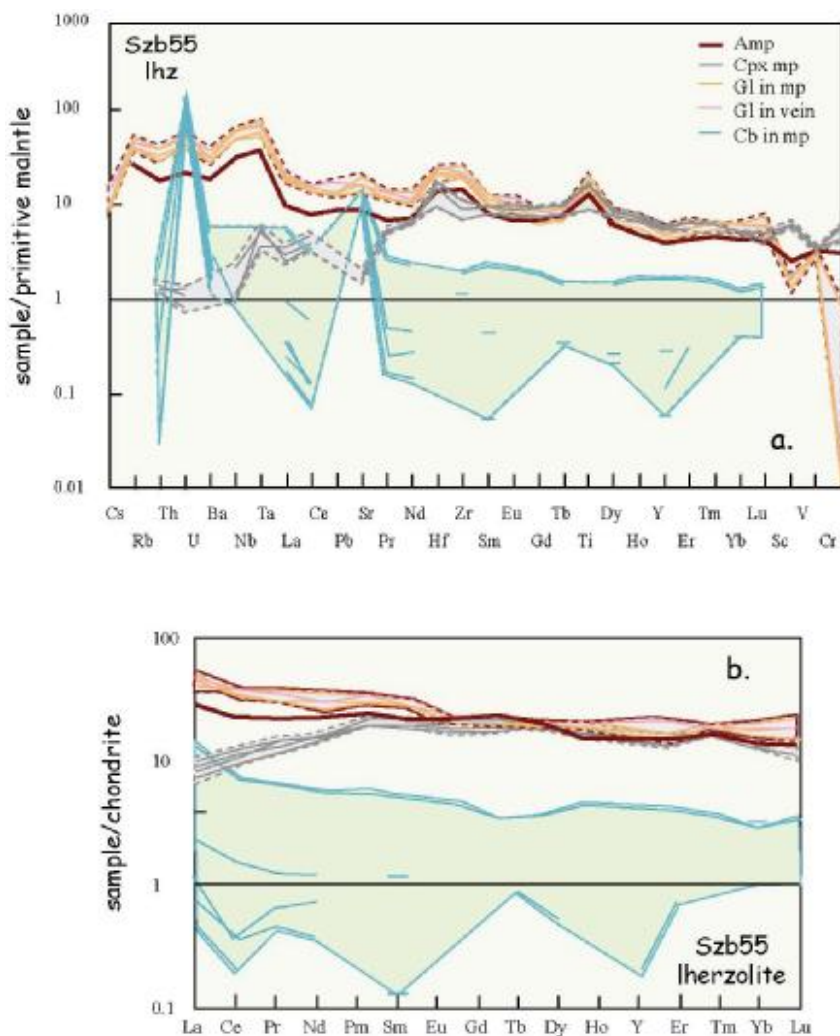


Fig. 33: Primitive mantle normalized multi element and chondrite normalized rare earth element diagrams for mantle amphiboles, melt pocket clinopyroxenes, melt pocket carbonates, silicate glass in melt pockets, in lherzolite, Sz55. Amp - mantle amphibole, cpx mp - newly formed clinopyroxenes in silicate melt pockets, Gl in mp - silicate glass in silicate melt pocket, Gl vein - silicate glass in silicate melt vein, Cb in mp - carbonate in silicate melt pocket. Normalizing values - Anders & Grevesse (1989) for chondrite, McDonough & Sun (1995) for primitive mantle.

7.2.3. Silicate melt accumulations

The compositions of silicate melt pockets and veins in xenoliths Sz504, Sz521, Sz536, Sz550, Sz552, Sz555 and Sz559 were determined. In the other samples the silicate melt veins or inclusions were either too thin or small to analyze (i.e. it was enough for microprobe analyses, but not for laser ablation which uses a much larger beam size). In most cases the melt pocket phases were too small to be analyzed by the laser beam, and instead the bulk melt of the pockets was ablated (for standardization see the chapter of analytical techniques). The measurement style (i.e. bulk melt or silicate glass) is indicated in all figures and tables.

7.2.3.1. Carbonate-bearing silicate melt accumulations

In xenoliths Szb21, Szb55 and Szb59/1 silicate glass in glass veins and in melt pockets as well as the bulk melt were also analyzed. In xenoliths Szb50 and Szb59/2 only the analysis of bulk melt was possible.

The bulk silicate melts in all samples always have higher REE-contents than the coexisting mantle clinopyroxenes and or amphiboles (Table 10, 11, 16, 17, 18, 19, 20, Fig. 27, 28, 32, 33, 34). They usually have LREE- and MREE-enrichment compared to the HREE (Fig. 27, 28, 31, 32, 34). The only exception is the melt of olivine clinopyroxenite Szb50 which is enriched in MREE relative to HREE, but have lower LREE compared to both MREEs and HREEs (Table 20, Fig. 32).

Considering other trace elements the bulk silicate melt of sample Szb50 show a narrow range having negative Nb- and Zr-peaks, but no positive Pb-anomaly was observed. In xenoliths Szb59 and Szb21 the bulk silicate melts show a much more significant overall enrichment in incompatible elements than that was observed in sample Szb50 (Fig. 27, 31). Different extents of positive Pb-anomalies are present in melts of both xenoliths, but in case of Szb59 the negative Zr- and Ti-peaks are absent.

The patterns of silicate glasses analysed in melt pockets or melt veins run parallel to those of the bulk melts (Fig. 27, 28, 31). Their compositional ranges are much narrower than the bulk melts in the same samples. In lherzolite Szb21 the bulk melts in several cases show stronger trace element enrichment than the silicate glass analysed either in melt pockets or in melt veins, whereas in sample Szb59 the glasses of silicate melt veins and melt pockets have elevated REE contents and the stronger enrichment in LREEs than that was observed in the bulk melt.

Silicate glasses analysed in melt pockets and veins of sample Szb55 follow the pattern of the coexisting amphiboles, but the glasses show overall higher trace element content (Table 21, Fig. 33).

7.2.3.2. Carbonate-free silicate melt accumulations

In lherzolite Szb04 silicate glass both in melt veins and melt pockets and bulk melt in melt pocket were analyzed, in orthopyroxene-rich websterite Szb36 glass was analyzed only in silicate melt veins in melt pockets only bulk melt composition was measured, and in sample

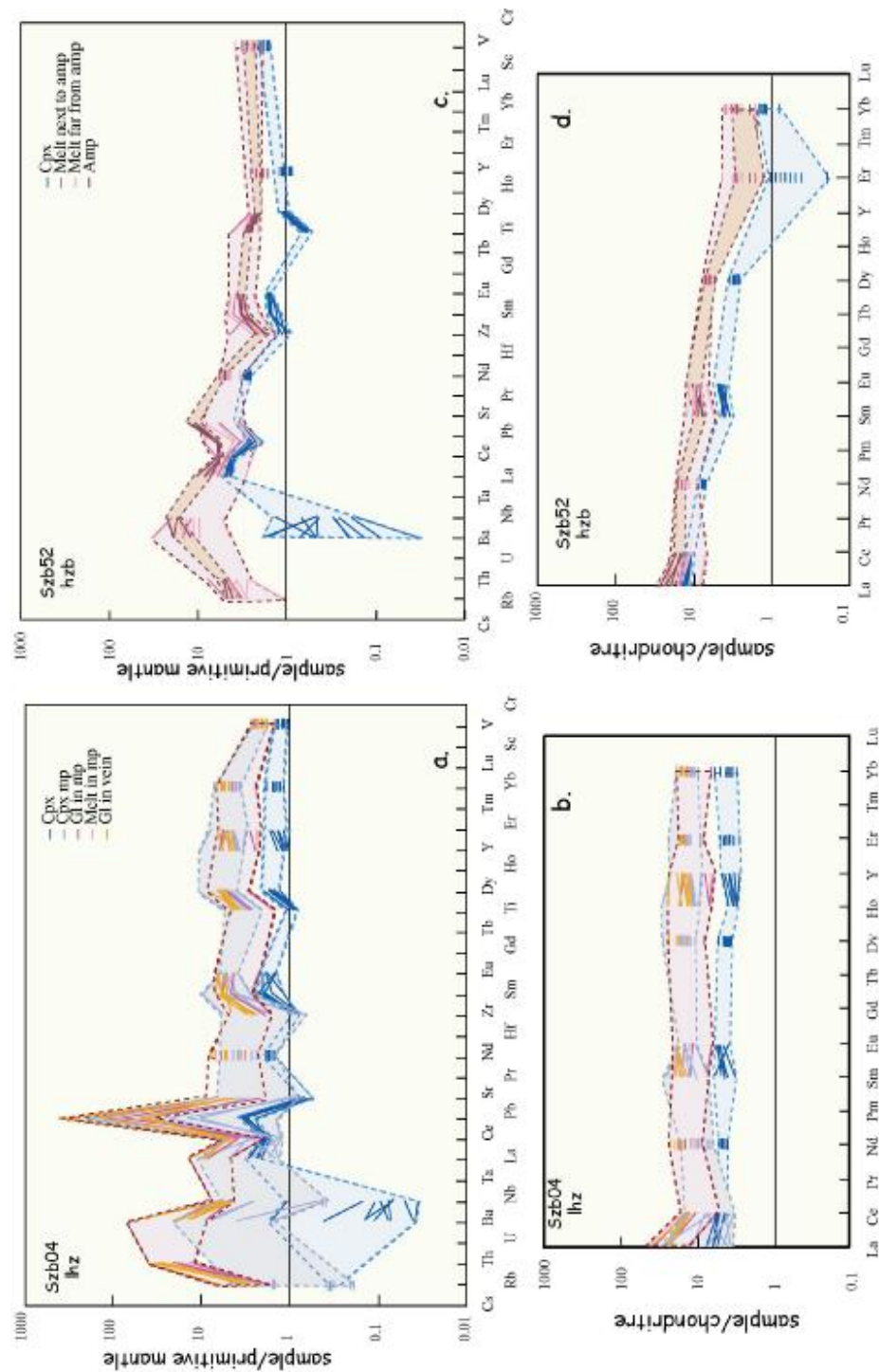


Fig. 34: Primitive mantle normalized multi element and chondrite normalized rare earth element diagrams for clinopyroxenes, amphiboles, melt accumulations of ilmenite Szb04 and harzburgite Szb52. Cpx - mantle clinopyroxene, Amp - mantle amphiboles, cpx mp - newly formed clinopyroxenes in silicate melt pockets, Melt in mp - bulk melt in silicate melt pockets, Gl in mp - silicate glass in silicate melt pocket, Gl vein - silicate glass in silicate melt vein. Normalizing values - Anders & Grevesse (1989) for chondrite, McDonough & Sun (1995) for primitive mantle.

Szb52 only the bulk melt pocket was analyzable.

All melt accumulations in all the three samples have LREE enriched REE-patterns. In sample Szb52 the composition of the silicate melt follows the composition of the coexisting mantle amphiboles and clinopyroxenes falling usually between the patterns of them or in the range of amphiboles. In the other two samples the bulk melts are usually 2 to 10 times more enriched compared to the coexisting mantle clinopyroxenes (Table 23, Fig. 34). The patterns of silicate glasses in either melt pockets or in melt veins run sub-parallel to the patterns of bulk melt but with an overall higher trace element content. Both in sample Szb04 and Szb36 the compositions of glasses in silicate melt veins have the highest REE-contents compared to those in the glasses of melt pockets or in bulk melts (Fig. 27, 34).

Considering other trace elements the patterns of bulk melts in melt pockets of Szb52 harzburgite follow again the pattern of the coexisting mantle amphiboles. The compositions of glasses and bulk melts of sample Szb36 run parallel to sub-parallel with the primitive mantle normalized trace element pattern of the coexisting primary clinopyroxenes showing up to 100 times enrichment. The glasses either in melt pockets or in melt veins and bulk melts of lherzolite Szb04 usually have lower extents of trace element enrichment compared to the primary clinopyroxenes than that was observed in Szb36 orthopyroxene-rich websterite, but have much higher positive Ba- and Pb-peaks than was observed in any of the previously described xenoliths (Fig. 27, 34).

7.2.4. Carbonates

Large carbonate aggregates were analyzed in melt pockets of Szb50, Szb55 and Szb59/1 xenoliths. All samples have carbonates with very variable compositions (Table 10, 17, 18, Fig. 27, 32, 33) but the carbonates of sample Szb55 show the largest variations. All the carbonates are enriched in incompatible trace elements, with high positive peaks of Ba, La, Pb and Zr. U was measured in only two carbonates of two melt pockets of Szb50 olivine clinopyroxenite and Th was above detection limit only in one of them. For this aggregate, U is about 50 times more enriched than Th (Table 20).

Table 9. Szb36

Table 10 Sz59/1

Table 11 Szb59/2

Table 12 Szgk99/11

Table 13 Sz62

Table 14 Sz63

Table 15 szg01

table16 Szb21

table 17 Szb50

table 18 Szb55

table 19 szb04

table 20 Szb52

7.3. Sr - Pb isotopes

Sr-Pb isotope compositions of separated clinopyroxenes and melt pockets are listed in Table 21. Clinopyroxenes were separated from all the main rock types (i.e. orthopyroxene-rich websterites, websterite veined peridotites and xenoliths with silicate melt pockets). For the websterite veined lherzolites, only the two xenoliths containing Al-rich orthopyroxenes were analyzed, and in these samples it was possible to separate clinopyroxene from both the wall rock and the veins.

7.3.1. Sr-isotopes

$^{87}\text{Sr}/^{86}\text{Sr}$ for the clinopyroxenes ranges from 0.70313 (lherzolite wall rock of Szb63) to 0.70747 (in the melt pocket bearing lherzolite Szb21) which is a much larger range was observed by Downes et al. (1992) for the BBHVF ultramafic xenoliths (between 0.70307 and 0.70523).

The websterite veined lherzolites (Szb62 and Szb63) have the lowest $^{87}\text{Sr}/^{86}\text{Sr}$ between 0.70313 and 0.70325. No unequivocal difference is observed between the wall rock and vein clinopyroxenes, although the later ones tend to have somewhat higher $^{87}\text{Sr}/^{86}\text{Sr}$ values (Table 21). Both wall rock and vein clinopyroxenes in xenolith Szb01 have higher $^{87}\text{Sr}/^{86}\text{Sr}$ ratios compared to the previously mentioned xenoliths with clearly higher values in the vein clinopyroxenes (0.70386 and 0.70436, respectively) (Fig. 35).

| Rock type | Xenolith | $^{87}\text{Sr}/^{86}\text{Sr}$ | error on the last digit | 206Pb/204Pb | 207Pb/204Pb | 208Pb/204Pb |
|---|--------------------------|---------------------------------|-------------------------|-------------|-------------|-------------|
| opx-rich websterites | Szb59/1 hzb wr cpx | 0.70568 | +/-2 | 18.61 | 15.65 | 38.84 |
| | Szb59/2 opx-rich wbs cpx | 0.70591 | +/-1 | 18.74 | 15.66 | 38.83 |
| | Szb59/2 opx-rich wbs mp | 0.70589 | +/-2 | 18.74 | 15.66 | 38.80 |
| lherzolites with websterite and clinopyroxenite veins | Szb62 wbs vein cpx | 0.70325 | +/-1 | 18.04 | 15.48 | 37.88 |
| | Szb62 lhz wr cpx | 0.70322 | +/-1 | 18.06 | 15.45 | 37.73 |
| | Szb63 wbs vein cpx | 0.70315 | +/-1 | 18.47 | 15.50 | 38.03 |
| | Szb63 lhz wr cpx | 0.70313 | +/-1 | 18.58 | 15.55 | 38.21 |
| | Szg01 cpxite vein cpx | 0.70436 | +/-2 | 18.52 | 15.62 | 38.42 |
| | Szg01 lhz wr cpx | 0.70386 | +/-2 | 18.45 | 15.57 | 38.51 |
| peridotites and clinopyroxenites with silicate melt pockets | Szb21 lhz cpx | 0.70747 | +/-1 | 18.71 | 15.65 | 38.88 |
| | Szb50 ol-cpxite cpx | 0.70538 | +/-1 | 18.85 | 15.64 | 38.79 |
| | Szb55 lhz mp | 0.70394 | +/-1 | 19.06 | 15.67 | 38.99 |
| | Szb04 lhz cpx | 0.70462 | +/-1 | 18.61 | 15.66 | 38.76 |
| | Szb52 hzb mp | 0.70500 | +/-1 | 18.69 | 15.65 | 38.83 |

Table 21: Sr - Pb isotopic composition of separated clinopyroxenes (cpx) and silicate melt pockets (mp).

Vein cpx - clinopyroxenes from websteritic or clinopyroxenitic veins, wr cpx - clinopyroxenes from the wall rock of veined samples.

Orthopyroxene-rich websterites contained only minor clinopyroxene, but for composite xenolith Szb59 clinopyroxenes were separated from both the orthopyroxene-rich (Szb59/2) and harzburgite (Szb59/1) part of the xenolith. They show very high $^{87}\text{Sr}/^{86}\text{Sr}$ between 0.70568 and 0.70591 with the higher ratios in the orthopyroxene-rich websterite part.

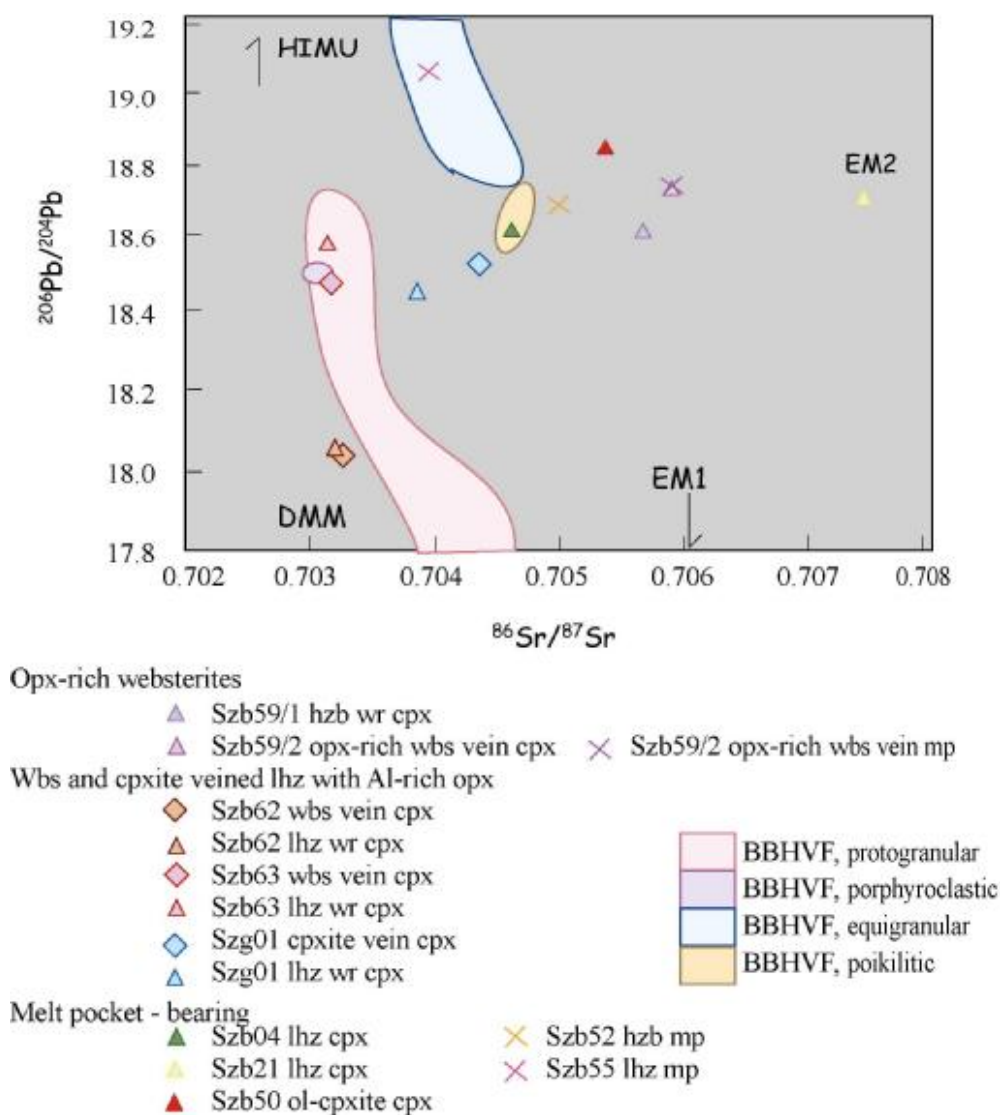


Fig. 35: Sr - Pb - isotopic compositions of separated clinopyroxenes (cpx) and silicate melt pockets (mp). The composition fields of clinopyroxenes from ultramafic xenoliths with different textures from the BBHVF reported by Downes et al. (1992) and Rosebaum et al. (1997) are also shown for comparison. Mantle components (DMM - depleted MORB mantle, HIMU - high μ , EM1 - enriched mantle 1, EM2 - enriched mantle 2) are from Hart (1984).

Clinopyroxenes in melt pocket bearing samples have the $^{87}\text{Sr}/^{86}\text{Sr}$ values varying between 0.70462 and 0.70747.

Separated melt pockets (Szb52, Szb55, Szb59/2) cover a narrower $^{87}\text{Sr}/^{86}\text{Sr}$ range between 0.70394 and 0.70589 with the lowest value in lherzolite Szb55 and the highest in orthopyroxene-rich websterite, Szb59/2. The melt pockets of sample Szb59/2 have nearly the same $^{87}\text{Sr}/^{86}\text{Sr}$ ratios as the coexisting clinopyroxenes.

7.3.2. Pb-isotopes

Similarly to the determined Sr isotope values the Pb ratios cover a relatively wide range (Table 21, Fig. 35, 36), but narrower than that observed by Rosenbaum et al. (1997) for separated clinopyroxenes from the same localities (Fig. 36).

$^{206}\text{Pb}/^{204}\text{Pb}$ ratios of the studied clinopyroxenes vary between 18.04 and 19.01, $^{207}\text{Pb}/^{204}\text{Pb}$ values fall between 15.45 and 15.66 and $^{208}\text{Pb}/^{204}\text{Pb}$ ratios are between 37.73 and 38.88. The lowest $^{207}\text{Pb}/^{204}\text{Pb}$ and $^{208}\text{Pb}/^{204}\text{Pb}$ ratios are shown again by the lherzolites containing websteritic veins (Table 21, Fig. 36.). In $^{206}\text{Pb}/^{204}\text{Pb}$ vs $^{208}\text{Pb}/^{204}\text{Pb}$ diagram the compositions of the vein clinopyroxenes do not differ significantly from those in the wall rocks and xenolith Szb62 has lower ratios. Whereas the wall rock clinopyroxenes of the Szb62 and Szb63 xenoliths differ from each other the vein clinopyroxenes of the two xenoliths have similar compositions to each other. A similar distribution can be observed in $^{206}\text{Pb}/^{204}\text{Pb}$ vs $^{207}\text{Pb}/^{204}\text{Pb}$ diagram. Szb01 clinopyroxenite-veined lherzolite has higher isotopic ratios compared to the previously mentioned xenoliths with higher values in the clinopyroxenite vein (Table 21, Fig. 36). The pyroxenes of both the peridotitic and orthopyroxene-rich part of composite xenolith Szb59 have very high $^{208}\text{Pb}/^{204}\text{Pb}$ and $^{207}\text{Pb}/^{204}\text{Pb}$ and medium $^{206}\text{Pb}/^{204}\text{Pb}$ ratios (Fig. 36). These values are very similar to those shown by the clinopyroxenes of the melt pocket - bearing xenoliths.

The Pb-isotopic composition of the melt pockets fall in a much more restricted range compared to the clinopyroxenes. The $^{206}\text{Pb}/^{204}\text{Pb}$ ratios of melt pockets vary between 18.69 and 19.06, $^{207}\text{Pb}/^{204}\text{Pb}$ values are between 15.65 and 15.67 and $^{208}\text{Pb}/^{204}\text{Pb}$ ratios fall between 38.80 and 38.99. The melt pockets of orthopyroxene-rich websterite Szb59/2 have the same values that were observed in the coexisting mantle clinopyroxenes (Table 21, Fig. 36). Melt pockets of lherzolite Szb55 have the highest $^{206}\text{Pb}/^{204}\text{Pb}$, $^{208}\text{Pb}/^{204}\text{Pb}$, $^{207}\text{Pb}/^{204}\text{Pb}$ ratios whereas those in the melt pockets of harzburgite Szb52 fall into the compositional range of the clinopyroxenes of melt pocket – bearing xenoliths (Table 21, Fig. 36).

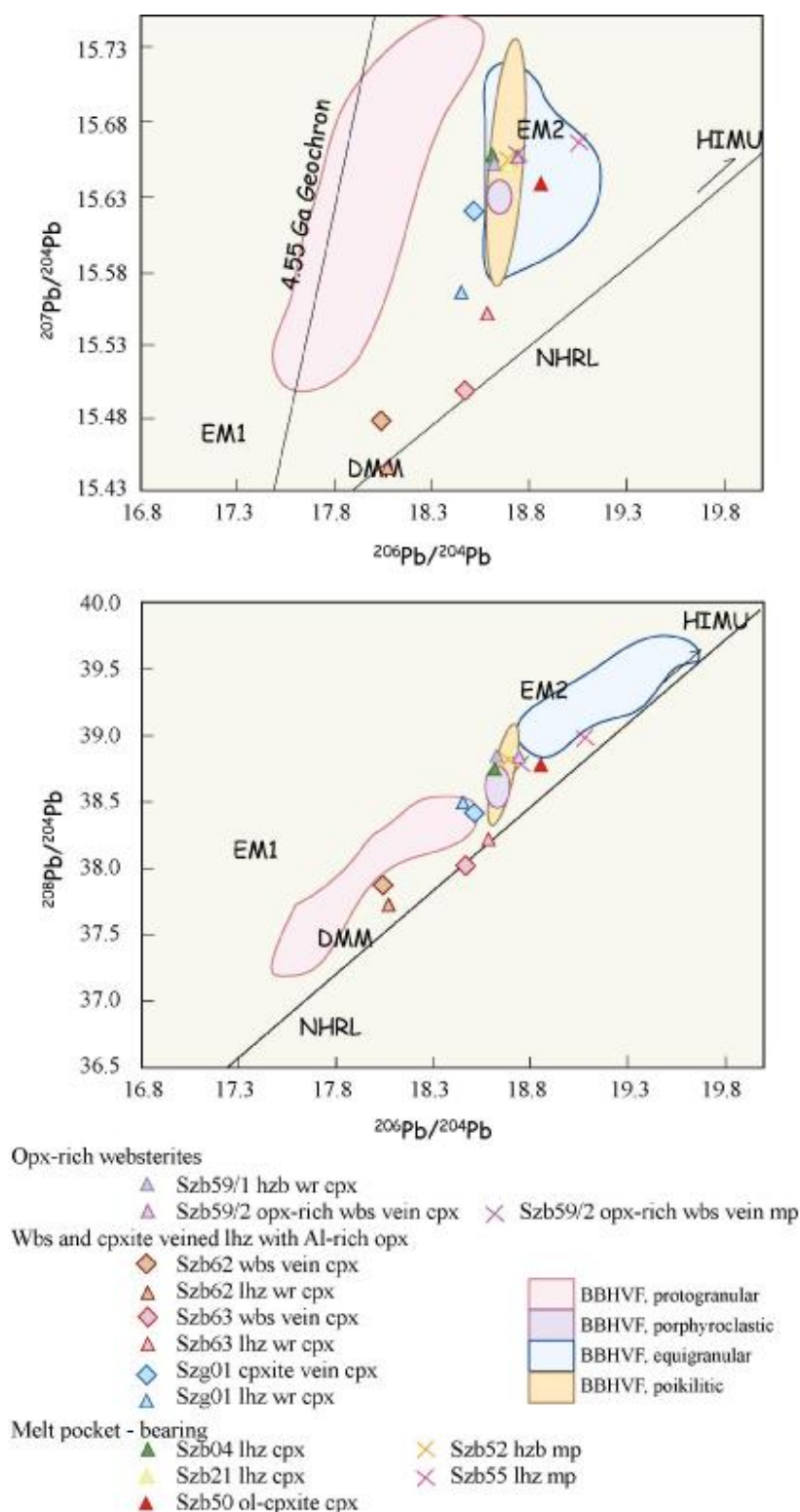


Fig. 36: Pb-isotopic compositions of separated clinopyroxenes (cpx) and silicate melt pockets (smp). For comparison the compositional field of Bakony-Balaton Highland Volcanic Field (BBHVF) (Rosenbaum et al., 1997) are also shown. Mantle components (DMM - depleted MORB mantle, HIMU - high μ , EM1 - enriched mantle 1, EM2 - enriched mantle 2) and Northern Hemisphere Reference Line (NHRL) are from Hart (1984).

8. Bulk rock chemistry

The bulk compositions of the xenoliths (Table 22) were calculated from the chemical compositions of the mineral phases (Table 3 to 8) and the modal compositions (Table 1-2). For silicate melt pocket – bearing xenoliths (Szb36, Szb59/1, Szb59/2, Szb21, Szb50, Szb55, Szb04, Szb52) the bulk composition of the rocks were determined both including the melt pockets and ignoring them to obtain the presumed original composition of the xenolith before melt pocket formation. For this calculation the compositions of melt pockets were extracted from the bulk peridotites while the amount of presumably melted primary mantle phases (mainly amphiboles and clinopyroxenes) were added into these bulk compositions (see in discussion for details).

8.1. Major elements

The bulk compositions of the studied xenoliths have a wide compositional range. The peridotites, as host rocks of melt pocket bearing xenoliths and wall rocks of those samples containing websteritic-clinopyroxenitic veins have high MgO and low Al₂O₃, CaO and Na₂O contents (Table 22) similarly to the peridotites studied by Downes et al. (1992) from the same localities. The Al₂O₃, CaO, TiO₂ and Na₂O contents decrease with increasing MgO (Fig. 37). The compositions of websterite and clinopyroxenite veins follow the trends shown by the peridotites but with much lower MgO and higher Al₂O₃, CaO, TiO₂ and Na₂O contents than the peridotites (Table 22, Fig. 37).

The orthopyroxene-rich websterites and the olivine clinopyroxenite (Szb50) have lower MgO but similar Al₂O₃ and TiO₂ contents to the peridotitic rocks (Table 22, Fig. 37), falling below the trends shown by the other samples. The CaO content of Szb50 (19.1 wt%) is much higher than in any other xenoliths, whereas that in the orthopyroxene-rich websterites is relatively low, falling above and below the trend shown by the peridotites and the websterite – clinopyroxenite veins (Fig. 37). The silicate melt pocket – bearing xenoliths have lower MgO contents than the presumed original compositions of them after extracting the melt pockets (Fig. 37).

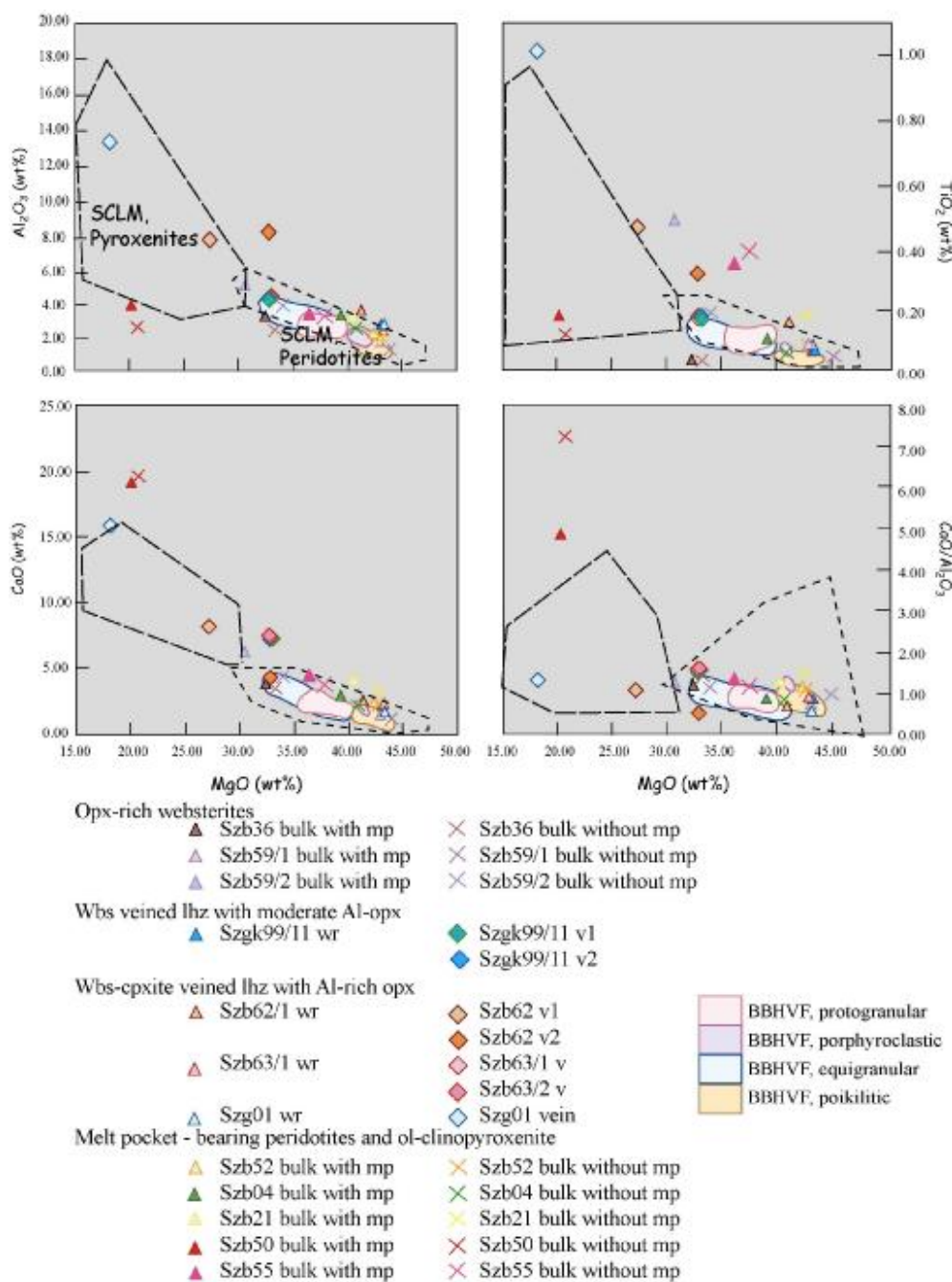


Fig. 37: Bulk rock major element variation diagrams for Bakony - Balaton Highland ultramafic xenoliths, this study. For comparison the compositional fields of ultramafic xenoliths with different textures from the BBHVF reported by Downes et al. (1992) and of peridotitic and pyroxenitic rocks in European subcontinental lithospheric mantle (SCLM) (Downes, 2001 and references therein) are also shown.

v - vein, wr - wall rock, bulk with mp - bulk composition of silicate melt pocket - bearing xenoliths, bulk without mp - presumed original bulk composition of silicate melt pocket - bearing samples with extracting the melt pockets (see in the text, in chapter 10)

8.2. Trace elements

Incompatible trace elements such as Sr, Zr and Yb show negative correlations with MgO-content (Fig. 38).

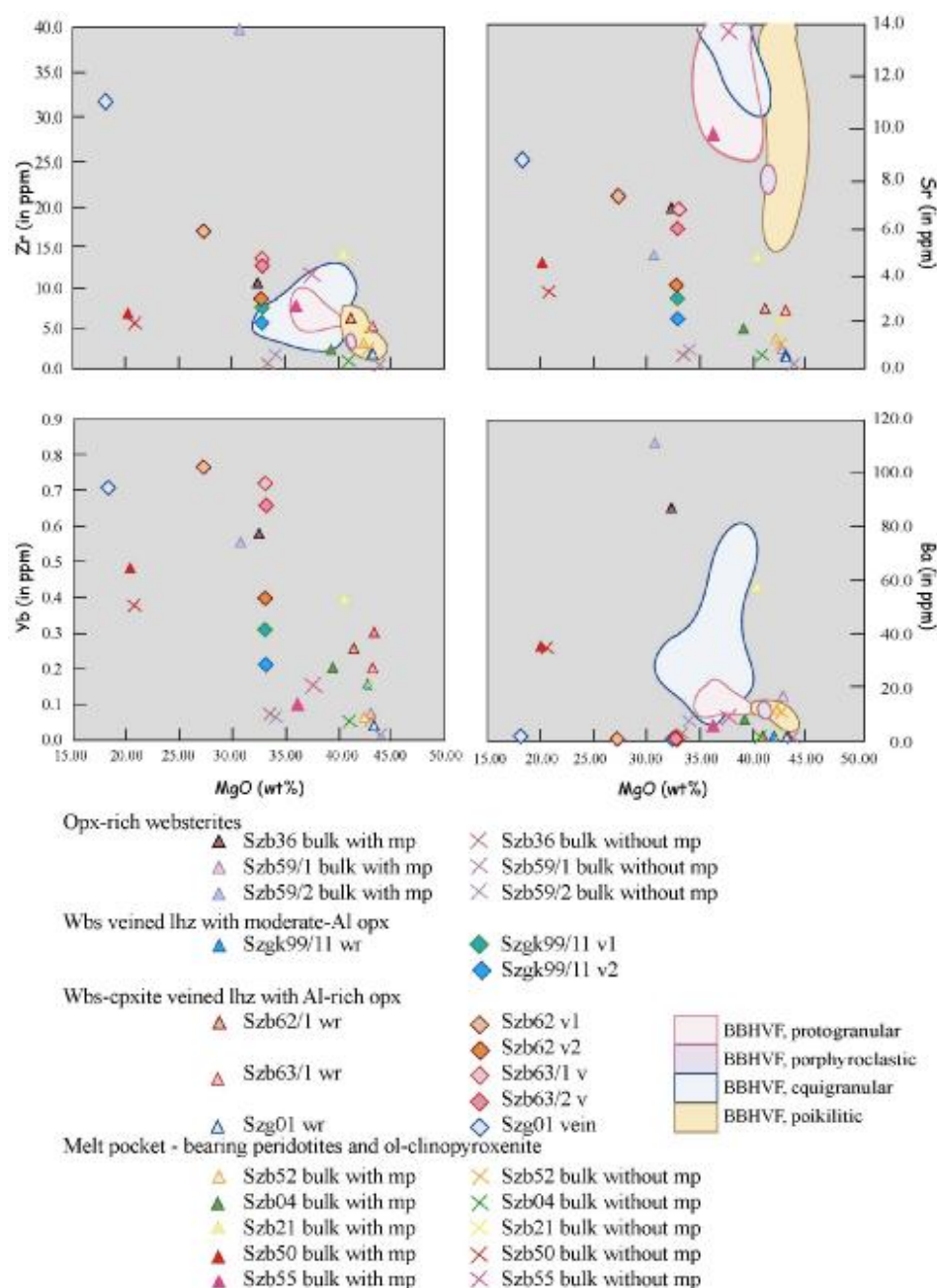


Fig. 38: Bulk rock trace element variation diagrams for Bakony - Balaton Highland ultramafic xenoliths, this study. For comparison the compositional fields of ultramafic xenoliths with different textures from the BBHVF reported by Downes et al. (1992) are also shown.

v - vein, wr - wall rock, bulk with mp - bulk composition of silicate melt pocket - bearing samples, bulk without mp - presumed original bulk composition of silicate melt pocket - bearing samples with extracting the melt pockets (see in the text, in chapter 10)

Only the olivine clinopyroxenite (Szb50) deviates from this trend, having lower incompatible element contents than other xenoliths with similar MgO contents (Fig. 38). Most of the xenoliths contain less than 20 ppm of Ba (Table 22, Fig. 38), but silicate melt pocket – bearing xenoliths Szb59/2, Szb36 and Szb21 have elevated Ba-contents of 25.0 (in Szb21) to 111.9 (in Szb59/2) ppm. The silicate melt pocket – extracted compositions of the same xenoliths however show low Ba contents similar to the other studied xenoliths and to those peridotites studied by Downes et al. (1992).

8.2.1 Orthopyroxene-rich websterites

Orthopyroxene-rich websterites Szb36 and Szb59/2 and harzburgite wall rock Szb59/1 show LREE-enrichment compared to MREEs and HREEs in chondrite normalized REE-diagram (Fig. 39). Furthermore, xenolith Szb36 shows a negative Ce-anomaly compared to the neighboring elements which is not observed neither in the orthopyroxene-rich nor in the harzburgite part of Szb59 xenolith. Furthermore this negative Ce-anomaly does not present in the melt pocket extracted compositions either.

The patterns of silicate melt pocket extracted compositions run sub-parallel to each other in primitive mantle normalized multi element diagrams with strongly depleted compositions and negative Zr- and positive Pb-anomalies. Slight negative anomaly of Ti is present only in the orthopyroxene-rich parts (Szb36 and Szb59/2). The melt pocket – bearing compositions show enrichment in incompatible elements with the highest enrichment seen in sample Szb36. Besides the negative Ce-anomaly, negative peak of Nb also appears in the melt pocket bearing – pattern of Szb36 compared to the melt pocket extracted composition of the same xenolith (Fig. 39). Furthermore, the negative Ti-anomaly observed either in the melt pocket - extracted compositions becomes deeper in this sample. In xenolith Szb59 the melt pocket – bearing compositions have smoother trace element pattern than that of the Szb36 with strong positive Pb-anomaly.

8.2.2. Spinel lherzolites with websterite or clinopyroxenite vein(s)

As the bulk rock compositions were calculated based on mineral compositions the REE and multi element patterns reflect the clinopyroxene compositions so that I set aside the

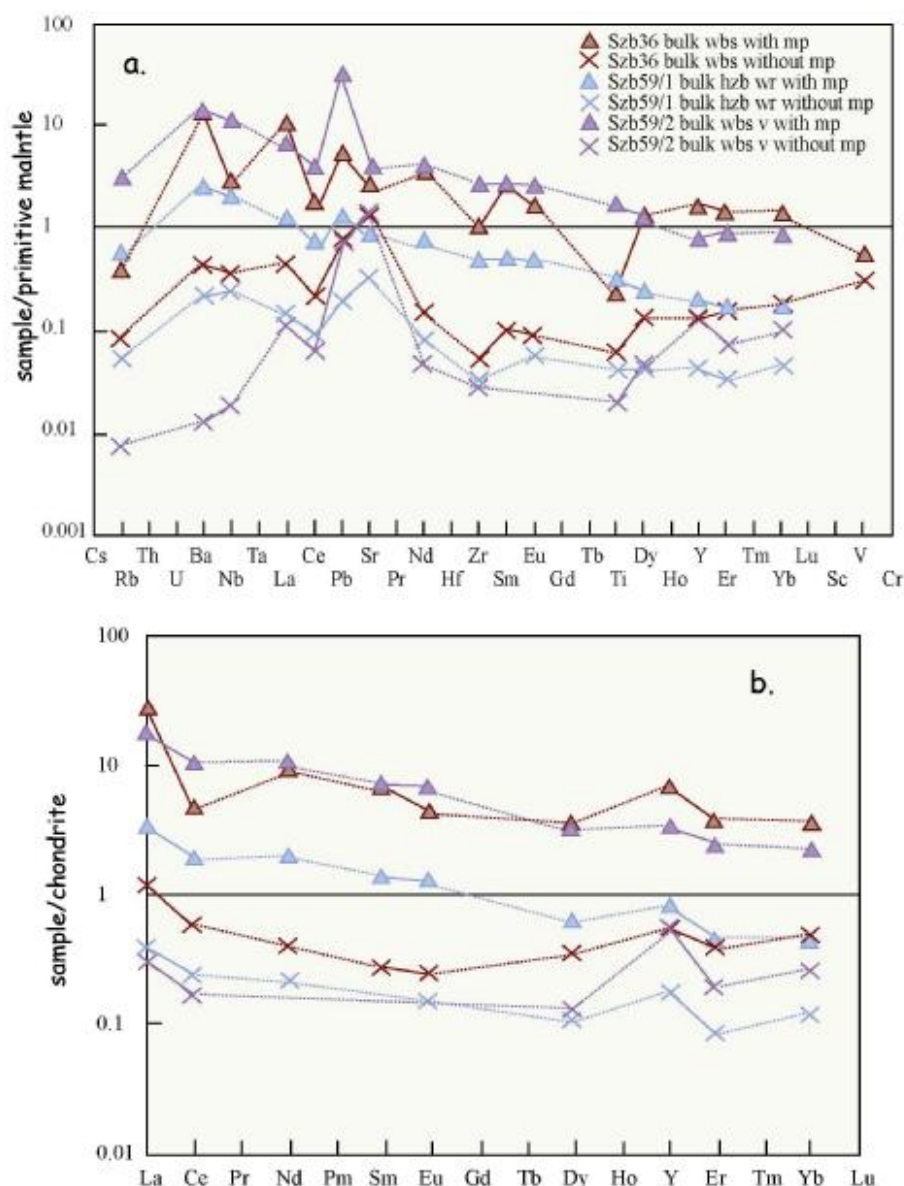


Fig. 39: Bulk rock trace element variation diagrams for orthopyroxene-rich websterite and harzburgitic wall rock xenoliths. Normalizing values are from Sun & McDonough (1995) - primitive mantle; and Anders & Grevesse (1989) - chondrite.

bulk with mp - bulk composition of silicate melt pocket - bearing xenoliths, bulk without mp - presumed original bulk composition of silicate melt pocket - bearing xenoliths with extracting the melt pockets (see in the text, in chapter 10)

detailed description of the patterns. All xenoliths with websterite and clinopyroxenite veins have n-shaped REE patterns with different extents of LREE-depletion (Fig. 40). All xenoliths, both the wall rock and veins, are slightly enriched in MREEs compared to LREEs and HREEs (Fig. 40). The primitive mantle normalized multi element diagrams show

incompatible element depletion and negative Zr-anomalies. Negative Ti-anomaly is characteristic for all xenoliths except Szg01 clinopyroxenite veined lherzolite (Fig. 40).

The wall rock of Szb62 and Szb63 xenoliths have overall higher trace element content compared to the relatively depleted wall rocks of Szgk99/11 and Szg01 xenoliths. The strongest trace element enrichment is observed in the clinopyroxenite vein of Szg01.

8.2.3. Spinel peridotites and pyroxenites with silicate melt pockets and veins

The chondrite normalized REE-patterns of silicate melt pocket bearing samples usually show LREE and MREE enrichments compared to the HREE (Fig. 42). The only exception is the olivine clinopyroxenite sample (Szb50) which is slightly depleted in LREEs compared to the MREEs, but its overall REE content is relatively high ($REE_N > 1$) (Table 22, Fig. 41). An unequivocal negative Ce-anomaly is only observed in sample Szb36. The pattern of silicate melt pocket extracted compositions usually run well below the pattern of the melt pocket bearing ones. Only xenoliths Szb50, Szb52 and Szb55 show overall similar patterns. Furthermore, no negative Ce-anomaly is observed in the melt pocket extracted bulk composition of orthopyroxene-rich websterite.

All xenoliths are enriched in incompatible trace elements and show different degrees of depletion in Nb ($Ba_N/Nb_N > 1$) and positive anomaly of Pb (with the exception of lherzolite Szb55) (Fig. 42). Most of the samples also have negative anomalies of Zr and Ti with the exception of sample Szb59/1, which does not have negative anomaly of Zr and has slight positive peak of Ti (Fig. 42). No unambiguous difference is observed between the samples with or without carbonate. The strong negative anomaly of Nb and positive anomaly of Pb are absent or much smoother in the patterns of melt pocket extracted bulk compositions (Fig. 41).

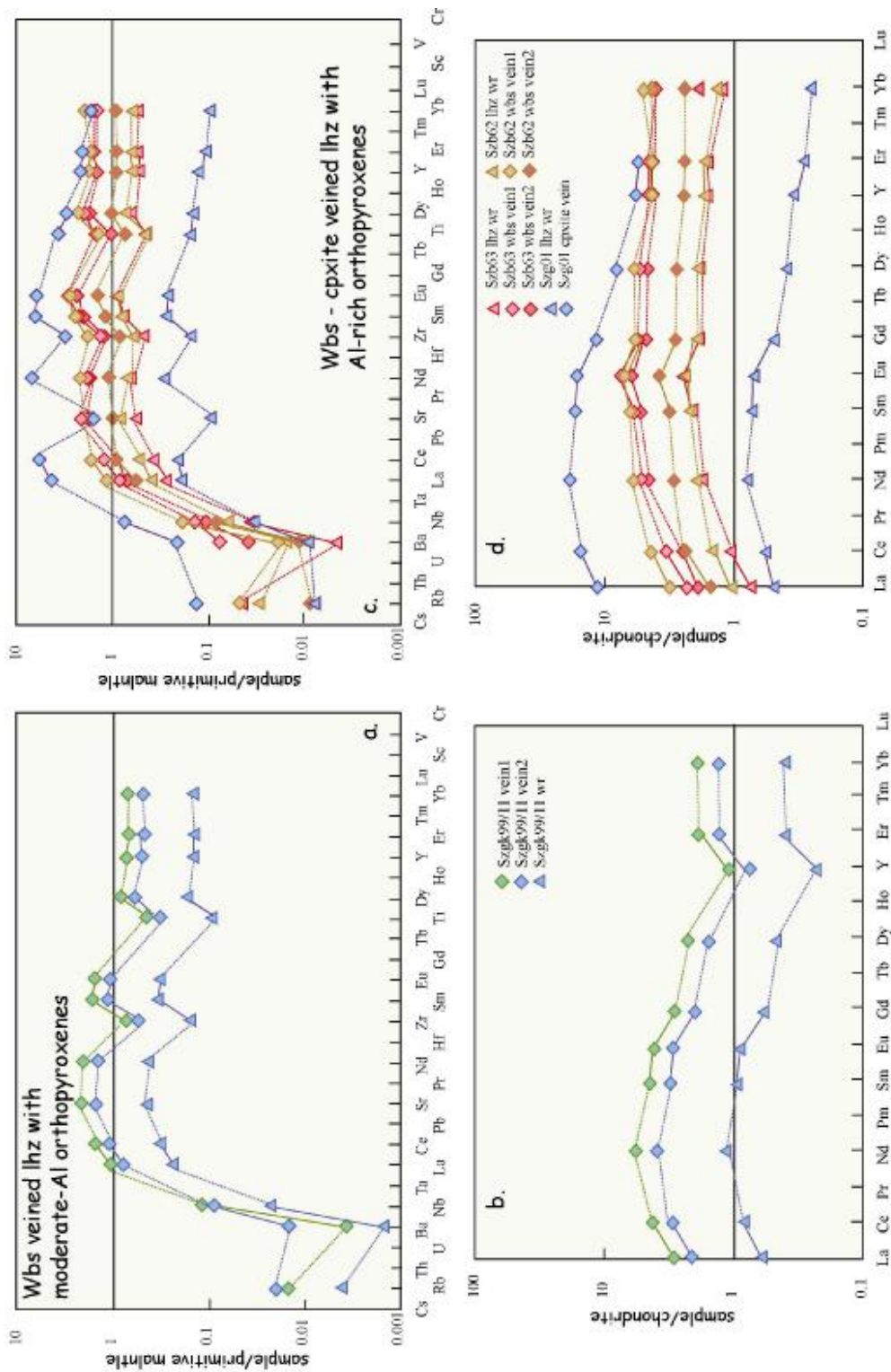


Fig. 40: Bulk rock trace element variation diagrams for websterite and clinopyroxene veined spinel lherzolites. Normalizing values are from Sun & McDonough (1995) - primitive mantle; and Anders & Grevesse (1989) - chondrite. wr - wall rock

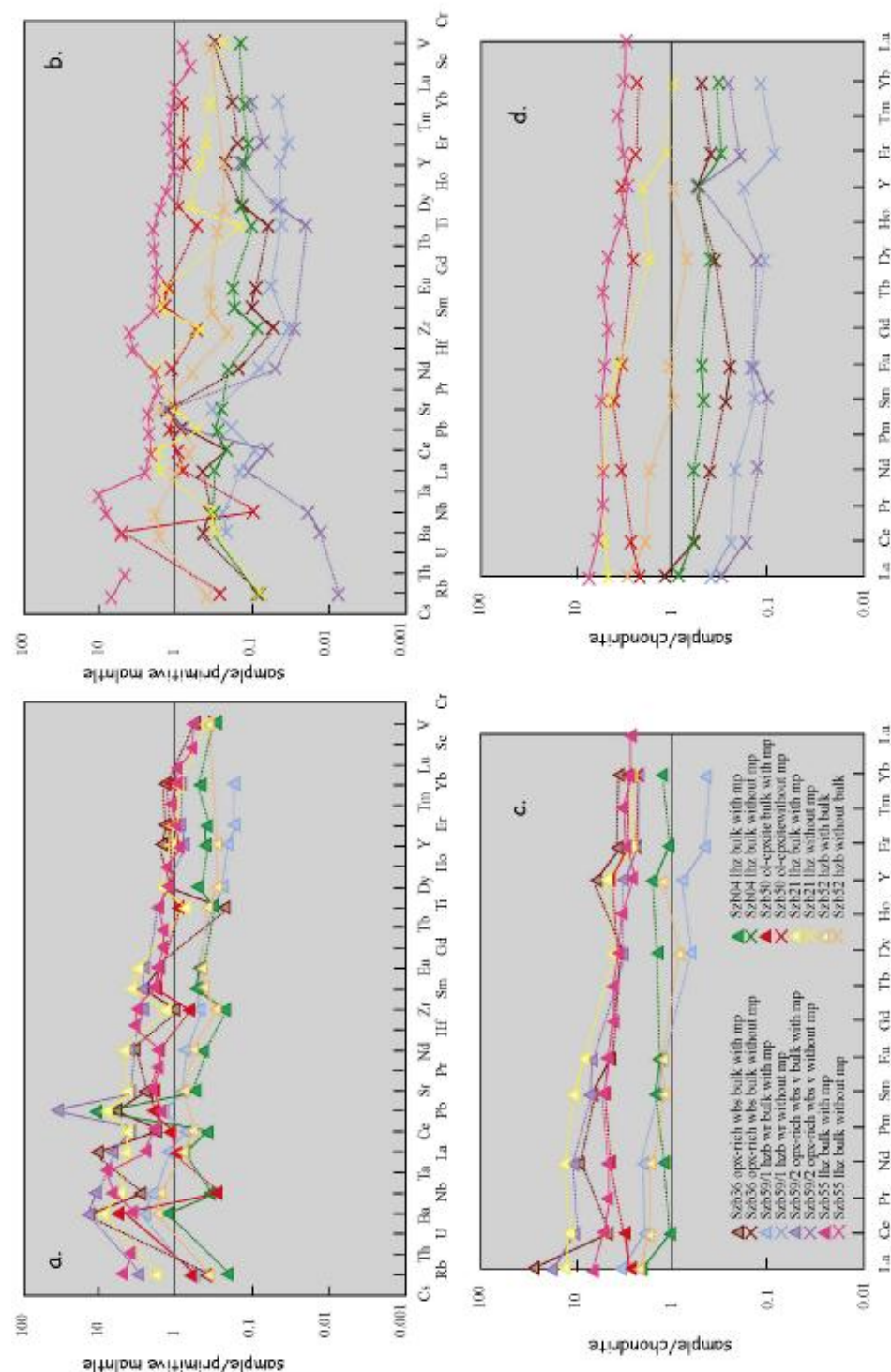


Fig. 41: Bulk rock trace element variation diagrams for silicate melt pocket - bearing xenoliths. Normalizing values are from Sun & McDonough (1995) - primitive mantle, and Anders & Grevesse (1989) - chondrite.

bulk with mp - bulk composition of silicate melt pocket - bearing samples, bulk without mp - presumed original bulk composition of silicate melt pocket - bearing samples with extracting the melt pockets (see in the text, in chapter 10)

Talbe 22 bulk rock

9. Equilibrium conditions

9.1. Interaction between websterite - clinopyroxenite veins and peridotite wall rocks

For all the pyroxene enriched rock types i.e. websterite, clinopyroxenite veins and orthopyroxene-rich websterites, it appears that the veins and their wall rock peridotites are in equilibrium. This is based on the compositions of both vein and wall rock minerals. No unequivocal differences are observed in the major element compositions between the different rock types i.e. veins and wall rock of the same sample (see microprobe data in Tables 3 to 6), and there are no differences even in the trace element contents of the clinopyroxenes. In all cases a narrow compositional range can be observed in the spider and REE diagrams (Fig. 27 to 30) and the compositional ranges of vein and wall rock clinopyroxenes are exactly the same. Furthermore there are no significant isotopic differences between them. This suggests that after the formation of the veins the material of the veins and the wall rock reached equilibrium at least on the several cm scale (Fig. 9b) provided by the size of the xenoliths.

9.2. Equilibrium between melt pocket amphiboles and their wall rock peridotites

Equilibrium between disseminated and interstitial amphiboles and their wall rock peridotites can be studied based on textural relationships and chemical compositions. For textural equilibrium there will be sharp boundaries between the amphiboles and the mineral assemblage of the peridotite whereas in the case of disequilibrium, amphibole overgrowths will be observed on the coexisting mantle minerals. Both the studied xenoliths contain only resorbing amphiboles in melt pockets. In these xenoliths trace element distribution coefficients between mantle clinopyroxenes and mantle amphiboles can provide useful information. As mantle clinopyroxenes were analyzed only in harzburgite Szb52, conclusions can be drawn only for the assemblage of this xenolith. The calculated distribution coefficients are shown in Fig. 42.

Compared with the experimental distribution coefficients for equilibrated amphiboles and clinopyroxenes (Tiepolo et al. 2000) the values calculated are usually similar (except for Ba), but the Amph/Cpx trace element ratios cannot be considered fixed to specific values, but depend on the crystal-chemical features of the two minerals. Compared with Amph/Cpx distribution coefficients from other localities of the CPR (Szabó et al., 1995a) and worldwide (Vannucci et al., 1995) the homogeneous amphiboles and clinopyroxenes of harzburgite Szb52 represent (at least!) a stage of the equilibration process.

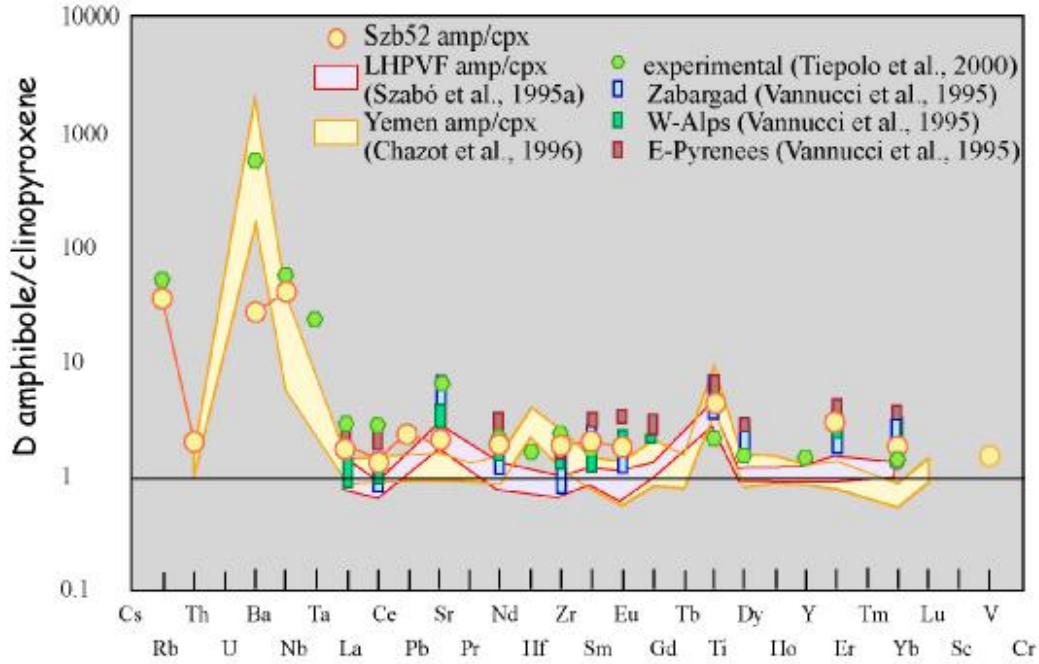


Fig. 42: Calculated trace element distribution coefficients between mantle amphiboles and clinopyroxenes in harzburgite Szabó 52. For comparison the experimental data on equilibrated clinopyroxene - amphibole pairs from Tiepolo et al. (2000) and distribution coefficients determined in ultramafic xenoliths and peridotite massifs, where equilibrium was suggested between the phases, are also plotted.

9.3. Estimates of equilibrium temperature and oxygen fugacity

To outline the equilibrium conditions of ultramafic xenoliths the equilibrium temperature and oxygen fugacity (+/- pressure) of the xenoliths were calculated based on the compositions of primary mantle minerals (olivine-I, orthopyroxene-I, clinopyroxene-I and spinel-I) assuming that they are in equilibrium. For the temperature estimation, the ‘two pyroxene’ and ‘Ca in orthopyroxene’ methods of Brey & Köhler (1990) were used:

$$T_{\text{BKN}} = \frac{23664 + (24 \cdot 9 + 126 \cdot 3 X_{\text{Fe}}^{\text{cpx}}) P}{13 \cdot 38 + (\ln K_D^*)^2 + 11 \cdot 59 X_{\text{Fe}}^{\text{opx}}}$$

and

$$T_{\text{Ca-in-opx}} = \frac{6425 + 26.4P}{-\ln \text{Ca}_{\text{opx}} + 1.843}$$

where $K_D^* = (1 - \text{Ca}^*)^{\text{cpx}} / (1 - \text{Ca}^*)^{\text{opx}}$; $\text{Ca}^* = \text{Ca}^{\text{M2}} / (1 - \text{Na}^{\text{M2}})$ and $X_{\text{Fe}}^{\text{px}} = \text{Fe} / (\text{Fe} + \text{Mg})$; T is in Kelvin, P is in kilobars for which 15 kilobars was used. As this geothermometer is based on the

composition of coexisting orthopyroxenes and clinopyroxenes it could not be used for the clinopyroxenite vein of xenolith Szg01. For this clinopyroxenite, the method of Mercier (1980) was used.

The equilibrium oxygen fugacity was determined by the method of Ballhaus et al. (1991) based on the composition of coexisting olivine and spinel:

$$\Delta \log(f_{O_2})^{FMQ} = 0.27 + 2505/T - 400P/T - 6\log(X_{Fe}^{olv}) - 3200(1 - X_{Fe}^{olv})^2/T + 2\log(X_{Fe^{2+}}^{sp}) + 4\log(X_{Fe^{3+}}^{sp}) + 2630(X_{Al}^{sp})^2/T$$

where

$$X_{Fe}^{olv} = Fe^{2+}/(Fe^{2+} + Mg) \text{ where olv is olivine}$$

$$X_{Fe^{2+}}^{sp} = Fe^{2+}/(Fe^{2+} + Mg)$$

$$X_{Fe^{3+}}^{sp} = Fe^{3+}/(Fe^{3+} + Cr + Al)$$

$$X_{Al}^{sp} = Al/(Fe^{3+} + Cr + Al)$$

For equilibrium pressure estimation there is no accepted geobarometer for spinel peridotites but the results of the calculation carried out by the barometer of Mercier (1980) (based on the pyroxene compositions equilibrium with spinel [diopside-spinel and enstatite-spinel]) are shown for information.

The calculations were carried out by the MINPROG software established by Harangi (1990-93). The results are seen in Table 1 and Fig. 43. In Fig. 43 the correlation between equilibrium temperatures and oxygen fugacities is shown.

The calculated equilibrium temperatures cover a very wide range from 815 (in melt pocket-bearing sample Szb50) to 1150 °C (in the lherzolite wall rock of xenolith Szb62) (Table 1). The calculated equilibrium oxygen fugacity values also show a wide variation from -1.316 (in websterite vein1 of lherzolite Szb62) to +0.710 (in harzburgite wall rock Szb59/1) logarithmic units compared to the quartz-fayalite-magnetite (QFM) buffer (Table 1, Fig. 43). In the oxygen fugacity vs equilibrium temperature diagram the samples fall usually above the magnetite-wustite buffer (after Chen et al., 1991). With the exception of the silicate melt pocket bearing xenoliths the petrographically distinct groups show different equilibrium states (Fig. 43) which is predominantly governed by their different oxidation states.

The highest temperatures and lowest oxygen fugacity values are observed in the websterite veined lherzolites which contained Al-rich orthopyroxenes falling near to the magnetite-wustite buffer and a little below the field of the Bakony - Balaton Highland ultramafic xenoliths calculated by Szabó et al. (1995b).

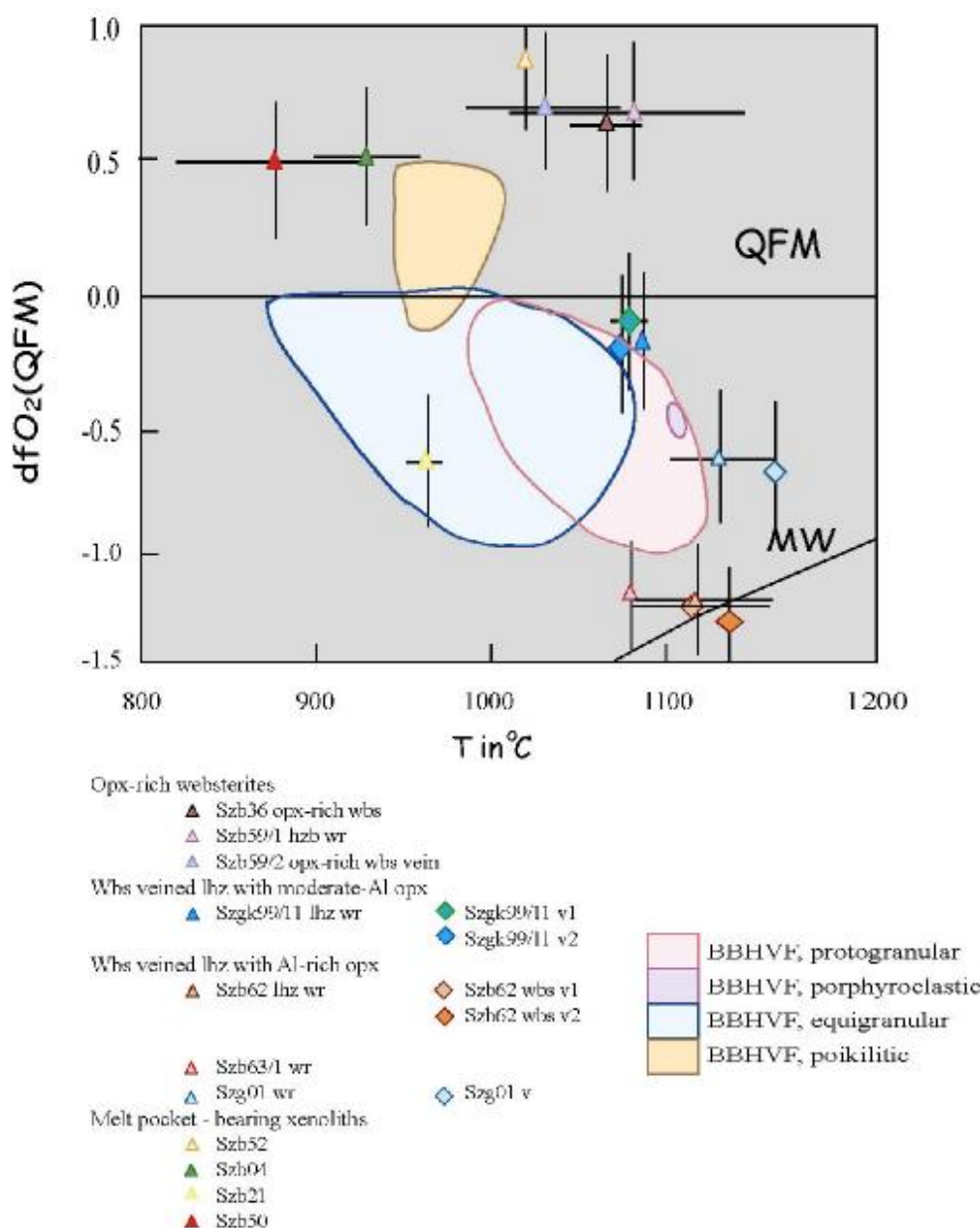


Fig. 43: Calculated equilibrium temperature vs. equilibrium oxygen fugacity diagram for Bakony - Balaton Highland Volcanic Field ultramafic xenoliths, this study. Symbols indicate the average of the temperature range shown in Table 1, error bars indicate the temperature and oxygen fugacity range. For comparison the field of equilibrium conditions from ultramafic xenoliths with different textures from the BBHVF reported by Downes et al. (1992) calculated by Szabó et al. (1995b) are also shown. QFM is indicated based on Ballhaus et al. (1991), MW is after Chen et al. (1991).

wr - wall rock, v - vein

There is no difference between the equilibrium state of websterite veins and the wall rock peridotites. Websterite veined xenolith Szgk99/11 containing orthopyroxenes with moderate Al content are characterized by similar equilibrium temperatures, but at much higher oxygen fugacity values than those observed in the previous group (Fig. 43). These values for Szgk99/11 xenolith are similar to those calculated in predominantly protogranular textured ultramafic xenoliths by Szabó et al. (1995b) from the same localities. Clinopyroxenite veined lherzolite Szg01 can be characterized also by high equilibrium temperatures as was observed in the websterite veined lherzolites, but the equilibrium oxygen fugacities for both the vein and the wall rock fall between the range of the previously described distinct groups (Fig. 43).

Orthopyroxene-rich websterites (Szb36 and Szb59/2 and the harzburgite wall rock Szb59/1) have high equilibrium temperatures either and higher equilibrium oxygen fugacities compared to the previously mentioned groups (Fig. 43). The oxygen fugacity values are above the QFM buffer and even higher than any other Bakony – Balaton Highland ultramafic xenoliths (Szabó et al., 1995b).

The melt pocket - bearing xenoliths usually have equilibrium oxygen fugacity values above QFM (except sample Szb21) and much lower equilibrium temperatures than in the groups discussed above (Fig. 44), having similar equilibrium temperatures to the equigranular samples studied by Szabó et al. (1995b).

Clear relations between equilibrium temperatures, oxygen fugacities and the isotopic composition of the studied xenoliths are also observed. The websterite and clinopyroxenite veined xenoliths with Al-rich orthopyroxenes have the highest equilibrium temperatures and the most reducing state trending from depleted mantle towards HIMU mantle component in T vs $^{207}\text{Pb}/^{206}\text{Pb}$ and $^{208}\text{Pb}/^{206}\text{Pb}$ diagrams with increasing $f\text{O}_2$ values. Whereas the other xenoliths (orthopyroxene – rich websterites, clinopyroxenite veined lherzolite and the melt pocket – bearing xenoliths) that trend towards enriched mantle (EM2) have lower temperatures and more oxidizing formation conditions (Fig. 44).

The correlation between the equilibrium oxidation state, temperature in the different rock types could be controlled either by the nature of metasomatism or by the nature of the mantle domain into which the metasomatizing melts/fluids intruded forming the different rock types.

The environment during the formation of websterite veins with Al-rich orthopyroxenes is characterized by high temperature and extremely low oxygen fugacity. As this environment is more reducing than that was observed for lithospheric mantle at the same localities Szabó et al. (1995b), it most probably represents the oxygen fugacity state of the metasomatizing agent which penetrated the peridotitic wall rock and formed the websteritic veins.

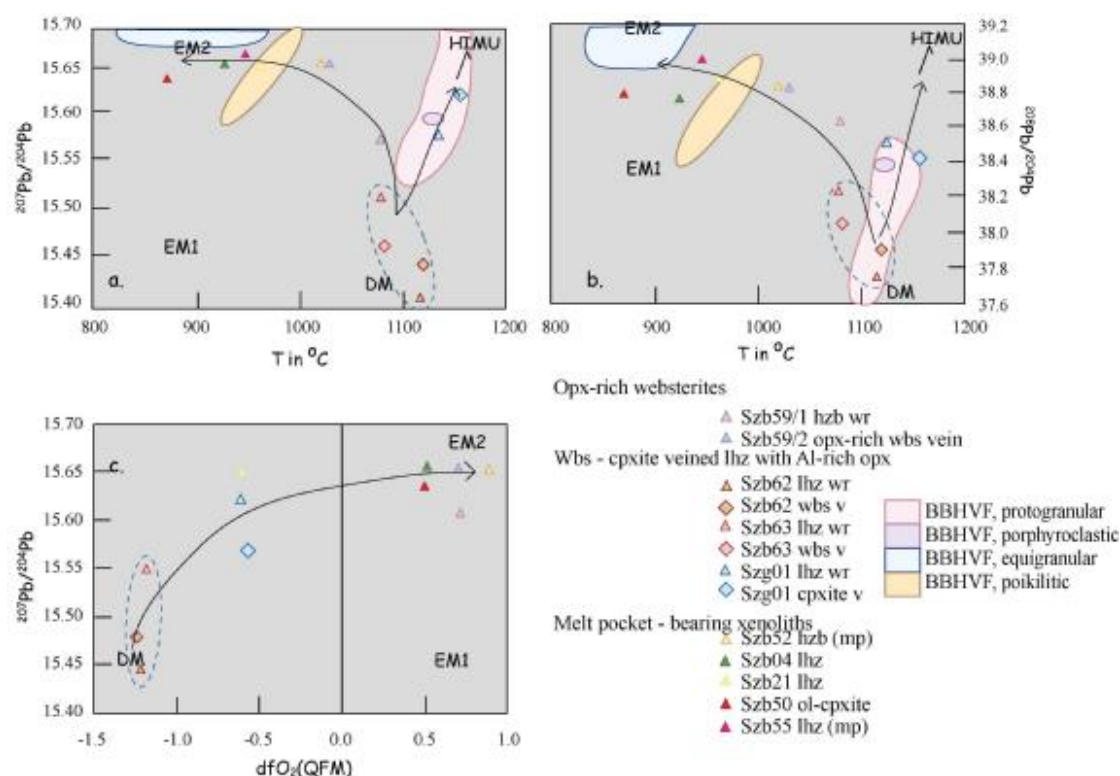


Fig. 44: Calculated equilibrium temperature (a, b) and equilibrium oxygen fugacity (c) vs. Pb-isotopic ratios diagram for Bakony - Balaton Highland Volcanic Field ultramafic xenoliths, this study. QFM is indicated based on Ballhaus et al. (1991). The composition fields of clinopyroxenes from ultramafic xenoliths with different textures from the BBHVF reported by Downes et al. (1992) and Rosebaum et al. (1997) are also shown for comparison. DM - depleted mantle, EM1 - enriched mantle 1, EM2 - enriched mantle 2 after Hart (1984). Note, that in harzburgite Sz652 and lherzolite Sz655 the isotopic composition of silicate melt pockets was analyzed whereas the equilibrium conditions were calculated based on the mantle assemblage.

wr - wall rock, v - vein, mp - silicate melt pocket

In case of websteritic veins with moderate Al-orthopyroxenes the material of both the veins and the wall rock got into equilibrium with the surrounding mantle material showing the equilibrium range typical for the BBHVF mantle (Fig. 43). For the orthopyroxene-rich websterites higher oxygen fugacities were usually observed compared to the BBHVF peridotitic mantle (Fig. 43) suggesting the involvement of oxidatising melt(s)/fluid(s) reacting with the relatively reductive mantle. The silicate melt pocket bearing peridotites cover a very wide range in Fig. 43 suggesting that only the melt pocket formation by which they were ranked into the same petrographic group did not unify the chemical character of them and/or the melt pockets have different origin in the different xenoliths.